Analysis of flamelet-based methods to reduce chemical kinetics in flame computations

Please check the document version of this publication:

• A submitted manuscript is the version of the article upon submission and before peer-review. There can be important differences between the submitted version and the official published version of record. People interested in the research are advised to contact the author for the final version of the publication, or visit the DOI to the publisher's website.
• The final author version and the galley proof are versions of the publication after peer review.
• The final published version features the final layout of the paper including the volume, issue and page numbers.

[Link to publication](#)

Analysis of Flamelet-Based Methods to Reduce Chemical Kinetics in Flame Computations

PROEFSCHRIFT

ter verkrijging van de graad van doctor aan de
Technische Universiteit Eindhoven, op gezag van de
Rector Magnificus, prof.dr.ir. C.J. van Duijn, voor een
commissie aangewezen door het College voor
Promoties in het openbaar te verdedigen
op dinsdag 13 september 2005 om 16.00 uur

door

Happy Bongers

geboren te Assen

Dit proefschrift is goedgekeurd door de promotoren:

prof.dr. L.P.H. de Goey
en
prof.dr.ir. A.A. van Steenhoven

Contents

General introduction

The world's energy demand has increased enormously in the past decades. Combustion processes play a major role in the conversion of energy, which is needed for transport, the generation of electrical energy, and heating devices. Recently, computer simulations of complex burner systems have become an important tool in the design process of modern combustion applications. Therefore, much effort is put in the development of models, which are both accurate and efficient. The subject of this thesis is the development and application of methods that are used to make combustion models more efficient, which means that the computational effort to solve these models is reduced without losing too much accuracy with respect to the original models. Special attention is paid to the coupling between chemical and transport processes, such as diffusion and convection, which plays an important role in an accurate description of combustion processes.

This chapter starts with a description of the research objectives and motivation. In the subsequent section, a general introduction to combustion is given. In the final section, an overview of the thesis is presented.

1.1   Research motivation and background

In this section, a motivation for the research is given. Firstly, the importance of combustion in our daily lives is placed in a historical perspective. Secondly, a number of problems, encountered in current combustion modelling is briefly discussed. Finally, the research objectives are presented.

1.1.1   Historical background

Since the early years of human civilisation, people were fascinated by fire. From the moment people were able to control fire, it has played an increasingly important role in our lives. Initially, fire was used directly, for instance for domestic heating, cooking, the creation of new arable land or as a weapon of destruction in wars. Over the years, as tools became more sophisticated, fire was used more and more indirectly. The generated heat is converted into kinetic energy, for instance in internal combustion engines, gas turbines or for the propulsion of rockets. Nowadays, our daily life strongly depends on combustion of fossil fuels. With the increasing energy demand,

also the need for fuels increased. However, the negative side effects of combustion, such as the emission of pollutant exhaust gases, soot, and unburnt hydrocarbons, have become more and more evident. Pollutant gases are for instance nitric oxides (NO_x), sulfur oxides (SO_x), and carbon dioxide (CO_2). Furthermore, the resources of fossil fuels are running out, even though it is expected that they will last for the next 50-100 years [41].

Since a few decades, the search for alternative sources of energy that are not based on combustion, like e.g. solar and wind energy has emerged. However, it is expected that combustion will play a key role in the energy conversion in the next decades, for instance with the advent of biomass and hydrogen combustion. To increase the efficiency of current and future combustion systems, severe legislations are introduced to restrict the amount of pollutant exhaust gases. These legislations put high demands on the design of new combustion systems. Advanced combustion models play a key role in the design processes of new combustion systems. Detailed information is needed to predict e.g. pollutant exhaust gases, flame stability, and temperature profiles. However, the currently available advanced models are too complex to be used in the simulation of practical burner systems. To enable the modelling of complex burner systems, much effort is put in the development of simplified models, while maintaining the accuracy.

1.1.2 Problem definition

Combustion has been an important research topic for hundreds of years. Initially, the studies were focused on the understanding of the basic principles of fire. Most of the studies were experimental or analytical. The analytical studies were restricted to strongly simplified models. With the introduction of modern computers, more sophisticated models were introduced, which incorporate detailed descriptions of chemical kinetics and molecular transport. However, due to the complexity of these systems, detailed studies of practical combustion systems are still prohibited. For example, a detailed reaction mechanism may contain hundreds of species and even more reactions. For each species a differential equation must be solved. In addition, these equations are strongly coupled and highly non-linear, which make them hard to solve [58].

To be able to do simulations of more complex burner systems, several strategies can be followed. Besides using sophisticated and effective numerical methods, specific modelling strategies are introduced. Two important categories are the so-called chemical reduction techniques and flamelet techniques. The main purpose of these techniques is to simplify the three-dimensional detailed combustion models, without significantly harming the accuracy. Both techniques are based on the observation that the general behaviour of a flame is characterised by a wide range of time and length scales. In chemical reduction techniques, it is assumed that a large number of fast chemical processes can be considered in steady-state. The identity

and the number of processes, which are taken in steady-state, depend on the reduction method chosen. In flamelet methods, a flame is considered as a thin front, which can be considered as quasi one-dimensional. The internal structure of the flame front can be described by a set of one-dimensional equations, i.e. the flamelet equations [39,76].

A number of reduction methods has been introduced in the past, e.g. [54,55,58, 75]. In chapter 3, an overview of the basic principles of reduction methods is given, in which these methods are explained briefly. The Intrinsic Low-Dimensional Manifold reduction method [58] is treated in more detail, as its theory is used in the remainder of the thesis. In general, a chemical reduction method is used to decrease the size of the original reaction mechanism in a pre-processing step. The reduction methods have been used successfully in numerous applications. However, during the construction of the reduced mechanism, only the chemical processes are taken into account. Nonetheless, the complete combustion process is a combination of chemical, convective and diffusive processes. The evaluation of the fast time scales from chemistry alone and the disregard of transport in the construction of the reduced mechanism may lead to inaccuracies in the model. These inaccuracies generally occur in colder parts of the flame, where chemical and transport scales are of the same order.

A solution to this problem was introduced by Van Oijen and De Goey [69], who introduced the Flamelet-Generated Manifold (FGM) method. The FGM method shares the idea with flamelet methods, that a flame can be seen as an ensemble of one-dimensional flames. The reduced mechanism obtained with FGM is based on the solution of premixed laminar flames, so both transport and chemical processes are taken into account. The FGM method has been used with success in a number of simulations [37,69–72]. However, the mathematical foundations of the FGM method are less strong than in some of the reduction methods, like for instance the Intrinsic-Low Dimensional Manifold (ILDM) method. Furthermore, as the FGM method is based on the solution of premixed flames, its applicability to flames, which are non-premixed and partially-premixed, is questionable.

Summarising, the general issue of this thesis is twofold. Firstly, even in reduced models, an accurate description of the coupling between chemical and transport processes is necessary for an accurate prediction of the flame behaviour. Secondly, even though the FGM reduction method, which incorporates this coupling, has proven to be very accurate, its mathematical background is less strong than in some other reduction methods, like for instance the ILDM method.

1.1.3   Research objectives

The main purpose of this research is the further testing of existing reduction techniques and the development of new reduction techniques, with respect to the problems mentioned in the previous section. The study of the reduction methods fo-

cuses on two methods, which have been introduced in the past, i.e. the Intrinsic Low-Dimensional Manifold (ILDM) method [58] and the Flamelet-Generated Manifold (FGM) method [69]. The general theme in this study is the coupling between chemical and transport processes and its effect on the flame behaviour. Firstly, to investigate the importance of an accurate description of molecular transport, several transport models are tested in a one-dimensional premixed flame configuration. Secondly, the major advantages and disadvantages of the FGM and ILDM method are studied. For example, the applicability of the FGM method, which was originally designed for premixed combustion, is tested in an environment that is not purely premixed. Finally, the possibility of the creation of a new reduction method, which combines the benefits of both the studied methods is investigated. This reduction method is referred to as Phase Space ILDM (PS-ILDM). This new method should be a reduction method, which takes transport processes into account and has a strong mathematical foundation.

1.2   Combustion: general principles

At first, it must be pointed out that several flame types can be distinguished. Generally, combustion can be described as an exothermic reaction between a fuel and an oxidiser, but each different flame type is characterised by different processes. For instance, in combustion of solid fuels (e.g. wood and coal) and liquid fuels (e.g. kerosine and gasoline), melting and vaporisation processes are important for the flame behaviour. These processes are absent in gaseous combustion. It should be noticed that most of the combustion chemistry normally takes place in the gaseous phase. The identity of gaseous flames strongly depends on the extent of premixing of fuel and oxidiser. Two limiting cases can be identified: a purely premixed flame and a purely non-premixed flame.

In general, a flame front can be seen as a thin layer in which the chemical conversion of fuel into products takes place. Figure 1.1 shows an example of a thin flame front surrounded by non-reacting gases. In case of a premixed flame, the gases on one side of the flame front are the fuel and the oxidiser. In the flame front, the fuel and oxidiser react and the burnt gases are found on the other side of the flame front. In case of a non-premixed flame, the flame front separates the fuel from the products. In the figures 1.2 and 1.3, the internal structure of the flame front is presented schematically for a premixed flame and a non-premixed flame, respectively.

A typical premixed flame structure is shown in figure 1.2a. A premixed flame is defined as a region in space, where a typical flame variable $\mathcal{Y}$ varies between its unburnt value $\mathcal{Y}_u$ and its burnt value $\mathcal{Y}_b$. This flame variable can be, for instance, the temperature, the density, or a species mass fraction. In the flame front, flame surfaces are defined as iso-contours of the variable $\mathcal{Y}$. Figure 1.2b shows profiles of a number of flame variables as a function of the coordinate perpendicular
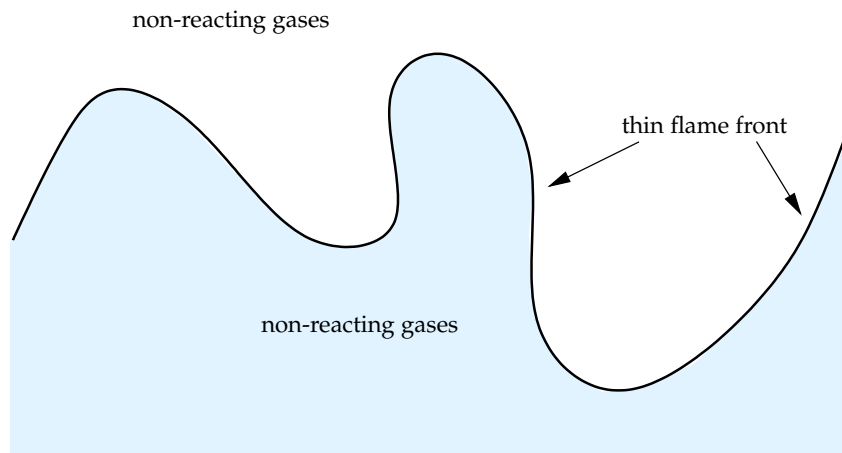
Figure 1.1 : A schematic example of a thin reacting flame front surrounded by non-reacting gases.

to the iso-contours of $\mathcal{Y}$. Characteristic for a premixed flame is that the flame is self-propagating. The propagation velocity is strongly determined by the laminar burning velocity s_L. Based on the ratio between s_L and the speed of sound c, premixed flames can be separated into detonations ($s_\mathrm{L} \geq c$) and deflagarations ($s_\mathrm{L} < c$). As most flames in practical applications are deflagarations, the flames studied in this thesis are restricted to deflagarations.

A non-premixed flame is defined as a region in space, where a typical flame variable varies between its value in the fuel stream and its value in the oxidiser stream. Figure 1.3a shows a typical non-premixed flame structure. For non-premixed flames, the mixture fraction Z, which is a measure for the mixing of fuel and oxidiser, is often used as flame variable. Products are transported along the iso-contours of Z. The internal structure of a non-premixed flame is shown in figure 1.3b. The figure shows typical flame variables as a function of the coordinate s, which is in this case the coordinate locally perpendicular to the iso-contours of Z.

In practice, many combustion systems are neither purely non-premixed, nor purely premixed. Therefore, the so-called partially-premixed flames are a special field of interest. Figure 1.4 shows a schematic example of three different counter-flow flame configurations. A counterflow flame is formed by two opposed jets, which impinge and form a stagnation plane. If both jets are equal mixtures of fuel and oxidiser, and the mixture fraction of the flows are within the flammability limits, a so-called twin flame with two premixed flame fronts appears (figure 1.4a). If one of the flows contains no fuel and the other flow contains no oxidiser, a single diffusion flame appears around the position where the mixture fraction is equal to its stoichiometric value (figure 1.4c). All other combinations of fuel and oxidiser can be considered as partially-premixed flames (figure 1.4b). The partially-premixed
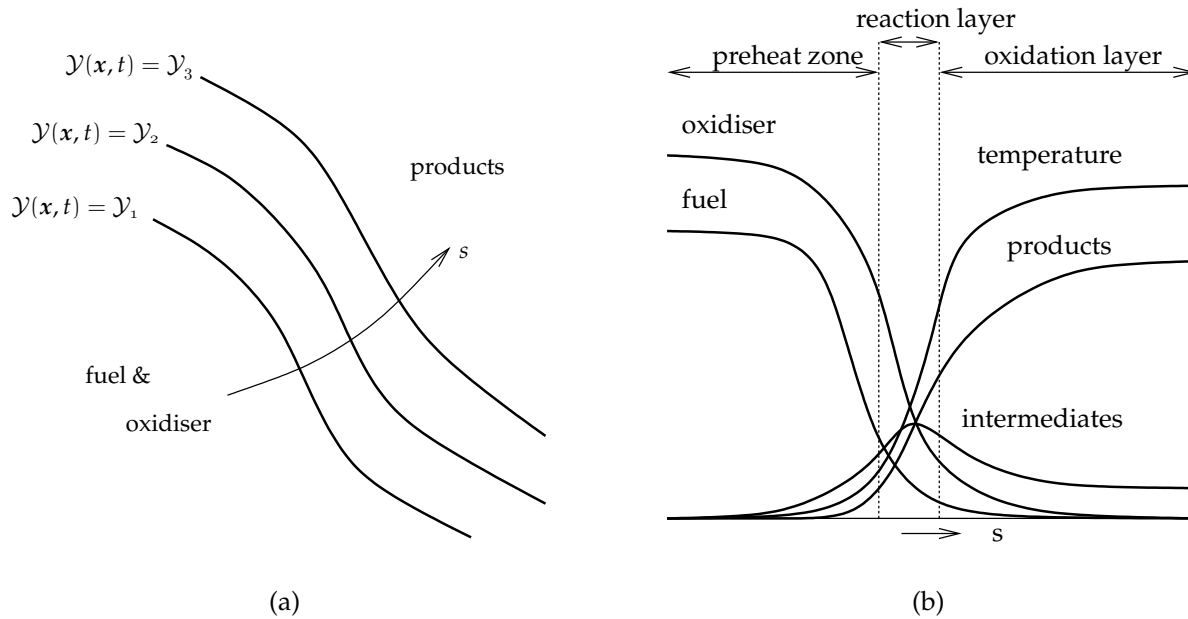
Figure 1.2 :   A schematic representation of a premixed flame.   The left figure shows a schematic example of a premixed flame front, whereas the right figure schematically shows the internal structure of the premixed flame, as a function of the coordinate s.

flame shown in figure 1.4b is formed by a rich premixed and a lean premixed jet. In this case, both the inlet mixtures are within the flammability limit, so two premixed flame fronts appear. Between the premixed flame fronts, a diffusion flame front appears, where the remaining fuel from the rich premixed flame reacts with remaining oxidiser from the lean premixed flame. In chapter 4, the counterflow configuration is used to test the FGM method, which is based on the solution of premixed flames, in a partially-premixed system. The major benefit of testing the FGM method in this configuration, is that the gradient of the mixture fraction Z can be controlled directly.

1.3   Outline of this thesis

In chapter 2, the equations that are used to model combuston processes are presented. The general conservation laws are derived. In addition, several closure models that are needed to complete the system of equations are given. Furthermore, a number of transport models is tested in a flame configuration, which is premixed and one-dimensional.

In chapter 3, the general principles of chemical reduction methods are presented. As reduction methods are generally based on steady-state assumptions of fast chemical processes, a time scale analysis of transport and chemical processes in flames is presented. Furthermore, a number of reduction methods is highlighted briefly. The
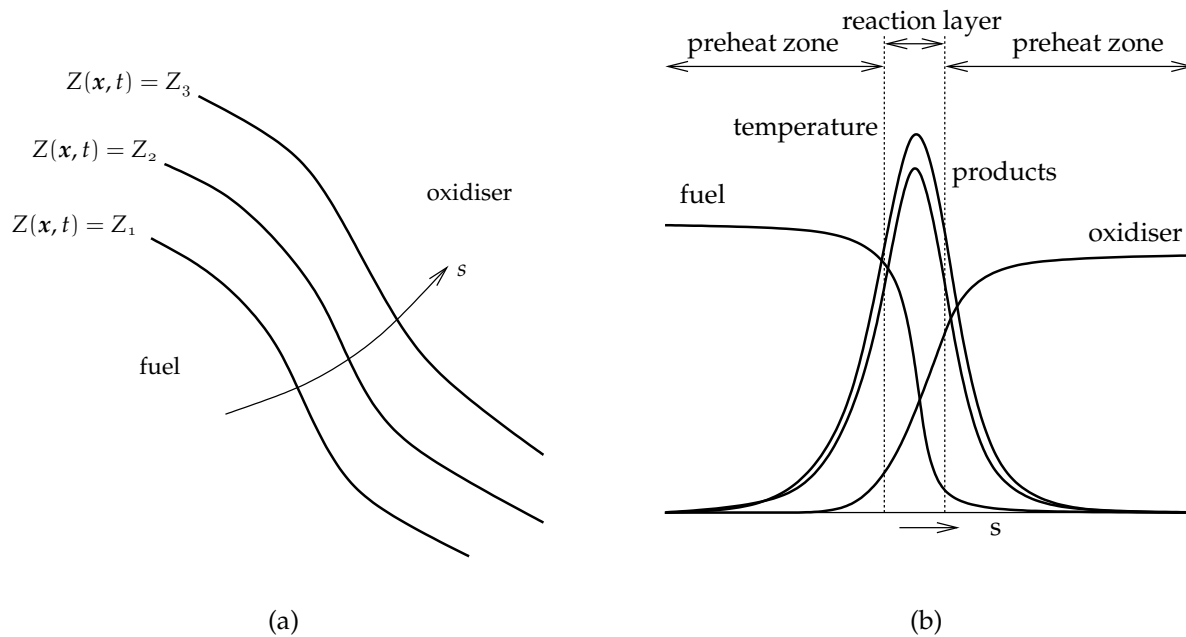
Figure 1.3 : A schematic representation of a non-premixed flame. The left figure shows a schematic example of a non-premixed flame front, whereas the right figure schematically shows the internal structure of the non-premixed flame, as a function of the coordinate s.

ILDM method and the FGM method are treated in more detail, as these methods are used in the remainder of the thesis.

In chapter 4, the FGM method is applied to a one-dimensional counterflow flame configuration, which is partially-premixed (see figure 1.4). A comparison is made with detailed computations and a standard non-premixed flamelet model. The accuracy of the FGM method is evaluated by means of a time scale analysis of the chemical and transport processes.

In chapter 5, a new reduction method is introduced, which will be referred to as the Phase-Space Intrinsic Low-Dimensional Manifold (PS-ILDM) method. As stated in the first section of this chapter, one of the objectives of this research is the possibility to combine the benefits of the ILDM and the FGM method in a new reduction method. First, the equations that are used to define a PS-ILDM are derived. The principles of the method are demonstrated by means of a simple but illustrative example. In addition, manifolds are computed for several fuels and applied in a simple flame configuration. Finally, in chapter 6, a number of conclusions is drawn.
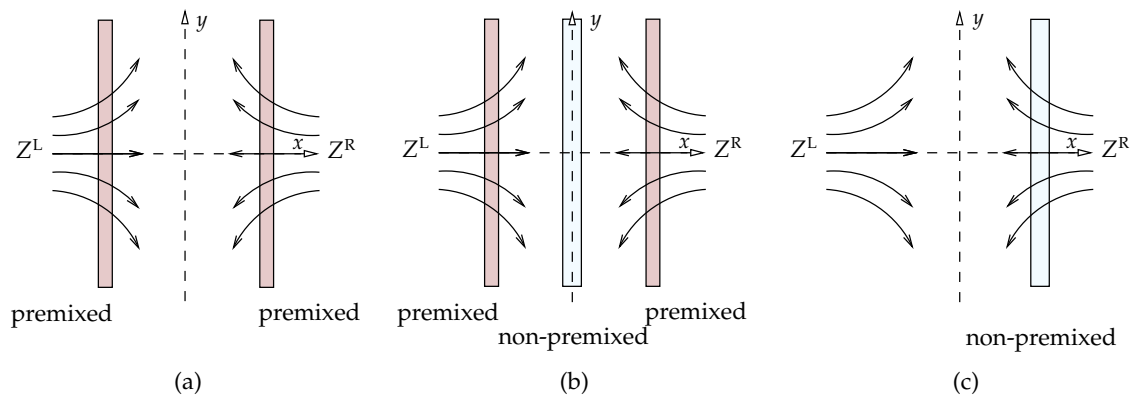
Figure 1.4 : A schematic representation of three counterflow flames. The arrows indicate the flow direction and the flame fronts are represented by the grey regions. The left figure shows a twin flame with two premixed flame fronts. The right figure is an example of a non-premixed flame. The counterflow flame in the middle is an example of a partially-premixed counterflow flame with three flame fronts.

Chemically reacting flows

This chapter presents the transport equations that are used to describe chemically reacting flows. The analyses in the subsequent chapters are based on the equations presented in this chapter. In the first section, the general conservation equations of mass, momentum, energy and chemical components are given together with closure models for the pressure, the enthalpy and the flux terms. In section 2.2, an expression is derived for the chemical source term. In the third section, a number of transport models is discussed and tested, respectively. Finally in section 2.4, a short summary is given of the models that are used in the remainder of this thesis.

2.1 Governing equations

Chemically reacting flows can generally be described by a set of differential equations, representing the conservation of mass, momentum, species mass fractions and energy. The derivation of these equations can be found in, for instance, [96,99]. This section only presents the resulting equations.

2.1.1 General conservation equations

The continuity of mass is expressed by the continuity equation

$$\frac{\partial \rho}{\partial t} + \nabla \cdot (\rho \boldsymbol{u}) = 0, \tag{2.1}$$

where ρ is the mass density and $\boldsymbol{u} = (u, v, w)^{\mathrm{T}}$ is the mixture velocity. The momentum equation yields

$$\frac{\partial \rho \boldsymbol{u}}{\partial t} + \nabla \cdot (\rho \boldsymbol{uu}) = \nabla \cdot \boldsymbol{\Pi} + \sum_{i=1}^{N_{\mathrm{s}}} \rho Y_i \boldsymbol{b}_i, \tag{2.2}$$

with $\boldsymbol{\Pi}$ the stress tensor, Y_i the mass fraction of species i and $\boldsymbol{b}_i$ the external force per unit mass acting on the ith species. The mass fractions Y_i are defined as $Y_i = \frac{\rho_i}{\rho}$, where ρ_i is the mass density of species i. The stress tensor $\boldsymbol{\Pi}$ can be divided into a hydrostatic part and a viscous part according to $\boldsymbol{\Pi} = -p\boldsymbol{I} + \boldsymbol{\tau}$, where p, $\boldsymbol{I}$, and $\boldsymbol{\tau}$ are the hydrostatic pressure, the unit tensor and the viscous stress tensor, respectively.

For each chemical component $i \in [1, N_s]$, which is present in the mixture, a conservation equation can be formulated, yielding

$$\frac{\partial \rho Y_i}{\partial t} + \nabla \cdot (\rho \boldsymbol{u}_i Y_i) = s_i, \qquad i \in [1, N_s], \tag{2.3}$$

with $\boldsymbol{u}_i$ the specific velocity of species i. The chemical source term s_i represents the change of mass due to chemical reactions. The specific velocity is defined as $\boldsymbol{u}_i = \boldsymbol{u} + \boldsymbol{U}_i$, with $\boldsymbol{U}_i$ the diffusion velocity of species i. The combination of (2.3) and the definition of $\boldsymbol{u}_i$ results in the general equation for the species mass fractions,

$$\frac{\partial \rho Y_i}{\partial t} + \nabla \cdot (\rho \boldsymbol{u} Y_i) + \nabla \cdot (\rho \boldsymbol{U}_i Y_i) = s_i, \qquad i \in [1, N_s]. \tag{2.4}$$

Finally, the conservation of enthalpy h can be written as,

$$\frac{\partial \rho h}{\partial t} + \nabla \cdot (\rho h \boldsymbol{u}) = \frac{Dp}{Dt} + \boldsymbol{\tau} : (\nabla \boldsymbol{u}) - \nabla \cdot \boldsymbol{q} + \sum_{i=1}^{N_s} \rho Y_i (\boldsymbol{u} + \boldsymbol{U}_i) \cdot \boldsymbol{b}_i, \tag{2.5}$$

with $\boldsymbol{q}$ the heat flux vector. The convective derivative of the pressure is given by $\frac{Dp}{Dt} = \frac{\partial p}{\partial t} + \boldsymbol{u} \cdot \nabla p$.

2.1.2   State equations

The total enthalpy h is defined as the mass-weighted sum of the specific enthalpies h_i, which follow from the caloric equation of state, i.e.

$$h = \sum_{i=1}^{N_s} Y_i h_i, \qquad h_i(T) = h_i^{\text{ref}} + \int_{T^{\text{ref}}}^{T} c_{p,i} d\tau, \qquad i \in [1, N_s], \tag{2.6}$$

with $c_{p,i}$ and h_i^{ref} being the specific heat and the enthalpy of formation of species i at reference temperature T^{ref}, respectively. The overall heat capacity at constant pressure c_p is given by

$$c_p = \sum_{i=1}^{N_s} Y_i c_{p,i}. \tag{2.7}$$

The specific heat $c_{p,i}$ and enthalpy h_i can be obtained from well tabulated polynomial fits [51].

The partial pressure of species i follows from the thermal equation of state. It is assumed that all chemical components in the flame behave like an ideal gas. In that case, the thermal equation of state is given by,

$$p_i = n_i R T = n X_i R T, \qquad i \in [1, N_s], \tag{2.8}$$

with R and n the universal gas constant and the total molar concentration, respectively. In addition, p_i, n_i, and X_i are the pressure, the molar concentration and the

mole fraction of species i, respectively. The mole fractions are defined as $X_i = \frac{n_i}{n}$ and are related to the mass fractions Y_i, according to

$$\frac{X_i}{\bar{M}} = \frac{Y_i}{M_i} = \phi_i, \qquad i \in [1, N_s], \tag{2.9}$$

with ϕ_i, M_i, and $\bar{M} = \sum_{i=1}^{N_s} X_i M_i$ being the specific mole number, the molar mass of species i and the average molar mass of the mixture, respectively. Combination of Eqs. (2.8) and (2.9), while using $\rho = n\bar{M}$, leads to

$$p_i = \rho R T \phi_i, \qquad i \in [1, N_s]. \tag{2.10}$$

The total pressure is equal to sum of the partial pressures of all species, thus given by

$$p = \sum_{i=1}^{N_s} p_i = \sum_{i=1}^{N_s} \rho R T \phi_i. \tag{2.11}$$

2.1.3 Transport fluxes

To be able to solve the conservation equations, expressions for the flux terms $\boldsymbol{U}_i$, $\boldsymbol{q}$ and $\boldsymbol{\tau}$ are needed. A complete description of the diffusion velocities $\boldsymbol{U}_i$, following from the kinetic theory of gases [30], is given by

$$\boldsymbol{U}_i = -\sum_{j=1}^{N_s} D_{ij} \boldsymbol{d}_j - D_i^T \boldsymbol{\nabla} \log T \qquad i \in [1, N_s], \tag{2.12}$$

where D_{ij} are the multicomponent diffusion coefficients of species i in species j and D_i^T are the thermal diffusion coefficients of species i. The second term on the right-hand side of equation (2.12) is known as the Soret effect or the thermal diffusion effect. Thermal diffusion tends to drive light species towards the hotter parts and heavy species towards colder parts of the mixture [99]. The vectors $\boldsymbol{d}_i$ incorporate the effects of various state variable gradients and external body forces [98] and are given by

$$\boldsymbol{d}_i = \boldsymbol{\nabla} X_i + (X_i - Y_i)\boldsymbol{\nabla}\log p + \frac{\rho}{p}\sum_{j=1}^{N_s} Y_i Y_j (\boldsymbol{b}_j - \boldsymbol{b}_i), \qquad i \in [1, N_s]. \tag{2.13}$$

Pioneering work on multicomponent transport modelling in flames was presented by Dixon-Lewis [19]. He showed that thermal diffusion especially effects the profiles of light species. On the other hand, Rosner *et al.* [82] showed that the Soret effect related to heavy species plays an important role in soot formation and during the vaporisation process in spray combustion. Furthermore, previous studies have shown that thermal diffusion has an important effect on the flame structure in two-dimensional simulations of hydrogen/air and methane/air Bunsen flames [32] and

hydrogen jet diffusion flames [45]. In addition, an accurate description of the heat fluxes is necessary in the modelling of flames near a wall [80]. Unfortunately, the evaluation of the diffusion coefficients D_{ij} and the thermal diffusion coefficients D_i^T is a CPU-intensive task, because a matrix inversion is required. Therefore, in many applications simpler expressions for the diffusion velocities are used. Some of these expressions will be discussed in section 2.3.3 and tested in section 2.3.4.

The heat flux vector q is given by

$$q = \rho \sum_{i=1}^{N_s} U_i Y_i h_i - \lambda' \nabla T + p \sum_{i=1}^{N_s} D_i^T d_i + q_R, \tag{2.14}$$

with λ', and q_R being the partial thermal conductivity and the radiative flux vector, respectively. In the flames studied in this thesis, radiation is neglected. The term with D_i^T in equation (2.14) is known as the Dufour effect, which is in fact the counterpart of the Soret effect in equation (2.12).

The last unknown flux term in the conservation equations is the stress tensor $\boldsymbol{\tau}$. An expression for τ follows from the kinetic theory

$$\boldsymbol{\tau} = (\kappa - \frac{2}{3}\eta)(\nabla \cdot u)I - \eta(\nabla u + (\nabla u^T)), \tag{2.15}$$

with p, κ and η being the hydrostatic pressure, the volume viscosity and the shear viscosity respectively. Generally in flame simulations, the volume viscosity is neglected [96].

2.2 Chemical reactions

This section presents the derivation of the chemical source term s_i, introduced in equation (2.3). The chemical source term describes the rate of change of chemical components due to chemical reactions. The conversion of a general hydrocarbon $C_aH_bO_c$, which is completely converted, can be described by the global reaction

$$C_aH_bO_c + \nu O_2 \rightarrow aCO_2 + \frac{b}{2}H_2O, \tag{2.16}$$
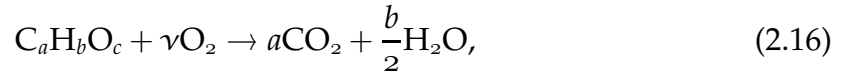
with ν the stoichiometric fraction, which is specific for each hydrocarbon. For example, the global reaction for the conversion of methane is given by

$$CH_4 + 2O_2 \rightarrow CO_2 + 2H_2O. \tag{2.17}$$

The global reaction is the result of a large number of elementary reactions. Each elementary reaction $k \in [1, N_r]$ can be written as

$$\nu'_{1k}A_i + \cdots + \nu'_{N_sk}A_{N_s} \leftrightarrows \nu''_{1k}A_1 + \cdots + \nu''_{N_sk}A_{N_s}, \tag{2.18}$$
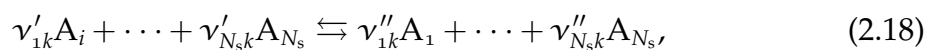
where A_i, v'_{ik}, and v''_{ik} denote a chemical component and the number of molecules of type i that are consumed and produced during reaction k, respectively. A typical elementary reaction is, e.g.

$$H + O_2 \leftrightarrows OH + O. \tag{2.19}$$

It is assumed that the reaction rate r^f of the forward reaction, i.e. from left to right, is proportional to the concentration of the reactants, hence,

$$r^f = k^f[H][O_2], \tag{2.20}$$

where the reaction rate coefficient k^f is generally given by a modified Arrhenius equation [96],

$$k^f = AT^\beta \exp\left(\frac{-E_a}{RT}\right). \tag{2.21}$$

In this equation, A, β, and E_a are reaction constants and the activation energy, respectively. The rate of change of the species, which are involved in the forward reaction of (2.19), is given by

$$\frac{d[H]}{dt} = \frac{d[O_2]}{dt} = -\frac{d[OH]}{dt} = -\frac{d[O]}{dt} = -r^f. \tag{2.22}$$

The rate of change caused by the reverse reaction is analogous. The resulting reaction rate r of this reaction is given by the difference between the forward and the backward reaction rate, i.e.

$$r = r^f - r^b = k^f[O_2][H] - k^b[OH][O]. \tag{2.23}$$

For a general reaction (2.18) with index k, the reaction rate is thus given by

$$r_k = k_k^f \prod_{i=1}^{N_s} (n_i)^{v'_{ik}} - k_k^b \prod_{i=1}^{N_s} (n_i)^{v''_{ik}}, \qquad k \in [1, N_r]. \tag{2.24}$$

The reaction rate coefficient k^b of the backward reaction can be obtained using the equilibrium constant $k^{eq} = k^f/k^b$, which is a function of the thermodynamic properties of the chemical components that are involved in the reaction. Finally, the chemical source term s_i of species i is given by

$$s_i = M_i \sum_{k=1}^{N_r} (v_{ik''} - v_{ik'}) r_k, \qquad i \in [1, N_s]. \tag{2.25}$$

2.3   Evaluation of transport coefficients

The transport coefficients that arise in the conservation equations (2.12), (2.14), and (2.15) are the diffusion coefficients D_{ij}, the thermal diffusion coefficients D_i^T, the

partial thermal conductivity λ', and shear viscosity η. The evaluation of these coefficients is an expensive and difficult task. Therefore, approximations of these coefficients are often used in practical applications. This section presents an overview of several transport models, starting from detailed transport models, which are obtained from the kinetic theory. Furthermore, the models are tested in a one-dimensional premixed flame configuration.

2.3.1 Multi-component diffusion

The kinetic theory does not provide explicit expressions for the transport coefficients. To obtain the transport coefficients, a linear system must be solved. These linear systems are usually referred to as transport linear systems (TLS) [29]. The multi-component diffusion equation, derived from the kinetic theory is given by

$$
\begin{aligned}
\boldsymbol{d}_i \;=\; & \sum_{j=1}^{N_s} \frac{X_i X_j}{\mathcal{D}_{ij}} (\boldsymbol{U}_j - \boldsymbol{U}_i) + \\
& \sum_{j=1}^{N_s} \left[\left(\frac{X_i X_j}{\rho \mathcal{D}_{ij}} \right) \left(\frac{D_j^T}{Y_j} - \frac{D_i^T}{Y_i} \right) \right] \boldsymbol{\nabla} \log T, \qquad i \in [1, N_s],
\end{aligned}
\tag{2.26}
$$

where $\mathcal{D}_{ij}$ are the binary diffusion coefficients [48]. As most combustion processes take place at a velocity which is much lower than the speed of sound, pressure is often assumed to be constant. Furthermore, the body-forces are assumed to be equal for all species and thermal diffusion is neglected [99]. With these assumptions, the multi-component diffusion equation reduces to the well-known Stefan-Maxwell equation [63,64],

$$
\boldsymbol{\nabla} X_i = \sum_{j=1}^{N_s} \frac{X_i X_j}{\mathcal{D}_{ij}} (\boldsymbol{U}_j - \boldsymbol{U}_i), \qquad i \in [1, N_s].
\tag{2.27}
$$

To find the solution of (2.26) is a complicated and CPU-intensive task, because a matrix has to be inverted. In addition, the system is singular. To remove the singularity, Hirschfelder et al. [48] proposed to take the diagonal elements D_{ii} of the diffusion matrix equal to zero. However, this assumption leads to a non-symmetric diffusion matrix, which is incompatible with Onsagers reciprocity relations for irreversible thermodynamics and therefore less useful in chemically reacting flows [18,94]. The coefficients used here, are the diffusion coefficients proposed by Waldmann and Trübenbacher [95]. These coefficients meet the Onsagers reciprocity relations, leading to a symmetrical diffusion coefficient matrix with positive diagonal terms. The diffusion coefficients are computed with the transport library EGLIB by Ern and Giovangigli [31]. The diffusion matrix computed by EGLIB is symmetric. Furthermore, it satisfies the constraint $\sum_{i=1}^{N_s} Y_i D_{ij} = 0$ such that $\sum_{i=1}^{N_s} Y_i \boldsymbol{U}_i = 0$.

In the EGLIB library, the TLS is solved in a computationally efficient manner, using a conjugated gradient method, cf. [42]. This method resulted in a new expression for the diffusion matrix **D**. The procedure has lead to a new expression for the diffusion coefficients D_{ij}. Ern and Giovangigli showed that the diffusion matrix can be approximated by a convergent series expansion

$$\mathbf{D}^{[k]} = \sum_{l=0}^{k} (\mathbf{P}(\mathbf{I} - \boldsymbol{\Upsilon}\boldsymbol{\Delta}))^{l}\mathbf{P}\boldsymbol{\Upsilon}\mathbf{P}^{\mathrm{T}}, \tag{2.28}$$

where P is a projection matrix, given by $P_{ij} = \delta_{ij} - Y_j$ for $i, j \in [1, N_{\mathrm{s}}]$, with δ_{ij} the Kronecker delta. The matrix $\boldsymbol{\Delta}$ is given by

$$\Delta_{ii} = \sum_{j=1, j \neq i}^{N_{\mathrm{s}}} \frac{X_i X_j}{\mathcal{D}_{ij}}, \qquad i \in [1, N_{\mathrm{s}}], \tag{2.29}$$

$$\Delta_{ij} = \frac{X_i X_j}{\mathcal{D}_{ij}}, \qquad i, j \in [1, N_{\mathrm{s}}], \qquad i \neq j. \tag{2.30}$$

Finally, $\boldsymbol{\Upsilon}$ is a diagonal matrix given by $\boldsymbol{\Upsilon} = \mathrm{diag}\,(D_{1m}/X_1, \ldots, D_{N_{\mathrm{s}}m}/X_{N_{\mathrm{s}}})$, where D_{im} are the mixture-averaged diffusion coefficients [47], obtained from

$$D_{im} = \frac{1 - Y_i}{\sum_{j \neq i}^{N} X_j/\mathcal{D}_{ij}}, \qquad i \in [1, N_{\mathrm{s}}]. \tag{2.31}$$

The diffusion coefficient D_{im} denotes the diffusion of species i into the mixture. The binary diffusion coefficients $\mathcal{D}_{ij}$ are obtained from fitted polynomials [51].

The first term in the series expansion, i.e. $\mathbf{D}^{[0]}$, corresponds to a mixture-averaged diffusion model [47], with a corrected diffusion velocity [49, 73]. This model will be discussed briefly later in this section. The second term in the series expansion corresponds to a new expression for the diffusion matrix, first introduced by Ern and Giovangigli, cf. [29].

2.3.2   Other transport coefficients

In addition to the diffusion coefficients D_{ij} and the thermal diffusion coefficients D_i^T, the shear viscosity η and the partial thermal conductivity λ' can also be obtained by solving the transport linear system, hence with the EGLIB library. However, this is a CPU intensive operation. In literature, several expressions for the shear viscosity are found. For instance, the mixture-averaged shear viscosity η according Wilke's approximation is given by [97]

$$\eta = \sum_{i=1}^{N} \frac{X_i \eta_i}{\sum_{j=1}^{N} X_j \Phi_{ij}}, \tag{2.32}$$

with η_i the viscosity of species i. The parameter Φ_{ij} is given by

$$\Phi_{ij} = \frac{1}{\sqrt{8}} \left(1 + \left(\frac{M_i}{M_j} \right)^{-\frac{1}{2}} \right) \left(1 + \left(\frac{\eta_i}{\eta_j} \right)^{-\frac{1}{2}} \left(\frac{M_j}{M_i} \right)^{-\frac{1}{4}} \right)^2. \tag{2.33}$$

In the calculations with simplified diffusion models, an approximation for the partial thermal conductivity coefficients λ' is used [61].

$$\lambda' \approx \frac{1}{2} \left(\sum_{i=1}^{N_s} X_i \lambda_i + \left(\sum_{i=1}^{N_s} X_i / \lambda_i \right)^{-1} \right), \tag{2.34}$$

with λ_i the conductivity of species i. This approximation has hardly any effect on the burning velocity, so it can be used without further consequences. The values of the viscosities η_i and conductivities λ_i are obtained from fitted polynomials [51].

A more simple relation for η and λ' is obtained by a fitted exponential function [86],

$$\frac{\eta}{c_p} = \alpha_1 \left(\frac{T}{T^{\text{ref}}} \right)^{\beta_1}, \tag{2.35}$$

and

$$\frac{\lambda'}{c_p} = \alpha_2 \left(\frac{T}{T^{\text{ref}}} \right)^{\beta_1}, \tag{2.36}$$

with $T^{\text{ref}} = 298$ K. The fit parameters α_1, α_2, β_1, and β_2 are obtained from detailed computations. Smooke and Giovangigli [86] found that η/c_p and λ'/c_p do not strongly depend on pressure, neither do they strongly depend on the stoichiometry of the mixture, at least for lean methane/air mixtures. In section 2.3.4, the fit parameters for several flames are presented.

2.3.3 Approximating diffusion models

This section gives an overview of several empirical diffusion models, which are used to save computing time. First, a so-called mixture-averaged model with different flux corrections is presented. Subsequently, a model with constant non-unit Lewis numbers and a model with unit Lewis numbers is given. The user manual of CHEMKIN [51] also presents an overview of several approximating models, but in this work the number of empirical models is restricted. An overview of a number of approximating models is given by Coffee and Heimerl [16,17].

The first term in the series expansion (2.28) is given by

$$\mathbf{D}^{[0]} = \mathbf{P} \boldsymbol{\Upsilon} \mathbf{P}^{\text{T}}. \tag{2.37}$$

This expression corresponds to a mixture-averaged diffusion model [47], with a mass correction diffusion velocity. The symmetric projection with $\mathbf{P}$ ensures symmetry of the diffusion matrix, so that it satisfies Onsagers reciprocity conditions.

Another often used approximation for the diffusion matrix can be written as

$$\mathbf{D} = \mathbf{P}\boldsymbol{\Upsilon}. \tag{2.38}$$

This corresponds with a mixture-averaged diffusion velocity with a constant correction velocity for all species. The corrected velocity is given by $\boldsymbol{U}_i^c = \boldsymbol{U}_i - \sum_{j=1}^{N_s} Y_j \boldsymbol{U}_j$ [78], where the diffusion velocity is given by

$$\boldsymbol{U}_i = -\frac{D_{im}}{X_i}\nabla X_i - \frac{D_i^T}{T}\nabla T, \qquad i \in [1, N_s]. \tag{2.39}$$

However, this method leads to a non-symmetric diffusion matrix. Finally, it is possible to use Eq. (2.39) to calculate the diffusion velocities and to obtain mass conservation by applying a correction only to the species with the largest mole fraction, i.e. $Y_{N_s} = 1 - \sum_{i=1}^{N_s-1} Y_i$. It can be shown that this correction may induce counter gradient diffusion of the N_s-th species [78]. However, this effect is negligible if the concentration of this species is large.

In many occasions the fluctuation of the mean mass $\bar{M}$ is neglected, so the expression (2.39) for the diffusion velocity can then be written as [87]

$$\boldsymbol{U}_i = -\frac{D_{im}}{Y_i}\nabla Y_i - \frac{D_i^T}{T}\nabla T, \qquad i \in [1, N_s]. \tag{2.40}$$

The advantage of this expression, is that the conservation equation for the species mass fractions is now entirely written in terms of Y_i. However, because the mixture-averaged model is mainly used in numerical studies, it is preferable to include the fluctuation of $\bar{M}$.

For analytical purposes, Eq. (2.40) can be rewritten according to

$$\boldsymbol{U}_i = -\frac{1}{\mathrm{Le}_i}\frac{\lambda'}{\rho Y_i c_p}\nabla Y_i - \frac{D_i^T}{T}\nabla T, \qquad i \in [1, N_s], \tag{2.41}$$

where the Lewis number is introduced as $Le_i = \frac{\lambda'}{c_p \rho D_{im}}$. The Lewis numbers can not be chosen independently for all species. To preserve mass conservation, a correction must be applied. For instance, the last Lewis number can be obtained from the condition $\sum_{i=1}^{N_s} Y_i \boldsymbol{U}_i = 0$. In most evaluations, the Lewis number of the last species Le_{N_s} is undefined and Y_{N_s} is evaluated from the condition $\sum_{i=1}^{N_s} Y_i = 1$. In a first approximation, the Lewis numbers are assumed to be constant. This assumption is based on the fact that variations of the Lewis numbers are small in a large part of the flame. For methane/air flames, this is shown in [86] and [78]. For the other flame types studied in this work, the variations in the Lewis numbers are larger, which leads to larger deviations in the burning velocity. In an even more simplified model, the mass flux and heat flux are assumed to be equal, i.e. $Le_i = 1$. This model is often used in theoretical studies. It has the advantage that the enthalpy and element fractions are constant in premixed flames, since preferential diffusion does not occur.

2.3.4   Test results

This section presents test results of several transport models. First, different expressions for the diffusion velocities are tested in one-dimensional methane and hydrogen flames. Subsequently, the effect of thermal diffusion is investigated and finally different fits for the partial thermal conductivity and the viscosity are presented. All computations are performed with CHEM1D [12]. Note that in the analysis presented below, only an impression is given of the accuracy of the approximating models. The final choice for a transport model depends on the application, for which the model is used.

The effect of simplified diffusion models

The effect of simplified diffusion models will be compared for the different flames (Fig. 2.1). The models are tested on 1D adiabatic CH_4/air, CH_4/O_2, H_2/air and H_2/O_2 flames, with an inlet temperature of 298 K and pressure of 1 atm. The flames are simulated with the GRI 2.11 reaction mechanism containing 49 species and 279 reactions [8]. A similar study has been performed by Coffee and Heimerl [16, 17]. However, in this thesis, the research is extended to a wide range of the equivalence ratio and to CH_4/O_2-flames. The following models are considered:

1. Detailed multi-component diffusion model: $\mathbf{D}^{[1]}$, i.e. equation (2.28).

2. Mixture-averaged model with a symmetric correction velocity: $\mathbf{D}^{[0]} = \mathbf{P}\boldsymbol{\Upsilon}\mathbf{P}^{\mathrm{T}}$, i.e. equation (2.37).

3. Constant non-unit Lewis numbers, i.e. equation (2.41). The Lewis numbers are obtained from the second model at $\varphi = 1$.

4. Unit Lewis numbers.

In all these models, the Soret and Dufour effect is neglected. The last model is crude but included here, because it is used in many analytical studies. In the figures here, the burning velocity s_L is presented for a varying equivalence ratio φ.

For all flame types, it can be observed that for low values of φ, the choice of the diffusion model is insignificant. For larger values of φ, however, the effect of the simplified diffusion models becomes more important. In most cases the simplest model, i.e. unit Lewis numbers, results in a poor prediction of the burning velocity. As stated above, this model is included as it is used in many analytical studies. The results show that one has be cautious with the results obtained with this assumption, if s_L is an important parameter in the analysis. In the following, the other three models will be compared.

For CH_4/air flames, the simple models 2 and 3 perform quite well. Even the model with constant Lewis numbers gives a good prediction of the burning velocity. Similar results (model 2) were obtained by Ern and Giovangigli [33]. However,

Table 2.1 :   Burning velocity s_L [cm/s] at $\varphi = 1$ obtained with a mixture-averaged diffusion model and different correction methods.

Correction/flame	CH_4/air	CH_4/O_2	H_2/air	H_2/O_2
$\mathbf{D}^{[0]} = \mathbf{P}\boldsymbol{\Upsilon}\mathbf{P}^T$	38.39	309.7	255.3	1053
$\mathbf{D} = \mathbf{P}\boldsymbol{\Upsilon}$	38.51	309.2	256.4	1053
Corr. on Y_{N_s} only	38.51	309.2	256.4	1053
$\mathbf{D}=\mathbf{P}\boldsymbol{\Upsilon}$ and $\nabla\bar{M}$ negl.	37.85	314.2	249.9	1048

the absolute values of s_L are different, probably caused by using a different reaction mechanism. For the other flame types, model 3 may lead to larger errors. As mentioned earlier, this is caused by the fact that the variations in the Lewis numbers are much larger for these flame types (in the order of 50 % for some species in hydrogen flames). The effect of the approximations is most dramatically shown by the H_2/O_2 flame. Even a mixture-averaged transport model can induce an error in the prediction of the burning velocity of up to 10%.

It should be noticed that part of the error in the results obtained with model 3 is induced by the neglect of the variation of the mean molar mass. To give an indication of the effect of this neglect, burning velocities obtained with a mixture-averaged diffusion model including the variation of $\bar{M}$ (2.39) are compared with results obtained without the variation of $\bar{M}$ taken into account (2.40). Table 2.1 shows that neglecting the fluctuation of $\bar{M}$ may lead to errors of 2-3%.

Finally, table 2.1 also shows that the effect of the three different flux corrections (2.37), (2.38) and the correction on Y_{N_s} only) on the burning velocity is negligible compared to deviations induced by the choice of the diffusion model. Therefore, the burning velocities obtained with the several correction methods are not shown in the figures.

The effect of thermal diffusion

In the second test case, the effect of thermal diffusion on the burning velocity is tested. Even though it makes no sense to neglect the Soret effect during multi-component transport computations since the additional computing time is negligible. However, it is interesting to study the influence of this effect separately on the burning velocity. The influence of thermal diffusion is studied with the following models (Fig. 2.2):

1. Soret and Dufour effect neglected.

2. Soret effect taken into account and Dufour effect neglected.

3. Soret and Dufour effect taken into account.

Table 2.2 :   Fit parameters for η/c_p and λ'/c_p for different flames.

Parameters	CH$_4$/air			C$_{12}$H$_{26}$/air	
	Smooke [86]	atmospheric	gas turb.	atmospheric	gas turb.
$\alpha_1 \times 10^4$	—	1.68	1.76	1.60	1.68
β_1	—	0.51	0.51	0.56	0.56
$\alpha_2 \times 10^4$	2.58	2.59	2.61	2.38	2.24
β_2	0.7	0.71	0.69	0.75	0.77

The models are tested on the same flames (CH$_4$/air, CH$_4$/O$_2$, H$_2$/air and H$_2$/O$_2$) as the diffusion models. In all these models, mass diffusion is described with the detailed multi-component diffusion model. The results show that the Dufour effect has hardly any effect on the burning velocity. The impact of the Soret effect can be much larger. The results show that for small values of φ, the effect of thermal diffusion is small. For larger values of φ, the Soret effect becomes more important. The influence of this effect is especially large for rich H$_2$/air flames. This result is in correspondence with earlier obtained results [43]. Neglecting thermal diffusion can lead to an increase of the burning velocity by almost 10%.

Fit parameters for the viscosity and the partial conductivity

In the third test, different fits for the partial thermal conductivity λ' and the viscosity are presented. The models are tested for different flame types, with different fuels and at different conditions. The fit parameters for the λ'/c_p relation (2.36), which are presented in [86] are fitted on a stoichiometric methane/air flame, at atmospheric conditions with an initial temperature of 298 K. To verify the fits presented here, the fit by Smooke and Giovangigli is reproduced. The fit parameters found for this flame type are presented in table 2.2. From the table, it can be concluded that the new fit parameters are in correspondence with the results of Smooke and Giovangigli, which are also given in table 2.2. The small deviation may be caused by a different distribution of the data points. A second fit is obtained from a methane/air flame at typical gas turbine conditions, i.e. at a pressure of 25 bar and with an initial temperature of 800 K and an equivalence ratio of $\varphi = 0.71$. For these conditions, the fit parameters for λ'/c_p and η only slightly deviate from the fit parameters at atmospheric conditions. This is also in correspondence with Smooke and Giovangigli, who also presented results for methane/air flames at higher pressures.

In a third and a fourth fit, a dodecane/air flame is evaluated. The flames are modelled with a reaction mechanism, which contains 38 species and 174 reactions [1]. In the third fit, a stoichiometric dodecane/air flame is used, at atmospheric conditions with an initial temperature of 298 K. In the fourth test, the parameters

are obtained from a dodecane/air flame with an equivalence ratio of $\varphi = 0.62$ at a pressure of 25 bar with an initial temperature of 800 K. The results for these tests are presented in table 2.2. From the table, it can be observed that for a dodecane/air flame, the η/c_p relation is more sensitive to the conditions, so one has to be careful using using the fitted expressions for dodecane flames.

2.4 Equations to be used in the remainder of this thesis

The conservation equations that are presented in the previous sections, contain a number of terms which are often neglected in combustion modelling. This section presents the equations that are used in the remainder of this thesis. Specifically, the terms that are neglected are: the body forces $\boldsymbol{b}_i$, the Soret and Dufour effects, pressure gradient diffusion (the second term on the right-hand side of equation (2.13)), the bulk viscosity κ and the radiant heat flux. An explanation for the neglect of these terms can be found in, e.g. [99]. In the subsequent chapters, the combustion model will be used to analyse chemical reduction methods. As stated in section 1.1.2, the main purpose of chemical reduction techniques is to reduce the computational costs of the combustion model, without losing too much accuracy. However, it is inevitable that some of the detailed information is lost if the model is reduced. Therefore, it is not useful to use a highly detailed diffusion model in the subsequent chapters. Furthermore, in section 2.3.4, it was shown that for fuel/air flames, the transport model with constant Lewis numbers gives relatively accurate results, at low computational costs. Therefore, this model is chosen for the remainder of this thesis. Hence, the diffusion velocity is given by

$$\boldsymbol{U}_i = -\frac{1}{\mathrm{Le}_i}\frac{\lambda'}{\rho Y_i c_p}\nabla Y_i \qquad i \in [1, N_\mathrm{s} - 1]. \tag{2.42}$$

An expression for $\boldsymbol{U}_{N_\mathrm{s}}$ can be obtained from the condition $\sum_{i=1}^{N_\mathrm{s}} Y_i \boldsymbol{U}_i = 0$. With the combination of (2.42), (2.6), and (2.7), the heat flux vector $\boldsymbol{q}$ can be written as

$$\boldsymbol{q} = -\frac{\lambda'}{c_p}\boldsymbol{\nabla}h - \frac{\lambda'}{c_p}\sum_{i=1}^{N_\mathrm{s}-1}\left(\frac{1}{Le_i} - 1\right)h_i^*\boldsymbol{\nabla}Y_i. \tag{2.43}$$

with $h_i^* = h_i - h_{N_s}$ [90]. With these expressions, the conservation equations can be written in the form as they are used in the remainder of this thesis,

$$\frac{\partial \rho}{\partial t} + \boldsymbol{\nabla} \cdot (\rho \boldsymbol{u}) \;=\; 0, \tag{2.44}$$

$$\frac{\partial \rho \boldsymbol{u}}{\partial t} + \boldsymbol{\nabla} \cdot (\rho \boldsymbol{u}\boldsymbol{u}) \;=\; \boldsymbol{\nabla} \cdot \boldsymbol{\Pi}, \tag{2.45}$$

$$\frac{\partial \rho Y_i}{\partial t} + \boldsymbol{\nabla} \cdot (\rho \boldsymbol{u} Y_i) - \boldsymbol{\nabla} \cdot \left(\frac{\lambda'}{Le_i c_p} \boldsymbol{\nabla} Y_i \right) \;=\; s_i, \qquad i \in [1, N_s - 1], \tag{2.46}$$

$$\sum_{i=1}^{N_s} Y_i \boldsymbol{U}_i \;=\; 0, \tag{2.47}$$

$$\sum_{i=1}^{N_s} Y_i \;=\; 1, \tag{2.48}$$

$$\tag{2.49}$$

and

$$\frac{\partial \rho h}{\partial t} + \boldsymbol{\nabla} \cdot (\rho h \boldsymbol{u}) - \boldsymbol{\nabla} \cdot \left(\frac{\lambda'}{c_p} \boldsymbol{\nabla} h \right) = \boldsymbol{\nabla} \cdot \left(\frac{\lambda'}{c_p} \sum_{i=1}^{N_s - 1} \left(\frac{1}{Le_i} - 1 \right) h_i^* \boldsymbol{\nabla} Y_i \right), \tag{2.50}$$

where it should be noticed that the pressure term and the viscous term are neglected in the enthalpy equation [81].
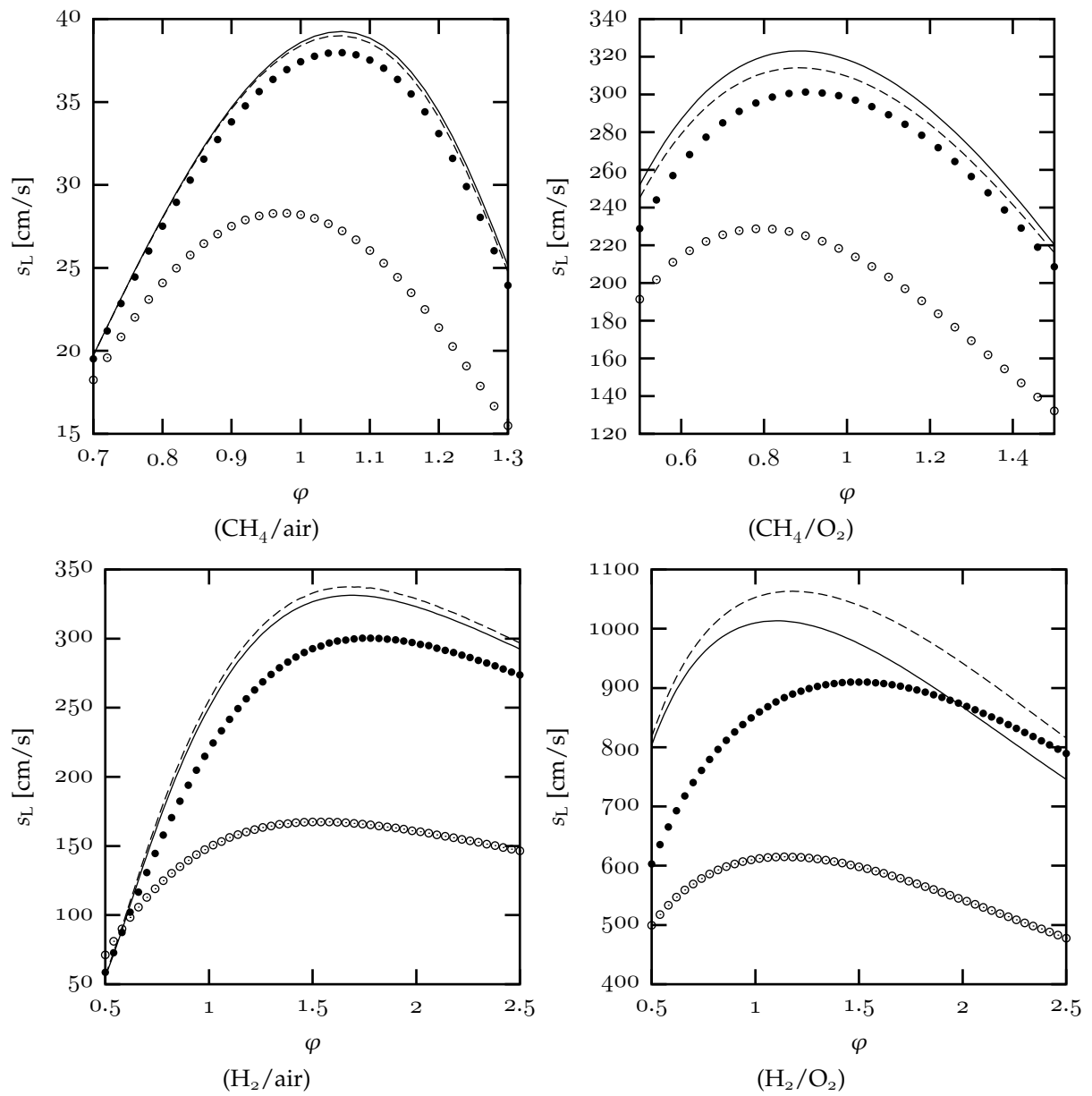
Figure 2.1 : The influence of different diffusion models on the burning velocity (solid: multi-component diff., dashed: mixture-averaged, solid circles: non-unit Lewis numbers, open circles: unit Lewis numbers)
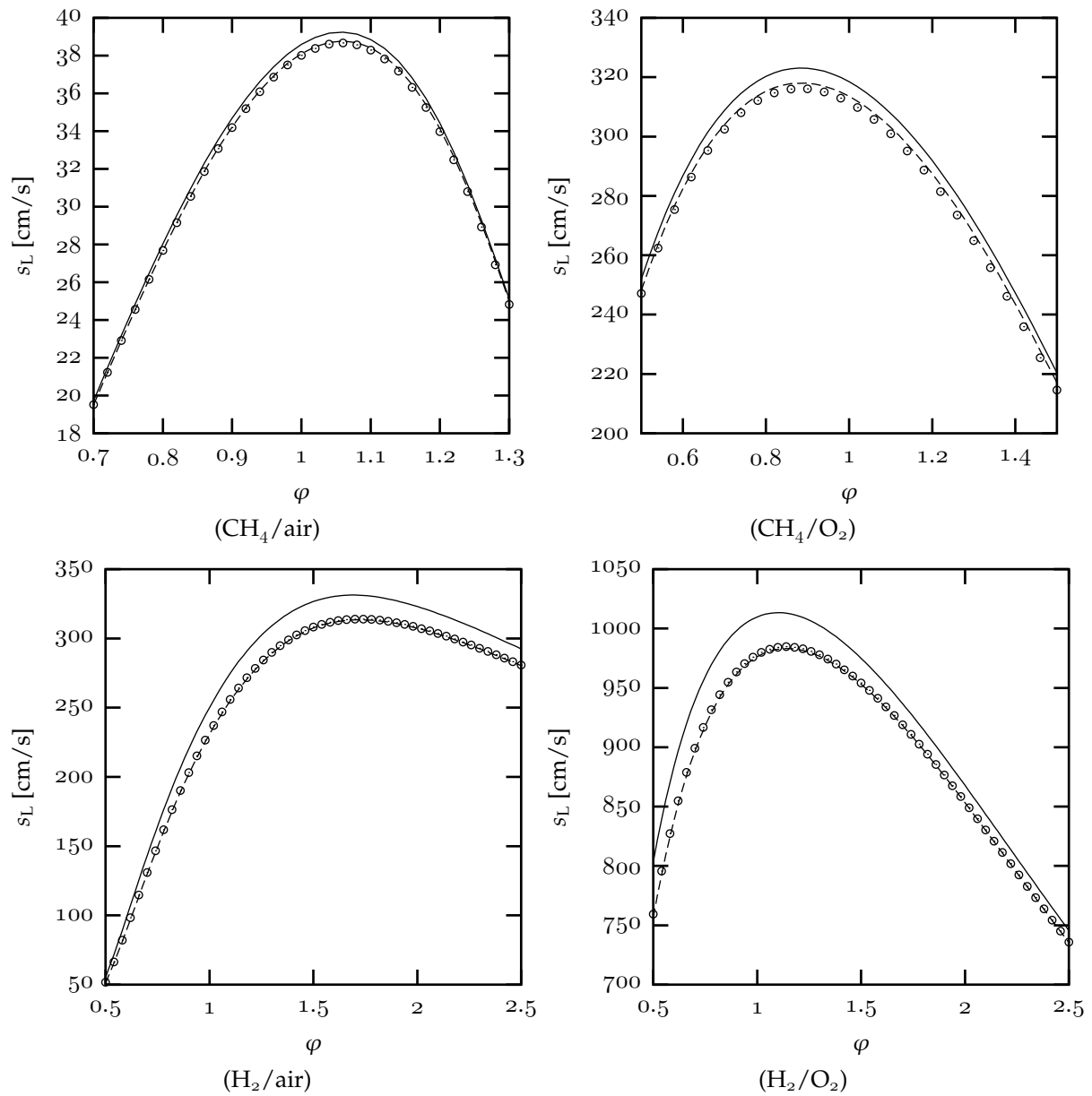
Figure 2.2 : The influence of the Soret and Dufour effect on the burning velocity (solid: No thermal diffusion, dashed: Soret effect taken into account, circles: Soret and Dufour effect taken into account)

Reduced chemistry

For the simulation of flames, the conservation equations for mass, momentum, enthalpy and chemical components need to be solved, i.e. equations (2.44), (2.45), (2.46), and (2.50). In general, chemical reaction mechanisms, which are needed to describe the chemical behaviour of flames, contain a large number of chemical components. For each component, a conservation equation has to be solved. As shown by equations (2.4) and (2.25), the conservation equations for the species are coupled by the highly nonlinear chemical source terms. In addition, the chemical source terms typically cover a wide range of time scales, which makes the set of conservation equations stiff [58]. To solve the system, advanced numerical methods or simpler methods with very small time steps are required. Even though two and three-dimensional simulations have been performed with detailed reaction mechanisms, see e.g. [13, 25, 66], their use in practical combustion simulations with complex geometries is still prohibited due to the long computation times. Part of the problems can be overcome by using advanced numerical methods, such as parallel computing [91], multi-grid methods [23] and local grid refinement [2, 3].

An alternative for the simulation of practical combustion applications, is the introduction of simplifications. In the past decades, two main approaches have been introduced: laminar flamelet models and chemical reduction techniques. Laminar flamelet models are based on the assumption that the flame front is much thinner than most of the flow length scales [74]. For that reason, the internal structure of the flame is almost frozen. During a CFD computation of a flame, the movement and the propagation of the flame front can be predicted by using the so-called $\mathcal{G}$-equation for premixed flames and the mixture fraction equation for non-premixed flames. The internal structure of the flame is obtained from a laminar flamelet library, which is defined in a preprocessing step.

Since most of the difficulties are caused by the chemical source term, it is most interesting to simplify the chemistry, by means of chemical reduction techniques. However, the accuracy should not be affected significantly. Generally, the reduction is achieved by reducing the number of unknown variables in the system, which results in a smaller set of equations that needs to be solved. In addition, much of the stiffness of system can be removed by applying steady-state assumptions for the fast processes. A straightforward method to reduce the size of the chemical system is achieved by replacing the detailed reaction mechanism by a small set of global

reactions. For instance, the set of detailed reactions can be replaced by a single global reaction, describing the conversion of fuel into products,

$$\text{Fuel} + \text{Oxidiser} \rightarrow \text{Products}. \qquad (3.1)$$
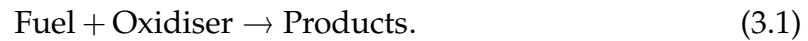
The reaction constants are obtained by fitting the results to experimental data, or data obtained by detailed computations. Due to the fitting, the global reaction mechanisms are only applicable to combustion simulations, which are closely related to the situation that was used during the fitting procedure. In addition, detailed information about radical profiles, which is needed to predict the amount of pollutant exhaust gases accurately, is not available.

More systematic reduction techniques that are used to simplify the chemistry are the so-called chemical reduction methods. In the past decades, a number of reduction methods has been introduced. Several of these methods will be discussed in the remainder of this chapter. In general, the reduction is achieved by applying steady-state assumptions for the fast processes. It is assumed that the chemical processes are dominated by a small number of slow processes and that it is sufficient to describe these slow processes accurately, since the fast processes adapt very rapidly to the slow processes.

This thesis focusses mainly on the further development of chemical reduction techniques. For further information on the principles of laminar flamelet techniques, the reader is referred to, e.g. [76]. This chapter presents the basic principles of chemical reduction methods. Furthermore, a number of methods is treated in more detail, as they are used in the remainder of this thesis. In the first section, the chemical processes that take place are analysed in a geometrical manner. Furthermore, the flow and chemical time scales of a premixed and a non-premixed flame are analysed. In the subsequent sections, the basic principles of chemical reduction techniques are treated. In the third and fourth section, the Intrinsic Low-Dimensional Manifold (ILDM) method and the Flamelet-Generated Manifold (FGM) method are treated in more detail, respectively. The FGM method can be seen as a combination of the laminar flamelet concept and chemical reduction techniques. In the final section, the ILDM method is compared with the FGM method.

3.1   Geometrical representation of the chemical system

The fundamentals of chemical reduction methods are more clear, if the chemical processes are described geometrically. Therefore, this section gives a geometrical representation of the chemical system. Consider a homogeneous system, which is

adiabatic and isobaric,

$$\rho \frac{\mathrm{d}\phi_i}{\mathrm{d}t} = \omega_i, \qquad i \in [1, N_s], \tag{3.2}$$

$$\frac{\mathrm{d}h}{\mathrm{d}t} = 0, \tag{3.3}$$

$$\frac{\mathrm{d}p}{\mathrm{d}t} = 0, \tag{3.4}$$

with $\omega_i = s_i/M_i$ the chemical source terms. The initial conditions of this system are given by $\phi_i(0) = \phi_i^o$, $h(0) = h^o$ and $p(0) = p^o$. At a certain time t, system (3.2-3.4) is completely determined by the state variables, i.e. the enthalpy h, the pressure p and the species mole numbers ϕ_i. The state of the mixture can be represented geometrically by a vector in the so-called N_{st}-dimensional *state space* $\mathcal{S}$, with $N_{st} = N_s + 2$. Therefore, equation system (3.2)-(3.4) can be written as

$$\frac{\mathrm{d}\boldsymbol{\Psi}}{\mathrm{d}t} = \boldsymbol{F}(\boldsymbol{\Psi}), \tag{3.5}$$

where $\boldsymbol{\Psi} = (\phi_1, \dots, \phi_{N_s}, h, p)^T$ is a vector in the state space and the corresponding source terms are given by the vector $\boldsymbol{F}(\boldsymbol{\Psi}) = (\omega_1/\rho, \dots, \omega_{N_s}/\rho, 0, 0)^T$. As the system is isobaric and adiabatic, it is sufficient to represent the evolution of the system in the N_s-dimensional *composition space* $\mathcal{C}$, in which h and p are conserved quantities. At a certain time t, the chemical composition is described by the vector

$$\boldsymbol{\phi} = (\phi_1, \dots, \phi_{N_s})^T \tag{3.6}$$

in the composition space $\mathcal{C}$. The chemical source terms ω_i can also be represented by a vector in the composition space, i.e. $\boldsymbol{\omega} = (\omega_1/\rho, \dots, \omega_{N_s}/\rho)^T$.

Chemical elements are conserved during a chemical reaction, which means that also the element mass fractions are conserved. The element mass fraction z_j of element j is defined as

$$z_j = \sum_{i=1}^{N_s} \eta_{ji} Y_i, \qquad j \in [1, N_e], \tag{3.7}$$

where η_{ji} is the mass fraction of element j in species i. In addition, the element mole number is defined as

$$\chi_j = \frac{z_j}{M_j^e} = \sum_{i=1}^{N_s} \mu_{ji} \phi_i = \boldsymbol{\mu}_j \cdot \boldsymbol{\phi} \qquad j \in [1, N_e], \tag{3.8}$$

with μ_{ji} the mole fraction of element j in species i and M_j^e is the molar mass of element j. The vector $\boldsymbol{\mu}_j$ can be seen as a normal vector to the $(N_s - 1)$-dimensional hyper-plane on which the element j is constant. The intersection of the N_e hyper-planes is the $(N_s - N_e)$-dimensional *reaction space* $\mathcal{R}$, in which all elements are conserved.
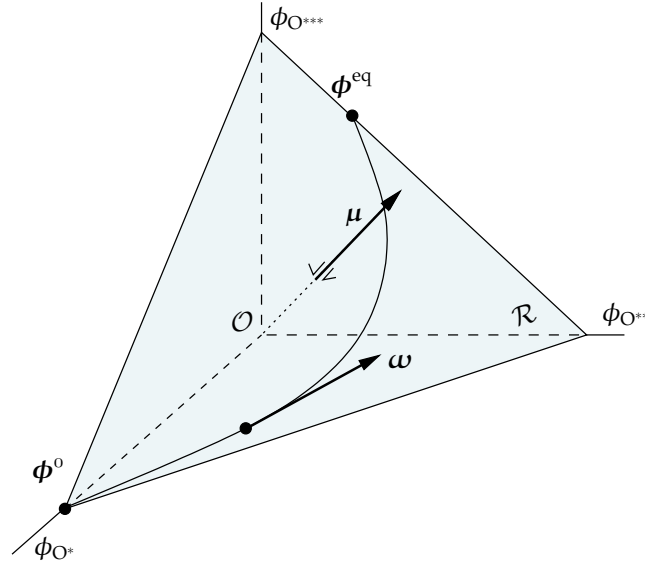
Figure 3.1 :   A schematic representation of a 3-dimensional composition space.

3.1.1   Example

A simple but illustrative reactive system consists of one element O, three chemical components, O^*, O^{**}, and O^{***}, and three reactions

$$O^* \rightarrow O^{**} \qquad\qquad O^{**} \rightarrow O^{***} \qquad\qquad O^{***} \rightarrow O^{**}.$$
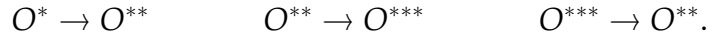
Figure 3.1 shows the three-dimensional composition space $\mathcal{C}$ of this system. The trajectory that starts from the initial point $\boldsymbol{\phi}^{\mathrm{o}}$ and ends in the equilibrium point $\boldsymbol{\phi}^{\mathrm{eq}}$ represents a solution of (3.2)-(3.4) for this system for $0 \leq t \leq \infty$. The element vector $\boldsymbol{\mu}$ of the element O, which is the only element present in the mixture, is given by

$$\boldsymbol{\mu} = (\mu_{O^*}, \mu_{O^{**}}, \mu_{O^{***}})^{\mathrm{T}} = (1, 1, 1)^{\mathrm{T}}. \tag{3.9}$$

The vector $\boldsymbol{\mu}$ is directed normal to the plane given by the parameterisation

$$\mu_{O^*}\phi_{O^*} + \mu_{O^{**}}\phi_{O^{**}} + \mu_{O^{***}}\phi_{O^{***}} = constant, \tag{3.10}$$

which means that the mass of element O is conserved in the plane described by (3.10). The chemical elements are conserved during chemical reactions, which implies that the vector $\boldsymbol{\omega}$ lies in the plane described by (3.10), or

$$\boldsymbol{\omega} \cdot \boldsymbol{\mu} = 0. \tag{3.11}$$

Furthermore, the vector representing the source terms is the local tangential vector to the solution of (3.2)-(3.4), i.e. the trajectory between $\boldsymbol{\phi}^{\mathrm{o}}$ and $\boldsymbol{\phi}^{\mathrm{eq}}$. In this example, the reaction space $\mathcal{R}$ is a $(N_{\mathrm{s}} - N_{\mathrm{e}})$-dimensional space described by (3.10).

3.1.2   Attracting manifolds in the composition space

As stated in the introduction of this chapter, combustion processes are characterised by a wide range of time scales. In chemical reduction techniques, it is assumed that the chemistry of a flame can be described by small number of slow processes, while assuming the fast processes in steady-state. The idea behind this assumption is illustrated by figure 3.2, which presents a projection of a N_s-dimensional composition space on a three-dimensional subspace of the composition space. The figure shows several flame trajectories in the composition space starting from the initial compositions $\boldsymbol{\phi}_i^0$, which are typical for a flame. These initial compositions all have the same enthalpy h and element fractions χ_j. Therefore, the initial points lie in the same reaction space $\mathcal{R}$ and all trajectories eventually end up in the same point in the composition space, i.e. the chemical equilibrium composition denoted by $\boldsymbol{\phi}^{eq}$. The equilibrium point can be seen as a zero-dimensional manifold, where all flame trajectories are attracted to. Close to the chemical equilibrium point, the trajectories collapse on a single line, or a one-dimensional manifold. On this line, the chemical processes are dominated by a single slow process. All other processes are much faster and can be assumed in steady-state. In general, the dimension of the manifold to which the flame trajectories collapse increases while going further away from $\boldsymbol{\phi}^{eq}$ (as shown by figure 3.2). Note that the steady-state assumption for a fast process is only valid if this process is much faster than all other processes in the flame.

In a chemical reduction method, it is assumed that the chemistry can effectively be described by a low number of slow processes, by applying steady-state assumptions to the fast processes. This means that the chemical compositions are restricted to a low-dimensional manifold, schematically shown in figure 3.2. Furthermore, it implies that the stiffness, which is caused by the large variation in time scales, and the dimension of the system, i.e. the number of differential equations that needs to be solved, can be reduced as well. A mathematical background for the reduction of a system of ODEs (ODE: Ordinary Differential Equation), which is based on singular perturbation theory, can be found in e.g. [92] and [34]. Several approaches to reduce reaction mechanisms have been introduced in the past. A concise overview of a number of these methods is given in section 3.2.

3.1.3   Time scales in flames

The analysis presented so far was based on the chemistry as it is found in a homogeneous system (3.2)-(3.4). In this system, the enthalpy h and element numbers χ_j are conserved variables. Hence, the chemical compositions are restricted to the $(N_s - N_e)$-dimensional reaction space $\mathcal{R}$. In real flames, this is generally not the case. Due to preferential diffusion, mixing processes, heat loss and pressure variations (e.g. in detonations), the chemical composition is not restricted to the reaction space $\mathcal{R}$. As stated in section 3.1.2, chemical reduction methods are based on steady-state
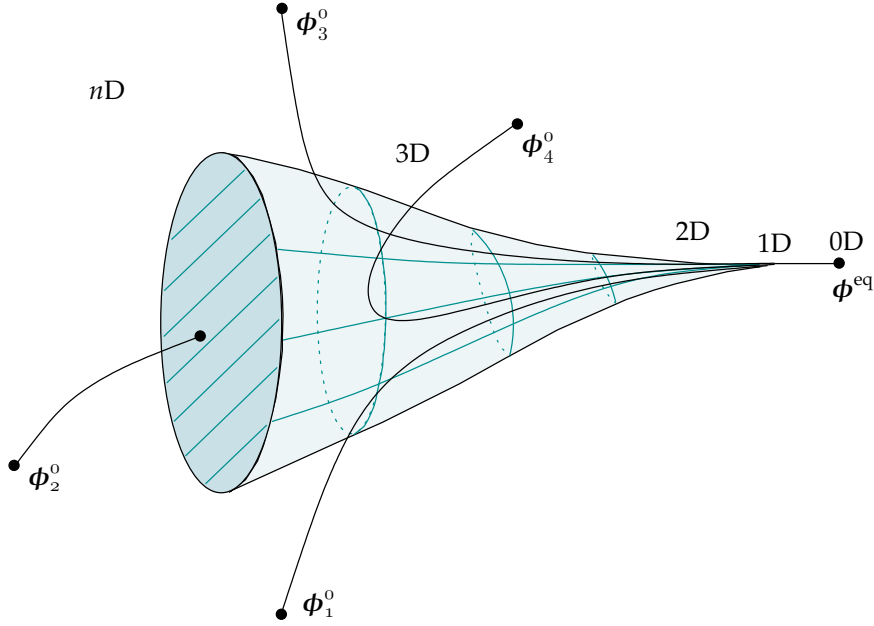
Figure 3.2 : A schematic example of an attracting manifold in the composition space. The points $\boldsymbol{\phi}_i^o$ denote several initial compositions, whereas the chemical equilibrium is denoted by $\boldsymbol{\phi}^{\text{eq}}$.

assumptions for the fast chemical processes. To be able to decouple the fast processes from the slow processes, all time scales in the flame must be evaluated. This means that also the time scales which involve mixing, heat loss and pressure variations must be investigated. In addition, as general combustion is not homogeneous, diffusion time scales must be taken into account as well.

A time scale for the chemistry can be obtained from the chemical source term of the reaction progress variable $\mathcal{Y}$, which was introduced in chapter 1 (see figure 1.2a). Here, it is assumed that the reaction progress variable is defined as a species mass fraction, or a linear combination of species mass fractions. The chemical source term $s_{\mathcal{Y}}$ represents the nett effect of two contributions, i.e. the production and the consumption of $\mathcal{Y}$. To give a fair analysis of the chemical time scales, the production and consumption terms should be treated separately. For this purpose, the source term of $\mathcal{Y}$ is written as

$$s_{\mathcal{Y}} = s_{\mathcal{Y}}^+ + s_{\mathcal{Y}}^-, \tag{3.12}$$

where the superscripts '+' and '-' stand for the production rate and the consumption rate of the progress variable $\mathcal{Y}$, respectively. The overall time scale of the chemical source term $s_{\mathcal{Y}}$ is given by

$$\tau_{\text{c}} = \frac{\rho}{|s_{\mathcal{Y}}|}. \tag{3.13}$$

From equation (3.12), it can be concluded that the chemical time scales corresponding to the production and the consumption of $\mathcal{Y}$ are given by

$$\tau_{\text{c}}^+ = \frac{\rho}{|s_{\mathcal{Y}}^+|} \qquad \text{and} \qquad \tau_{\text{c}}^- = \frac{\rho}{|s_{\mathcal{Y}}^-|}. \tag{3.14}$$

It should be noted that these chemical time scales represent global chemistry. Other chemical time scales can be much faster. The time scales presented here can be used to compare the time scale of chemical processes in general with other time scales in the flame, which will be introduced below.

An expression for the mixture fraction is given by [4],

$$Z = \frac{Z^* - Z^*_{\text{ox}}}{Z^*_{\text{fu}} - Z^*_{\text{ox}}}, \tag{3.15}$$

where Z^* is given by

$$Z^* = 2\chi_{\text{C}} + \frac{1}{2}\chi_{\text{H}} - \chi_{\text{O}}, \tag{3.16}$$

and the subscripts 'fu' and 'ox' stand for pure fuel and pure oxidiser, respectively. In a premixed flame, the mixture fraction is a conserved variable and it can only change locally due to preferential diffusion. In non-premixed and partially-premixed flames, the mixture varies between a fuel rich value Z_1 and a lean value Z_2. In case of a fully non-premixed flame, these values are $Z_1 = 1$ and $Z_2 = 0$, respectively. As in a non-premixed flame, the mixing of fuel and oxidiser is mainly driven by diffusive processes, a time scale for the mixing of fuel and oxidiser can be defined as

$$\tau_{Z_{\text{st}}} = \frac{\delta_{\text{m}}^2}{D_Z}, \tag{3.17}$$

with D_Z the diffusion coefficient of Z, Z_{st} the stoichiometric value of the mixture fraction, and δ_{m} the mixing length, which is defined as

$$\delta_{\text{m}} = (Z_1 - Z_2) \left(\|\boldsymbol{\nabla} Z\|_{Z=Z\text{st}} \right)^{-1}. \tag{3.18}$$

Note that $\tau_{Z_{\text{st}}}$ is related to the scalar dissipation rate χ, which is usually defined as $\chi = 2D_Z \|\boldsymbol{\nabla} Z\|^2$, according to

$$\chi_{\text{st}} = 2D_Z \|\boldsymbol{\nabla} Z\|^2_{Z=Z_{\text{st}}} = 2(Z_1 - Z_2)^2 \tau_{Z_{\text{st}}}^{-1}. \tag{3.19}$$

Note that the scalar dissipation rate is a local value, whereas $\tau_{Z_{\text{st}}}$ is defined at stoichiometry. Analogous to the scalar dissipation rate, a local mixing time scale can be defined as

$$\tau_Z^{-1} = \frac{\chi}{2(Z_1 - Z_2)^2}. \tag{3.20}$$

In premixed flames, the mixing time τ_Z is infinite. Therefore, the effect of a gradient in Z on the chemistry does not need to be taken into account in a reduction method, which is used to model premixed flames. However, in non-premixed flames, the gradient of Z is non-zero and the mixing time scale τ_Z may be of the same order as other time scales. In that case, it may be necessary to take the effect of the Z-gradient on the chemistry into account in the reduction method. A similar relation can be derived for the time scale of the heat flux, for instance near a wall, i.e.

$$\tau_h = \frac{c_p \delta_h^2}{\lambda'}, \tag{3.21}$$

where δ_h is defined as

$$\delta_h = (h_1 - h_2) \left(\|\boldsymbol{\nabla} h\|_{h=h_{\text{wall}}} \right)^{-1} , \tag{3.22}$$

with h_1 and h_2 are enthalpy values in the flow and close to the wall, respectively.

Pressure variations typically travel with the speed of sound. Since, in general combustion situations, the velocities involved with combustion are much smaller than the speed of sound (i.e. the Mach number $Ma \ll 1$), the pressure is often assumed to be locally constant. Therefore, the effect of pressure variations on the chemical behaviour does not have to be taken into account in the reduction method. However, in detonations, the typical flame velocities are in the same order of the local speed of sound and the pressure may not assumed to be locally constant, so the effect of pressure variations on the chemistry needs to be taken into account in the reduction method. As the flames studied in this thesis are deflagarations, the pressure gradients are not taken into account in the reduction methods in the remainder of this thesis.

Finally, also diffusion effects may lead to deviations from a homogeneous system, which means that also diffusion time scales need to be taken into account. A distinction is made between mixing of fuel and air (described by the mixture fraction Z) and diffusion of individual species, since in a purely premixed system, where Z is constant, diffusion of individual chemical components still plays an important role in the combustion process. A typical diffusion time scale of the reaction progress variable $\mathcal{Y}$ can be expressed as

$$\tau_{\text{D}_y}^{-1} = |R_{\text{D}_y}| = \frac{1}{\rho \mathcal{Y}} \left| \boldsymbol{\nabla} \cdot \left(\frac{\lambda'}{c_p Le_y} \boldsymbol{\nabla} \mathcal{Y} \right) \right|, \qquad i \in [1, N_s], \tag{3.23}$$

with R_{D_y} the diffusion rate of $\mathcal{Y}$ in the conservation equation for species (2.46). In the hot regions of a flame, diffusion is generally much slower than chemistry, so the effect of diffusion on the chemical behaviour can be ignored. However, in colder parts diffusion time scales and chemical time scales can be of the same order.

Finally, also a convection time scale can be defined according to

$$\tau_{\text{C}_y}^{-1} = |R_{\text{C}_y}| = \frac{1}{\rho \mathcal{Y}} |\boldsymbol{\nabla} \cdot (\rho \boldsymbol{u} \mathcal{Y})|, \tag{3.24}$$

with R_{C_y} the convection rate of $\mathcal{Y}$.

3.1.4   Time scales in a non-premixed flame

This section presents the time scales, which are introduced in the previous section, in a typical non-premixed flame configuration, i.e. a methane/air counterflow diffusion flame (see figure 1.4). The flame is modelled with the GRI-mech 3.0 reaction mechanism [85], at atmospheric conditions. The applied strain rate is $a = 200$ s^{-1} and the inlet temperatures are 300 K. Previous work, in which the chemical time scales of different species are compared in this way was presented in [11]. Figure

3.3a shows profiles of the temperature, the mixture fraction, and the mass fractions of methane, oxygen, and the progress variable $\mathcal{Y}$, as a function of the spatial coordinate s. A progress variable is introduced to parameterise the reaction progress. The chemical time scale that is presented here is derived from the source term of the progress variable, which is defined as

$$\mathcal{Y} = Y_{H_2} + Y_{H_2O} + Y_{CO_2}. \tag{3.25}$$

Generally, the chemistry is relatively fast in regions where the temperature is high. In colder regions, the chemical time scales can be of the same order as other time scales in the flame. In figure 3.3b, the different time scales are presented as a function of temperature. The figure shows the inverse of the time scales τ_c, τ_c^+, and τ_c^- and the rates R_{D_y} and R_{C_y}. In figure 3.4, the chemical time scales are compared with the mixing rate R_Z for two different values of the strain rate. Figure 3.4a shows the time scales for a counterflow diffusion flame with a strain rate of $a = 200$ s^{-1}, whereas figure 3.4b shows results for $a = 400$ s^{-1}. From the figures 3.3 and 3.4, it can be concluded that chemistry is significant in a small region of the flame, i.e. the reaction layer. Furthermore, in regions of high temperature, the behaviour of the flame is mainly determined by chemical production and consumption. In addition, it can be concluded that the mixing time scale τ_Z, is much larger than the chemical time scale τ_c. For higher values of the applied strain rate, τ_Z decreases and τ_c^+ and τ_c^- increase, hence the effect of mixing on the chemical behaviour increases.

3.1.5 Time scales in a premixed flame

Figure 3.5a shows profiles for a stoichiometric methane/air flame at atmospheric conditions, as a function of the coordinate perpendicular to the premixed flame front. The flame is simulated with the GRI-mech 3.0 reaction mechanism. The initial temperature is 300 K and the pressure is 1 atm. The typical time scales in this flame are presented in figure 3.5b. Similar to the non-premixed flame, the figure shows that at high temperatures, the flame behaviour is mainly dominated by chemical production and consumption processes. However, at lower temperatures, the chemical and transport time scales are of the same order. In this region, the flame behaviour is determined by a balance between chemical and transport processes, which is typical for a premixed flame.

3.2 Reduction Methods

In this section, an overview of approaches to reduce the chemistry is given. It should be noted that an accurate description of the chemistry is especially needed in regions of the flame, where chemistry is important, which means in the reaction layer (see figures 1.2b and 1.3b). As stated in the introduction of this chapter, the processes

(a)   (b)

Figure 3.3 :   Several profiles and time scales of a typical a one-dimensional non-premixed
flame at a strain rate of $a = 200\ \mathrm{s}^{-1}$. Left figure: the temperature T (solid
line), the mixture fraction Z (dash-dotted line), the progress variable $\mathcal{Y}$ (dashed
line), the mass fraction of methane Y_{CH_4} (closed symbols) and the mass fraction
of oxygen Y_{O_2} (open symbols). Right figure: τ_c^+ (solid line), τ_c^- (long-dashed
line), τ_c (dash-dotted line), R_{D_y} (short-dashed line) and R_{C_y} (dotted line) as a
function of the temperature. Note that the temperature axis is mirrored with
respect to the maximum value, which is approximately 2000 K. Temperatures
on the left hand side correspond to the fuel side, whereas temperatures on the
right hand side correspond to the oxidiser side.

that take place in a flame are characterised by a wide range of time scales. In the
derivation of most chemical reduction techniques, it is assumed that many chemi-
cal processes are much faster than transport processes. Based on this assumption,
steady-state assumptions are applied to the fast chemical processes.

A number of reduction methods has been introduced in the past few decades.
The major difference of the several reduction methods is the procedure, which is
used to decouple and identify the fast processes from the slow processes. Another
difference arises in the application of the reduced mechanism. In a number of meth-
ods, the size of the reaction mechanism is reduced in a pre-processing step. During
the application, the reduced mechanism is used in a similar fashion as the original
mechanism. These methods are referred to as global reduction methods. Other re-
duction methods generate a database in a pre-processing step, in which the local
chemical behaviour is stored. The reaction progress is parameterised by N_c^r control-
ling variables, which are typically (linear combinations of) species mass fractions.
If necessary, additional dimensions are added to the database, to be able to capture
for instance enthalpy variations due to heat-loss. The additional dimensions are

(a)   (b)

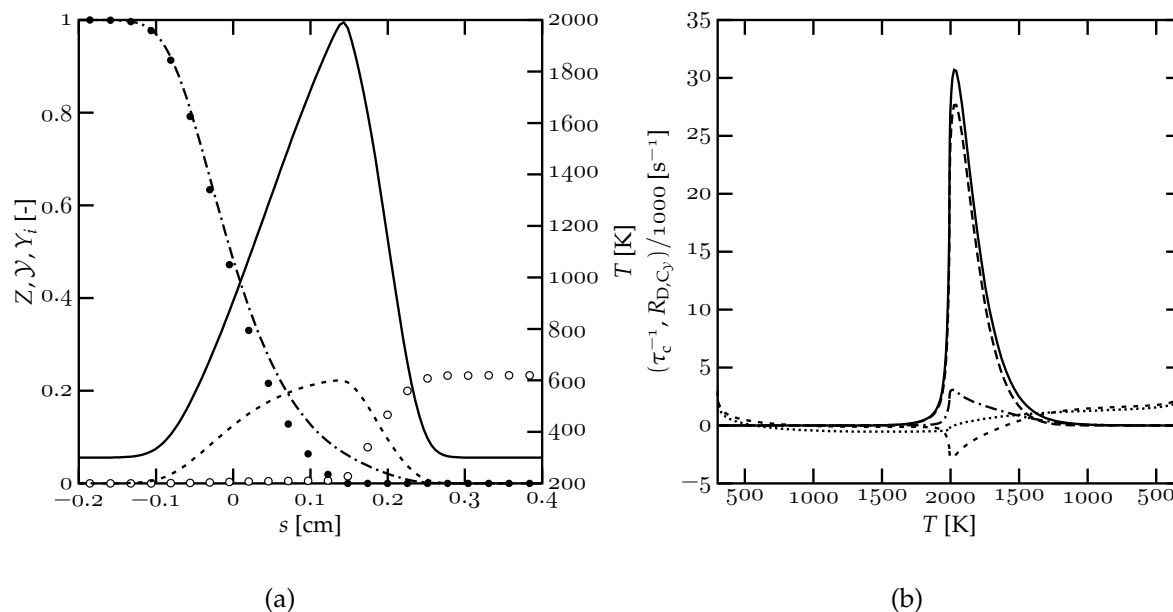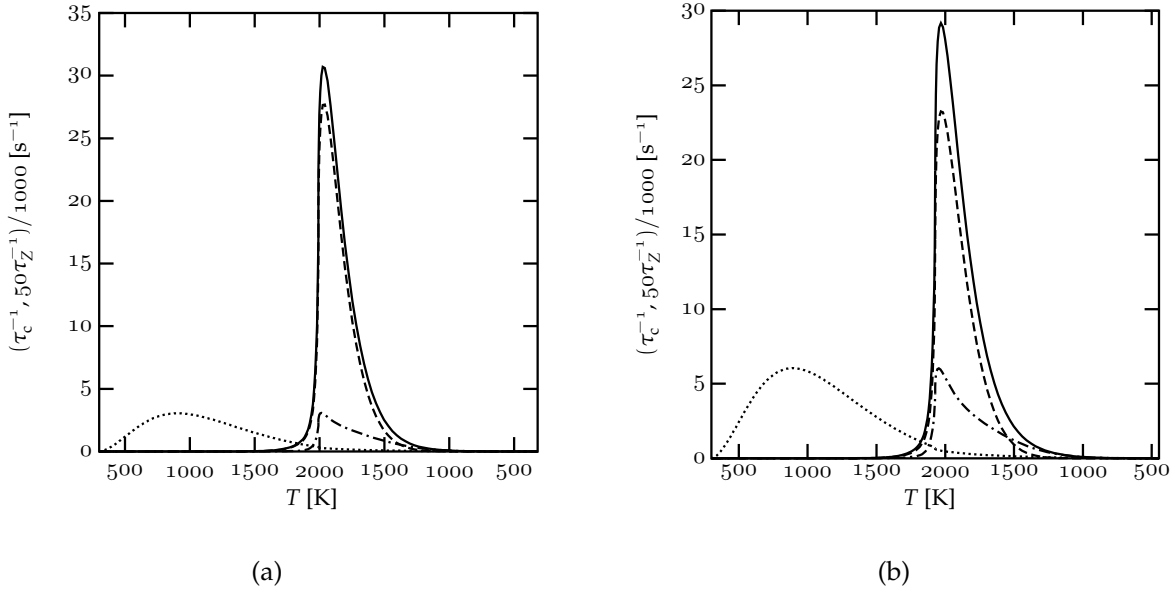**Figure 3.4** : Several time scales of a typical a one-dimensional non-premixed flame at a strain rate of $a = 200$ s^{-1} (left figure) and $a = 400$ s^{-1} (right figure). The inverse of the chemical time scales of the reaction progress variable $\mathcal{Y}$, τ_c^+ (solid line), τ_c^- (long-dashed line), τ_c (dash-dotted line), and the inverse of the mixing time scale τ_Z (dashed line) as a function of the temperature. Note that the temperature axis is mirrored with respect to the maximum value, which is approximately 2000 K. Temperatures on the left hand side correspond to the fuel side, whereas temperatures on the right hand side correspond to the oxidiser side. Note the scale change along the vertical axes of figure a and b.

parameterised with N_c^{nr} so-called non-reacting controlling variables. During the application of the reduction method, only equations for the $N_c = N_c^r + N_c^{nr}$ controlling variables are solved, in stead of solving the full set of equations. Other flame variables are retrieved from the database in a post-processing step. This section presents the basic principles of the most prominent reduction methods. However, the Intrinsic Low-Dimensional Manifold (ILDM) method by Maas and Pope [58] and the Flamelet-Generated Manifold (FGM) method by Van Oijen and De Goey [69] will be discussed in more detail in the subsequent sections, as these methods are used in the remainder of this thesis.

In the conventional reduction technique [75], steady-state assumptions are applied to intermediate species and partial equilibrium assumptions for fast reactions. A steady-state assumption for a chemical component i means that the production and the consumption of this component balance, or

$$\frac{\omega_i}{\rho} = \boldsymbol{v}_j \cdot \boldsymbol{F} = \sum_{k=1}^{N_r} \left(\nu_{ik''} - \nu_{ik'} \right) \left(r_{kf} - r_{kb} \right) = 0, \qquad j \in [1, N_{ss}], \qquad (3.26)$$

with N_{ss} the number of species that are assumed in steady-state. The vector $\boldsymbol{v}_j$ is for this method given by $v_{ij} = \delta_{ij}$, with δ_{ij} the Kronecker delta. In the homogeneous

(a)   (b)
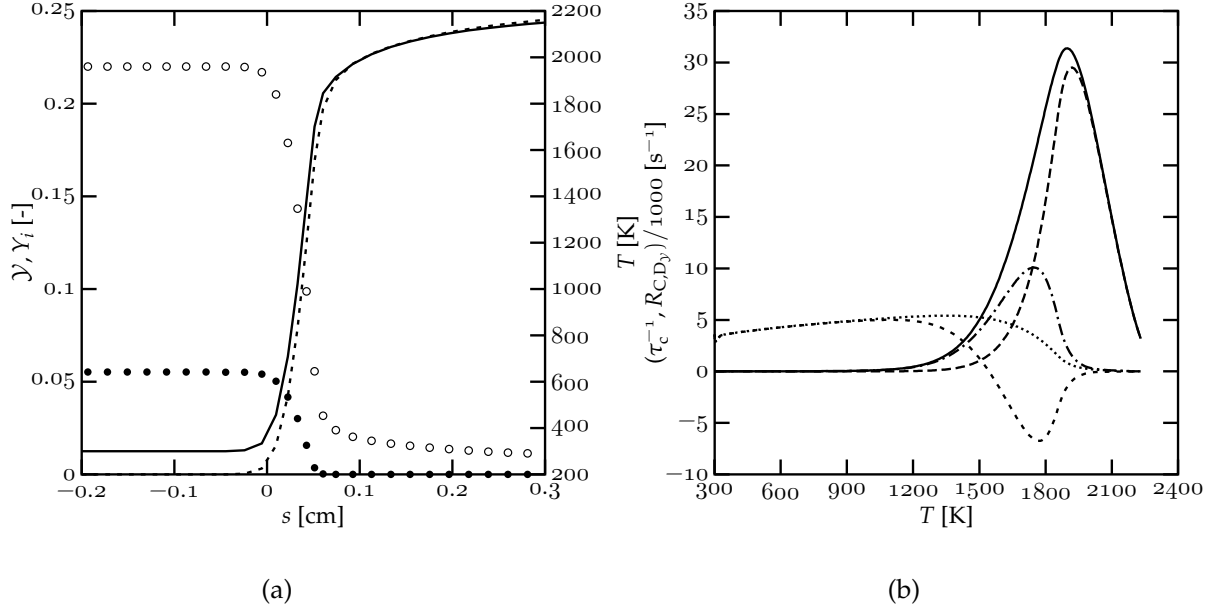
Figure 3.5 : The time scales in a stoichiometric premixed flame. Left figure: the temper-
ature T (solid line), the progress variable $\mathcal{Y}$ (dashed line), the mass fraction
of methane Y_{CH_4} (closed symbols) and the mass fraction of oxygen Y_{O_2} (open
symbols) as a function of the coordinate perpendicular to the flame front. Right
figure: τ_c^+ (solid line), τ_c^- (long-dashed line), τ_c (dash-dotted line), R_{D_y} (short-
dashed line) and R_{C_y} (dotted line) as a function of temperature.

system (3.2)-(3.4), a steady-state assumption for species i implies that the original
differential equation for species i is replaced by the algebraic equation (3.26). In a
flame, chemical reactions are balanced by convection and diffusion. Therefore, (3.26)
implies that the chemical processes related to the consumption and production of
species i are much faster than transport processes. The full set of species equations
(2.46) is replaced by

$$0 = s_i, \qquad i \in [1, N_{ss}], \qquad (3.27)$$

$$\frac{\partial \rho Y_i}{\partial t} + \boldsymbol{\nabla} \cdot (\rho \boldsymbol{u} Y_i) - \boldsymbol{\nabla} \cdot \left(\frac{\lambda}{c_p Le_i} \boldsymbol{\nabla} Y_i \right) = s_i, \qquad i \in [N_{ss}+1, N_s-1]. \quad (3.28)$$

The introduction of steady-state relations for the fast species not only reduces the
number of differential equations that needs to be solved, it also reduces the stiffness
of the set of differential equations. However, in stead of the full set of differential
equations, a large set of non-linear and strongly coupled algebraic equations needs
to be solved. The stiffness of these algebraic equations can be reduced by obtaining
explicit relations for the steady-state species. Explicit relations can be obtained by a
truncation of the summation in (3.26), in which only the largest terms in (3.26) are
considered.

The selection of steady-state species is done manually, which requires deep in-
sight in the chemical behaviour of the flame. For large reaction mechanisms, which

contain hundreds of species and reactions, this is a complicated task. In addition, the steady-state relations for the species are assumed to be valid in the complete domain, hence v_j is fixed, which is generally not the case. Consequently, the reduced reaction mechanism is inaccurate in parts of the domain, which may lead to an inaccurate description of the flame behaviour. A solution to this problem has been proposed by Løwås *et al.* [55]. In this method, a so-called level of importance (LOI) index is introduced, which indicates whether a species may be considered in steady-state. The LOI values correspond to the sensitivity of a chemical component on the accuracy of the result. If the LOI value of a certain species is below a certain threshold, it may be assumed in steady-state.

The CSP (Computational Singular Perturbation) algorithm, introduced by Lam and Goussis [54], uses a singular perturbation technique to distinguish between slow and fast processes. In contrast to the conventional reduction technique, the time-scale analysis is done locally and the number and the identity of processes which are assumed in steady-state are not constant. Even though this method is very accurate, its direct applicability as a reduction technique in complex simulations is questionable because of the high computational costs. On the other hand, the CSP method can be used to construct a globally reduced mechanism, by averaging the CSP results over the entire domain of a simple flame configuration [60]. In this manner, a reduced mechanism is obtained which can be used globally. However, the local accuracy of the original CSP method is lost.

The last reduction method, which is treated in this section, is the so-called Rate-Controlled Constraint Equilibrium (RCCE) method [50, 88], which is based purely on thermodynamics. A manifold is constructed, based on maximum entropy or minimum free energy conditions of the gas mixture, subject to specified constraints. The so-called constraint equilibrium manifolds (CEMs), which are obtained with the RCCE method, have a number of mathematical properties, which are generally not present in other reduction methods [88]. A manifold point is always uniquely defined. Furthermore, the manifold is infinitely differentiable, which stabilises the reduced computation.

Reduction techniques, in which a database is used to store the chemical behaviour, can be optimised further by using efficient storage techniques. The most important criteria for the efficiency of the retrieval of data from a database are the required memory needed for the storage of the database, the CPU time needed to retrieve a value from the database, and the accuracy of the retrieved value. Several methods to make the storage and retrieval more efficient have been introduced in literature. In [93], the database is replaced by a set of orthogonal polynomials. Another possibility is the use of so-called neural networks for the storage and application of the database [15]. In the so-called *in situ* Adaptive Tabulation (ISAT) [79], a database is created during run time. The ISAT method has two major advantages. Firstly, the size of the database is restricted to the actually accessed part of the composition space. In many reduction methods, the database is generated in

a pre-processing step. This means that it is not a priori known which part of the composition space is accessed during the application, so the size of the database can not be optimised. Secondly, the accuracy of the reduced mechanism is directly controlled by a so-called error control. Based on this error control, it is decided whether a newly obtained point in the composition space must be added to the database. In this manner, the size of the database can also be optimised for a designed accuracy.

3.3   Intrinsic-Low Dimensional Manifolds (ILDM)

Another very popular reduction method, the Intrinsic Low-Dimensional Manifold (ILDM) method [58, 59] will be treated in more detail, as its theory is used in the remainder of this thesis. Here, only the general principles are presented. For a more extensive study of the ILDM method, the reader is referred to, e.g. [6, 27, 58]. It is assumed that the chemical composition is restricted to a so-called intrinsic low-dimensional manifold (see figure 3.2) in the composition space. The purpose of the ILDM method is to find this low-dimensional manifold, parameterise it with so-called controlling variables, and store it in a database. The manifold is found by means of an eigenvalue analysis of the chemical source term. The ILDM method has been applied successfully in a number of applications, cf. [38, 67, 100]. An improved version of the ILDM method has recently been introduced by Nafe and Maas [65]. In this method, the original ILDM is used as an initial guess. During a post-processing step, a time dependent solver is used to remove the effect of mixing of slow and fast time-scales, which results in a more accurate database.

The method basically consists of three steps: the definition of the manifold, the procedure to obtain the manifold and the application of the manifold. In this section, the basics of the ILDM method are explained. First, it is described how the steady-state assumptions are made by means of a time scale analysis of the chemical source term. Secondly, the equations that define the manifold are derived. Subsequently, the computational strategy to compute the manifold is presented. Next, it is described how a manifold is used in a flame simulation. Finally, the theory of so-called slow manifolds is described generally.

3.3.1   Time scale analysis of the chemical source term

Since the ILDM method is a chemical reduction technique, only the chemical system is analysed, i.e. equation (3.5). This implies that it is assumed that the chemical processes are much faster than convective and diffusive processes in a flame. The homogeneous system considered here is a system in which the enthalpy h is constant. If, however, a reduced chemical model is developed for non-isobaric combustion processes, it can be convenient to start the analysis with a constant volume model, hence a model with a constant internal energy could be used then [26].

To perform a time scale analysis of the homogeneous system (3.5), the source term $F(\Psi)$ is linearised around a reference state Ψ^0,

$$F(\Psi) \approx F(\Psi^0) + J(\Psi^0)(\Psi - \Psi^0), \qquad (3.29)$$

where J is the Jacobi matrix, which is defined as $J_{ij} = \partial F_i / \partial \Psi_j$. After combining (3.5) and (3.29), the evolution of $\Psi(t)$ is described by

$$\frac{d\Psi}{dt} \approx F(\Psi^0) + J(\Psi^0)(\Psi - \Psi^0). \qquad (3.30)$$

By introducing $\epsilon(t)$ as the difference between the reference state $\Psi^0(t)$ and $\Psi(t)$, i.e.

$$\epsilon(t) = \Psi(t) - \Psi^0(t), \qquad (3.31)$$

the following expression is obtained

$$\frac{d\epsilon}{dt} = J(\Psi^0)\,\epsilon, \qquad (3.32)$$

with initial condition $\epsilon(0) = \Psi(0) - \Psi^0(0)$. If it is assumed that the Jacobi matrix can be diagonalised, the time scales of the system (3.32) can be separated by means of an eigenvalue analysis,

$$\frac{d\epsilon}{dt} = U\Lambda U^{-1}\epsilon, \qquad (3.33)$$

with Λ a diagonal matrix containing the eigenvalues λ_i^J, for $i \in [1, N_{st}]$ of the Jacobi matrix J. The columns of the matrix U are the right eigenvectors u_i^J, for $i \in [1, N_{st}]$. Note that the left eigenvectors v_i^J are given by the rows of U^{-1}. In general, the eigenvalues and eigenvectors may be complex. In [27], it can be found how a modified basis of eigenvectors, which consists of real valued vectors, can be constructed. Equation (3.33) can be rewritten in the basis of eigenvectors

$$\frac{d\widehat{\epsilon}}{dt} = \Lambda\widehat{\epsilon}, \qquad (3.34)$$

where the transformation $\epsilon = U\widehat{\epsilon}$ is used.

The evolution of $\widehat{\epsilon}_i(t)$ is schematically presented by figure 3.6. The figure shows the trajectories of $\widehat{\Psi}_i^0(t)$ and $\widehat{\Psi}_i(t)$. The general solution of (3.34) is given by

$$\widehat{\epsilon}_i(t) = \widehat{\epsilon}_i^0 \exp(\lambda_i t), \qquad i \in [1, N_{st}], \qquad (3.35)$$

with $\widehat{\epsilon}_i^0 = \widehat{\epsilon}_i(0)$. The behaviour of $\widehat{\epsilon}_i(t)$ is determined by the corresponding eigenvalue λ_i^J. In general, three groups of eigenvalues can be distinguished, depending on the value of the real part of the eigenvalue. If $\text{Re}(\lambda_i^J) > 0$, then $|\widehat{\epsilon}_i(t)|$ will grow, hence the eigenmodes corresponding with eigenvalues with a positive real part are called growing modes. Secondly, the real part of the eigenvalue can be equal to zero, i.e. $\text{Re}(\lambda_i^J) = 0$. It can be shown that eigenmodes with these eigenvalues correspond
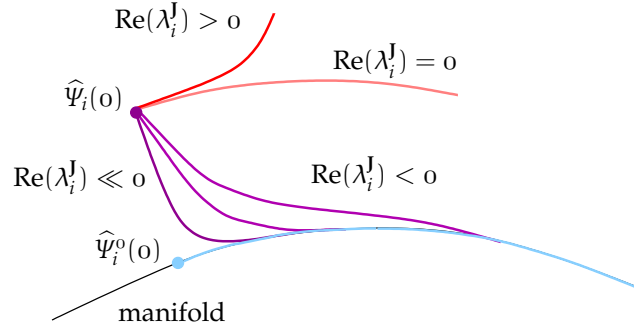
Figure 3.6 :   A schematic example of the evolution of the perturbation $\widehat{\epsilon}_i(t) = \widehat{\Psi}_i(t) - \widehat{\Psi}_i^{\mathrm{o}}(t)$ for different values of λ_i^{J}. Note that in this example a manifold only exists if $\lambda_i^{\mathrm{J}} < 0$.

to conserved variables, e.g. element numbers χ_j, $j \in [1, N_e]$ [27]. Finally, the real part of the eigenvalue can be negative, or $\mathrm{Re}(\lambda_i^{\mathrm{J}}) < 0$. Eigenmodes corresponding to these eigenvalues are called damping modes. In that case, the trajectory of $\widehat{\Psi}_i(t)$ is attracted to the trajectory of $\widehat{\Psi}_i^{\mathrm{o}}(t)$. The time scale involved with the attraction depends on $|\lambda_i^{\mathrm{J}}|$. If $|\lambda_i^{\mathrm{J}}|$ is small, then the attraction is slow. On the other hand, if $|\lambda_i^{\mathrm{J}}|$ is large, then $\widehat{\epsilon}_i(t)$ will rapidly decay.

To be able to assume a process $\widehat{\Psi}_i(t)$ in steady-state, two conditions must be satisfied. The first condition is obtained from the eigenvalues λ_i^{J}. The second condition can be derived from the differential equation for $\widehat{\Psi}_i(t)$, which is given by

$$\frac{\mathrm{d}\widehat{\Psi}_i}{\mathrm{d}t} = \widehat{F}_i^{\mathrm{o}} + \lambda_i^{\mathrm{J}} \left(\widehat{\Psi}_i - \widehat{\Psi}_i^{\mathrm{o}} \right), \qquad i \in [1, N_{\mathrm{st}}], \tag{3.36}$$

with $\widehat{F}_i^{\mathrm{o}} = \widehat{F}_i(\widehat{\boldsymbol{\Psi}}^{\mathrm{o}})$. The path length that is involved with the decay of $\widehat{\epsilon}_i(t)$ not only depends on $|\lambda_i^{\mathrm{J}}|$, it also depends on the time scale $\left(\widehat{F}_i^{\mathrm{o}} \right)^{-1}$. If $|\lambda_i^{\mathrm{J}}|$ is large compared to $\left(\widehat{F}_i^{\mathrm{o}} \right)^{-1}$, then the trajectory of $\widehat{\Psi}_i(t)$ will rapidly collapse on the trajectory of $\widehat{\Psi}_i^{\mathrm{o}}(t)$, i.e. close to the reference point $\widehat{\Psi}_i^{\mathrm{o}}(0)$. However, if $|\lambda_i^{\mathrm{J}}|$ is small compared to $\left(\widehat{F}_i^{\mathrm{o}} \right)^{-1}$, then the trajectory of $\widehat{\epsilon}_i(t)$ will be longer before $\widehat{\epsilon}_i(t) \approx 0$. In other words, there must be a clear separation between slow modes (evolution on the manifold) and fast modes (evolution towards the manifold). In the ILDM method, it is assumed that fast processes are in steady-state, so the chemical compositions are restricted to a low-dimensional manifold. From the analysis presented above, it can be concluded that a process may be assumed in steady-state if, both $\mathrm{Re}(\lambda_i^{\mathrm{J}}) \ll 0$ and $|\mathrm{Re}(\lambda_i^{\mathrm{J}})| \gg |\left(\widehat{F}_i^{\mathrm{o}} \right)^{-1}|$. The steady-state assumption for a process with a corresponding eigenvalue that satisfies these conditions, is given by

$$\frac{\mathrm{d}\widehat{\Psi}_i}{\mathrm{d}t} = 0, \qquad i \in [1, N_{\mathrm{ss}}]. \tag{3.37}$$

In figure 3.6, it is assumed that $\boldsymbol{\Psi}^{\mathrm{o}}(0)$ is on the manifold, so the trajectory of $\boldsymbol{\Psi}^{\mathrm{o}}(t)$ is a trajectory on the manifold. The eigenmode $\widehat{\Psi}_i(t)$, relaxes rapidly towards the

manifold only if the corresponding eigenvalue satisfies both steady-state conditions. On the other hand, if the steady-state conditions are not satisfied for a mode corresponding to $\widehat{\Psi}_i^{o}$, than this mode may not be assumed in steady-state. Hence, this mode also describes a motion over the manifold. The dimension of the manifold is determined by the number of eigenmodes, which can not be assumed in steady-state.

3.3.2 Equations that define the manifold

In this section, the equations that define the manifold are described. To find a manifold point Ψ, a set of N_{st} equations must be solved. Firstly, N_{ss} steady-state relations are defined, based on the size of the real part of the eigenvalues. Secondly, a number of equations is needed to parameterise the manifold in terms of the conserved variables. Finally, the system is closed with so-called parameterisation equations, which parameterise the reaction progress.

On the manifold, the eigenvalues λ^J can be separated into three groups. First a group of N_{ss} eigenvalues has a large negative real part. These eigenvalues correspond to processes which are assumed in steady-state. Using the transformation $\widehat{\Psi} = \mathbf{U}^{-1}\Psi$, the steady-state assumptions (3.37) can be rewritten as

$$\widehat{F}_i = v_i^J \cdot F = 0, \qquad i \in [1, N_{ss}], \tag{3.38}$$

with v_i^J the left eigenvectors of the Jacobi-matrix $\mathbf{J}$. Note the analogy between this expression for the steady-state processes and equation (3.26) in the conventional reduction method. Equation (3.38) implies that on the manifold, the chemical source term has no component in the direction corresponding to the fast damping modes.

The remaining eigenvalues can be divided into two groups. First, a group of $N_c^{nr} = N_e + 2$ eigenvalues is equal to zero, corresponding to conserved variables. In general, for the conserved variables, a set of parameterisation equations is solved. Suppose that the point Ψ_m is already on the manifold. This can be, for example, the chemical equilibrium point Ψ_e, which always lies on the low-dimensional manifold. As Ψ_m is on the manifold, the composition in this point satisfies the equations, which define the conserved variables, e.g. equation (3.8) for the element fractions χ_j. Therefore, this point can be used as a reference for the new point Ψ. The equations that fix the conserved variables can be written as

$$\mathbf{P}^{nr}(\Psi - \Psi_m) = 0, \tag{3.39}$$

where $\mathbf{P}^{nr}$ is a $(N_c^{nr} \times N_{st})$-dimensional matrix.

Finally, a group of $N_c^r = N_{st} - N_c^{nr} - N_{ss}$ eigenvalues corresponds to slow damping modes and growing modes. As these processes are not assumed in steady-state, they correspond to processes in the manifold. The parameterisation equations that are solved for these processes describe the reaction progress,

$$\mathbf{P}^r(\Psi - \Psi_m) = \beta, \tag{3.40}$$

where $\mathbf{P}^r$ is a $(N_c^r \times N_{st})$-matrix, and $\boldsymbol{\beta}$ is a vector which contains the step size.

The equations above are derived for a manifold with constant pressure, element fractions and enthalpy. However, in many combustion systems, at least some of these variables are not constant. To be able to capture variations in the enthalpy, pressure, and element fractions, these variables can be added as additional dimensions to the manifold. The controlling variables that parameterise the manifold in the direction of the conserved variables are referred to as non-reacting progress variables. In that case, the right hand side of (3.39) is replaced by the vector $\boldsymbol{\alpha}$, which contains the step sizes for variations in the conserved variables. The complete set of equations, which define a manifold point $\boldsymbol{\Psi}$, is given by

$$\mathbf{P}^{nr}\left(\boldsymbol{\Psi} - \boldsymbol{\Psi}_m\right) = \boldsymbol{\alpha} \tag{3.41}$$

$$\mathbf{P}^r\left(\boldsymbol{\Psi} - \boldsymbol{\Psi}_m\right) = \boldsymbol{\beta} \tag{3.42}$$

$$v_i^J \cdot \boldsymbol{F} = 0, \qquad i \in [1, N_{ss}]. \tag{3.43}$$

The set of equations (3.41-3.43) can be solved on a pre-defined fixed grid, for the reacting and non-reacting controlling variables (e.g. an equidistant grid). In this case, the number and the identity of the controlling variables are chosen in advance. Hence, both $\mathbf{P}^{nr}$ and $\mathbf{P}^r$ are pre-defined and kept constant during the construction of the manifold. However, if the parameterisation matrix $\mathbf{P}^r$ is allowed to change during the construction of the manifold, a continuation algorithm, which is multi-dimensional can be used [56, 84]. In this case, only the number of controlling variables and the identity of the non-reacting controlling variables is chosen in advance. The identity of the reacting controlling variables is chosen afterwards. A fixed parameterisation has a number of advantages [5]:

1. The ILDM database is well-structured and can be stored directly as a function of the controlling variables (a post-processing step is not needed).

2. The equations that parameterise the reaction progress, i.e. (3.40) are relatively simple and constant.

3. The implementation of the ILDM in a CFD code is straightforward.

On the other hand, a number of problems may occur:

1. Wrongly chosen controlling variables may lead to a bad parameterisation of the manifold and so-called turning points can not be identified.

2. The choice of parameterisation requires experience of the user.

3. The edges of the manifold can not be detected automatically.

These disadvantages can be overcome by using a multi-dimensional continuation method. The general concept of this method is discussed in the next section.
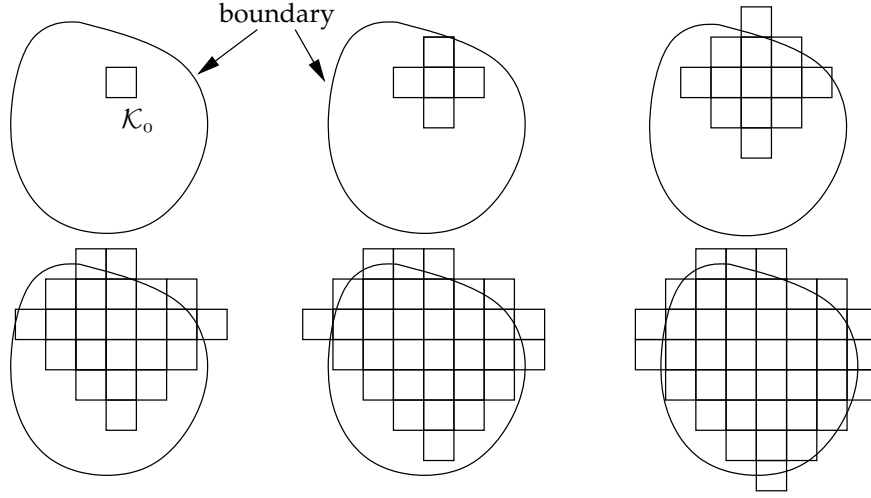
Figure 3.7 : A schematic example of the built up of a two-dimensional mesh [56]. First, the cell $\mathcal{K}_0$ is created. Subsequently, the neighbouring cells are created. Outside the domain where a solution can be found, no new cells are created.

3.3.3 Computational strategy

The major ingredients in the solution procedure are [56]:

- The generation of a mesh.
- The parameterisation of the manifold.
- A predictor-corrector algorithm for the computation of the manifold points.

Figure 3.7 schematically shows the built-up of a two-dimensional mesh. The mesh consists of N_c-dimensional cells, with $N_c = N_c^r + N_c^{nr}$. The computation is started in grid cell $\mathcal{K}_0$. First the vertices of this cell are computed. Successively, new grid cells are created at the boundaries of cell $\mathcal{K}_0$. In this manner, the number of grid cells is extended until the boundaries of the domain, in which a manifold can be defined, are reached. For more details about the mesh generation, for example the treatment of boundaries, the reader is referred to [56].

The set of equations (3.41)-(3.43) is solved with a multi-dimensional continuation algorithm. Therefore, the equations (3.41)-(3.43) are rewritten to yield a one-dimensional continuation process in the direction of $d = (\alpha, \beta)^{\mathrm{T}}$,

$$\mathbf{P}\left(\boldsymbol{\Psi} - \boldsymbol{\Psi}_{\mathrm{m}}\right) - \zeta d = 0, \tag{3.44}$$

$$v_i^{\mathrm{J}} \cdot \boldsymbol{F} = 0, \qquad i \in [1, N_{\mathrm{ss}}], \tag{3.45}$$

with ζ the local continuation parameter and $\mathbf{P}$ the local parameterisation matrix, which contains the matrices $\mathbf{P}^{\mathrm{nr}}$, and $\mathbf{P}^{\mathrm{r}}$. Even though the continuation algorithm is used to obtain multi-dimensional manifolds, it is one-dimensional in the sense that for each new manifold point, a step in only one direction is taken. Hence, in each step, only one element of the vector d is non-zero.
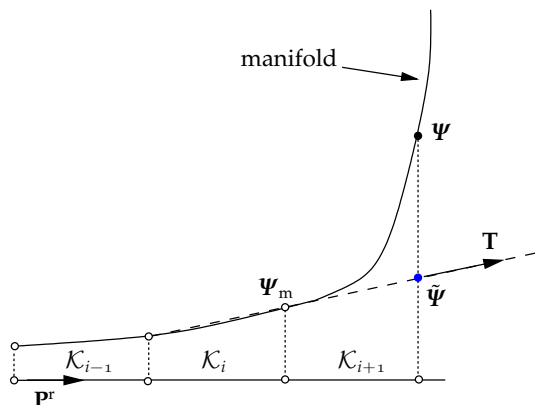
Figure 3.8 : A schematic one-dimensional example of a fixed parameterisation. The parameterisation matrix of the reaction progress $\mathbf{P}^r$ is kept fixed. The matrix $\mathbf{T}$ contains the tangential direction vectors, which are used to compute the initial guess $\tilde{\boldsymbol{\Psi}}$.

The projection matrix $\mathbf{P}$ can be predefined, if all progress variables are chosen in advance. If, furthermore, also the step sizes are predefined, the parameterisation method is similar to the method in which the grid is predefined. Note that in this case, the parameter ζ must be kept constant. Figure 3.8 schematically shows how the parameterisation matrix $\mathbf{P}^r$ is kept fixed during the creation of cell $\mathcal{K}_{i+1}$, in case of a one-dimensional manifold. The initial guess $\tilde{\boldsymbol{\Psi}}$ and the matrix $\tilde{\mathbf{T}}_{i+1}$ correspond to the predictor-corrector algorithm, which will be explained later.

On the other hand, the parameterisation of the reaction progress, i.e. $\mathbf{P}^r$, can be adapted locally to the manifold. Figure 3.9 shows how the parameterisation is updated after the creation of cell $\mathcal{K}_{i+1}$. First the parameterisation $\mathbf{P}_i^r$ of neighbouring cell $\mathcal{K}_i$ is copied to cell $\mathcal{K}_{i+1}$. The initial parameterisation of cell $\mathcal{K}_{i+1}$ is called $\tilde{\mathbf{P}}_{i+1}^r$ (see figure 3.9a). During the creation of the new cell, the parameterisation is kept constant. Once the new point $\boldsymbol{\Psi}$ is found, the parameterisation of the reaction progress for cell $\mathcal{K}_{i+1}$ can be updated to $\mathbf{P}_{i+1}^r$ (figure 3.9b). Note that only the reactive part of the parameterisation is updated. The adaptive parameterisation works similar in case of a multi-dimensional grid.

The algorithm to compute a manifold point generally consists of two steps. First an initial guess $\tilde{\boldsymbol{\Psi}}$ is created in a predictor step. Subsequently, the manifold point $\boldsymbol{\Psi}$ is obtained in a corrector step. As stated in equations (3.44)-(3.45), the solution procedure is started from a point $\boldsymbol{\psi}_m$, which is on the manifold. The initial guess $\tilde{\boldsymbol{\Psi}}$ is obtained from the predictor step, which is defined as

$$\tilde{\boldsymbol{\psi}} = \boldsymbol{\psi}_m + \zeta \tilde{\mathbf{T}}_{i+1} \left(\tilde{\mathbf{P}}_{i+1} \tilde{\mathbf{T}}_{i+1} \right)^{-1} \boldsymbol{d}, \tag{3.46}$$

where $\tilde{\mathbf{T}}_{i+1}$ is a matrix containing N_c vectors, which are tangential to the manifold at cell $\mathcal{K}_i$. Note that $\tilde{\mathbf{T}}_{i+1} = \tilde{\mathbf{P}}_{i+1} = \mathbf{P}_i$ in case of the adaptive parameterisation. Figures 3.8 and 3.9 schematically show how the initial guess is made in case of a one-
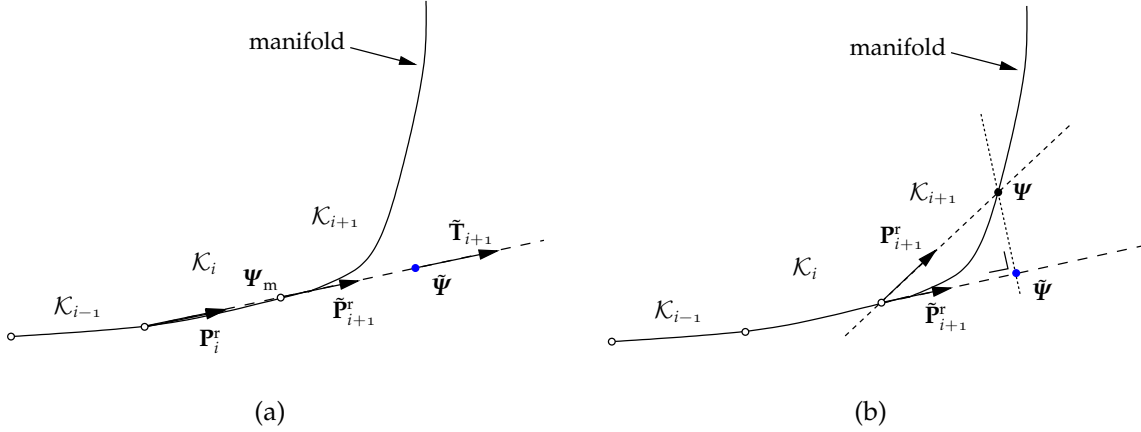
Figure 3.9 : A schematic one-dimensional example of an adaptive parameterisation. (a): First the parameterisation of cell $\mathcal{K}_i$ is copied to the new cell $\mathcal{K}_{i+1}$ and an initial guess is made in a predictor step. (b): Subsequently, the new manifold point is obtained in the corrector step and the parameterisation of cell $\mathcal{K}_{i+1}$ is updated.

dimensional manifold. The point $\tilde{\boldsymbol{\Psi}}$ will not be exactly on the manifold. Therefore, a correction must be applied. The corrector step is given by

$$\tilde{\mathbf{P}}_{i+1}\left(\boldsymbol{\Psi} - \boldsymbol{\Psi}_{\mathrm{m}}\right) - \zeta \boldsymbol{d} \;\; = \;\; 0, \tag{3.47}$$

$$\boldsymbol{v}_i^{\mathrm{J}} \cdot \boldsymbol{F} \;\; = \;\; 0, \qquad i \in [1, N_{\mathrm{ss}}]. \tag{3.48}$$

This set of equations can be solved using for example a damped Newton-solver or a pseudo-time stepping technique [89]. Once the new manifold point is obtained, the matrix $\tilde{\mathbf{T}}_{i+1}$ is updated to $\mathbf{T}_{i+1}$ and, in case of an adaptive parameterisation $\tilde{\mathbf{P}}^{\mathrm{r}}_{i+1}$ is updated to $\mathbf{P}^{\mathrm{r}}_{i+1}$.

The continuation parameter ζ is used to adjust the cell size of the manifold. The value of ζ is obtained from

$$\zeta = \frac{1}{\|\boldsymbol{d}\|} \sqrt{\left(\delta^2 - \|\boldsymbol{\Psi} - \tilde{\boldsymbol{\Psi}}\|^2\right)}, \tag{3.49}$$

with δ the (pre-set) arc-length between the new manifold point $\boldsymbol{\Psi}$ and the old manifold point $\boldsymbol{\Psi}_{\mathrm{m}}$.

3.3.4 The application of ILDM

Once the manifold is computed, it is stored as a function of the reacting controlling variables $\mathcal{Y} = (\mathcal{Y}_1, \ldots, \mathcal{Y}_{N_{\mathrm{c}}^{\mathrm{r}}})^{\mathrm{T}}$ and the non-reacting controlling variables $c = (c_1, \ldots, c_{N_{\mathrm{c}}^{\mathrm{nr}}})^{\mathrm{T}}$. If an adaptive parameterisation is used to obtain the manifold, the controlling variables that are used to parameterise the manifold are determined afterwards. The controlling variables are defined as,

$$\boldsymbol{\Psi}_{\mathrm{c}} = \mathbf{P}_{\mathrm{p}} \boldsymbol{\Psi} = \begin{pmatrix} \mathbf{P}_{\mathrm{p}}^{\mathrm{r}} \\ \mathbf{P}_{\mathrm{p}}^{\mathrm{nr}} \end{pmatrix} \boldsymbol{\Psi}, \tag{3.50}$$

with $\boldsymbol{\Psi}_c = (\boldsymbol{\mathcal{Y}}^T, \boldsymbol{c}^T)^T$ and $\mathbf{P}_p$, $\mathbf{P}_p^r$, and $\mathbf{P}_p^{nr}$ are matrices which parameterise the manifold globally. Note that $\mathbf{P}_p^r = \mathbf{P}^r$ and $\mathbf{P}_p^{nr} = \mathbf{P}^{nr}$ if the manifold is obtained with a fixed parameterisation. During the application, not all the data from the manifold is needed. In general, it is sufficient to store $\boldsymbol{F}_c = \mathbf{P}_p \boldsymbol{F}$, ρ, T and c_p in a small database, which is used during the CFD computation. In a post processing step, other variables like for instance the species mass fractions of other species, can be retrieved from another database, where the rest of the manifold data is stored. In the CFD computation, only conservation equations for the controlling variables are solved. These conservation equations are obtained by projecting the complete set of equations on the manifold, using the eigenvectors of the Jacobi matrix $\mathbf{J}$ [57]. The conservation equations for the state variables can generally be written as

$$\frac{\partial \boldsymbol{\Psi}}{\partial t} = \boldsymbol{F}(\boldsymbol{\Psi}) + \boldsymbol{\Sigma}(\boldsymbol{\Psi}), \tag{3.51}$$

where the term $\boldsymbol{\Sigma}(\boldsymbol{\Psi})$ represents the perturbations due to physical processes. Using the eigenvectors corresponding to the fast processes, the set of equations (3.51) is projected on the manifold according to

$$\frac{\partial \boldsymbol{\Psi}_c}{\partial t} = \boldsymbol{F}_c(\boldsymbol{\Psi}_c) + \mathbf{P}_p \left(\mathbf{I} - \mathbf{U}_f \mathbf{V}_f \right) \boldsymbol{\Sigma}(\boldsymbol{\Psi}), \tag{3.52}$$

where $\mathbf{I}$ is the $(N_{st} \times N_{st})$-identity matrix, $\mathbf{U}_f$ is a $(N_{st} \times N_{ss})$ matrix, which contains the right eigenvectors corresponding to the steady-state processes, and $\mathbf{V}_f$ is a $(N_{ss} \times N_{st})$ matrix that contains the corresponding left eigenvectors. With this projection method, the eigenvectors are needed during the CFD computation, which requires in a large database. On the other hand, also a simpler projection method has been proposed, using tangential direction vectors [28, 38]. This projection is formally not correct, but the errors caused by this projection method are relatively small compared to the errors induced by the reduced mechanism.

3.3.5 Slow Manifolds

A major assumption in the ILDM method, is that the fast chemical time scales are well separated from the slow chemical time scales. In practice, this is not necessarily the case. In figure 3.10, a one-dimensional hydrogen/air flame is compared with a homogeneous solution (3.2)-(3.4) and a one-dimensional ILDM approximation of the homogeneous solution. The initial mixture is a stoichiometric hydrogen/air mixture at a temperature of 300 K and a pressure of 1 atm. The figure shows that close to chemical equilibrium, the three solutions are equal. This implies that, a) chemistry is faster than diffusion time-scales, and b) that the chemistry can accurately be described with a one-dimensional manifold.

Further towards the unburnt side ($0.13 < Y_{H_2O} < 0.20$), the ILDM deviates from both the homogeneous solution and the flame solution. From this observation, it can be concluded that diffusion time scales can not be neglected (difference between the
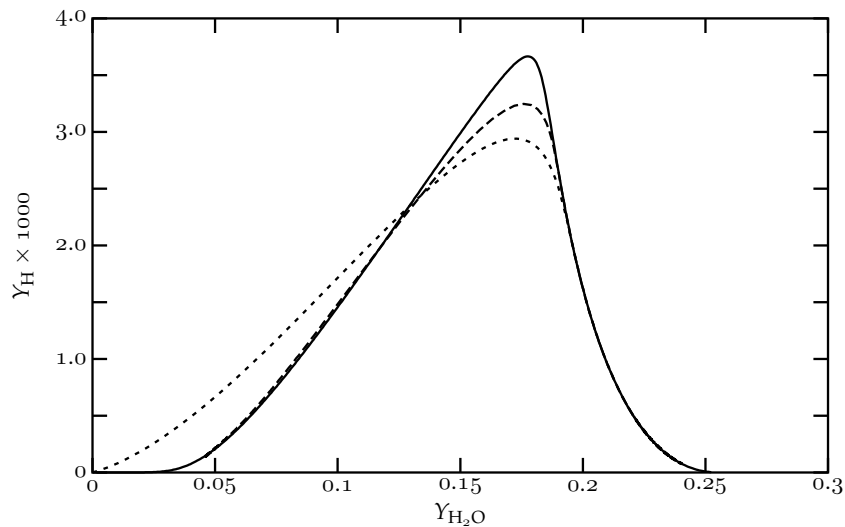
Figure 3.10 : A one-dimensional ILDM (solid line) of a stoichiometric H_2/air mixture at atmospheric conditions, with an initial temperature of 300 K, compared with a homogeneous solution (long dashed line) and a one-dimensional flame (short dashed line). Note that the flame is modelled with all Lewis numbers equal to unity.

homogeneous solution and the flame solution) and that a one-dimensional manifold is not sufficient to describe the chemistry (difference between the ILDM and the homogeneous solution). The over prediction of the hydrogen peak, with respect to the homogeneous solution, is caused by the mixing of chemical time-scales. In this region, the slowest and the second slowest eigenvalue are not well separated. However, the second slowest eigenvalue corresponds to a process which is also assumed in steady-state. Hence, the manifold is inaccurate in this region. Furthermore, the manifold is not inert, which means that if a manifold point would be used as an initial point in the homogeneous problem (3.2)-(3.4), the solution trajectory will deviate from the manifold.

Recently, a solution to this problem has been introduced by Nafe and Maas [65]. In this method, which is referred to as the method of Slow Manifolds, the original ILDM is used as an initial guess. In a post-processing step, a time-stepper is used to find the steady-state solution of the manifold. To prevent that all initial manifold points end up in the chemical equilibrium point, only movements perpendicular to the manifold are allowed. The resulting slow manifold is inert and, in addition, more accurate than the original ILDM.

Returning to figure 3.10, further upstream, ($Y_{H_2O} < 0.13$) the chemical time scales seem to be well separated again, as the ILDM is nearly equal to homogeneous solution. However, the temperature in this region is relatively low, and diffusion and chemical time scales are of the same order. Therefore, the homogeneous solution and the ILDM deviate from the flame solution, as diffusion processes are not included in the first two. A method to capture diffusion processes in the manifold

is discussed in the next section, which discusses the so-called Flamelet-Generated Manifold method.

3.4 Flamelet-Generated Manifolds for premixed flames

All the reduction methods presented so far are based on the chemical system only. In flames, and especially in premixed flames, the behaviour of the system is determined by a balance between convection, diffusion, and chemical reactions, as shown in figure 3.3 and 3.5. As the transport processes are ignored during the construction of the reduced mechanisms, it may lead to inaccuracies in colder parts of the flame, where the time scales of diffusion and chemistry are of the same order. A solution to this problem is offered by the Flamelet-Generated Manifold (FGM) method, which was introduced by Van Oijen [69]. Based on the observation that the internal structure of a propagating three-dimensional flame is very similar to the internal structure of a one-dimensional flame, it is assumed that also the chemistry in the three-dimensional flame is very close to the chemistry of a one-dimensional flame. This implies that one can use the solution of one-dimensional premixed flames to construct a chemical database, which can be used in two and three-dimensional flame simulations. This idea was first proposed by Bradley *et al.* [9] for turbulent flames. Van Oijen managed to improve the accuracy of the method by increasing the dimension of the database. In this case, the number of slow time-scales that are included in the manifold is increased. He also proposed methods to include enthalpy and mixture fraction variations in the manifold. A similar approach called Flame Prolongation of ILDM (FPI) has been introduced by Gicquel *et al.* [37]. In this section, the laminar flamelet equations, which are used to construct the FGM database are presented. Furthermore, the construction and the application of an FGM is discussed.

3.4.1 The flamelet description of laminar flames

The derivation of the equations, which define a FGM is analogous to the derivation of a flamelet description of a laminar premixed flame, following the ideas of De Goey and Ten Thije Boonkkamp [39, 40]. The reader is referred to their work for detailed information on the derivation of the flamelet analysis. In the following, only the major steps are presented. The flamelet description generally consists of two parts: a set of quasi one-dimensional equations, which describes the internal structure of the flame in a flame adapted coordinate system, and a kinematic equation, which couples the set of one-dimensional equations to the flow equations in the original coordinate system.

As stated in chapter 1, a premixed flame is defined as a region in space, where a typical flame variable $\mathcal{Y}$ varies between its unburnt value $\mathcal{Y}_u$ and its burnt value $\mathcal{Y}_b$. This so-called progress variable can be the density, the temperature or any linear
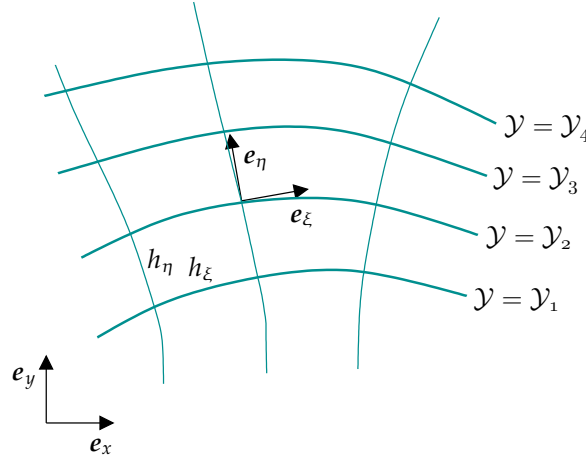
Figure 3.11 : A two-dimensional example of a flamelet coordinate system η adapted to the iso-contours of $\mathcal{Y}$.

combination of chemical components, which satisfies the condition $\nabla \mathcal{Y} \neq 0$. A flame surface is defined as an iso-contour of $\mathcal{Y}$, which means that $\mathcal{Y}$ is constant on such a surface. The motion of an iso-contour is given by the kinematic equation

$$\frac{\partial \mathcal{Y}}{\partial t} + \boldsymbol{u}_{\text{f}} \cdot \boldsymbol{\nabla} \mathcal{Y} = 0, \tag{3.53}$$

where $\boldsymbol{u}_{\text{f}}$ is the propagation velocity of the iso-surface, or the flame velocity.

With the introduction of the iso-contours, the conservation equations for mass (2.1), species mass fractions (2.4) and enthalpy (2.5) can be rewritten in a so-called flame adapted coordinate system. Figure 3.11 shows a schematic example of a flame in the original coordinate system $\boldsymbol{x} = (x, y)$, which is two-dimensional. A two-dimensional example is chosen for convenience. The extension to the three-dimensional case is analogous [39]. In this example, the flame adapted orthogonal coordinate system $\boldsymbol{\eta} = (\eta, \xi)$ is introduced. The unit vectors corresponding to the new coordinate system are $\boldsymbol{e}_\eta = (1/h_\eta)\partial \boldsymbol{x}/\partial \eta$ and $\boldsymbol{e}_\xi = (1/h_\xi)\partial \boldsymbol{x}/\partial \xi$, respectively. In the definition of the unit vectors, the scale vectors h_η and h_ξ are defined as $h_\eta = \|\partial \boldsymbol{x}/\partial \eta\|$ and $h_\xi = \|\partial \boldsymbol{x}/\partial \xi\|$, respectively. Furthermore, η is the coordinate locally perpendicular to the iso-contours, i.e. $\boldsymbol{e}_\eta = \text{sign}(\mathcal{Y}_{\text{b}} - \mathcal{Y}_{\text{u}}) \, \boldsymbol{\nabla} \mathcal{Y}/\|\boldsymbol{\nabla} \mathcal{Y}\|$, and ξ is the coordinate locally tangential to the iso-surfaces.

The flame velocity $\boldsymbol{u}_{\text{f}}$ is given by the sum of the gas velocity $\boldsymbol{u}$ and the laminar burning velocity s_{L}, which is directed normal to the iso-surfaces,

$$\boldsymbol{u}_{\text{f}} = \boldsymbol{u} - s_{\text{L}}\boldsymbol{e}_\eta. \tag{3.54}$$

Notice that the burning velocity is directed towards the unburnt mixture, which results in the minus sign in (3.54). The combination of (3.53) and (3.54) leads to the kinematic equation

$$\frac{\partial \mathcal{Y}}{\partial t} + \boldsymbol{u} \cdot \boldsymbol{\nabla} \mathcal{Y} = s_{\text{L}}\boldsymbol{e}_\eta \cdot \boldsymbol{\nabla} \mathcal{Y} = s_{\text{L}}\|\boldsymbol{\nabla} \mathcal{Y}\|. \tag{3.55}$$

Equation (3.55) is related to the well-known $\mathcal{G}$-equation [99]. However, in the $\mathcal{G}$-equation approach only the single iso-contour $\mathcal{G} = \mathcal{G}^o$, is followed. Equation (3.55) is valid for each iso-contour of $\mathcal{Y} \in [\mathcal{Y}_u, \mathcal{Y}_b]$. In addition, the burning velocity s_L is a field quantity, whereas in the $\mathcal{G}$-equation approach, it is only defined at $\mathcal{G} = \mathcal{G}^o$.

The kinematic equation (3.55) is used to rewrite the three-dimensional conservation equations in a set of quasi one-dimensional conservation equations, describing the processes in the direction perpendicular to the iso-contours in a flame adapted coordinate system. Combination of the continuity equation (2.1) and the expression for the flame velocity (3.54) leads to

$$\frac{\partial \rho}{\partial t} + \nabla \cdot (\rho \boldsymbol{u}_f) = -\nabla \cdot (\rho s_L \boldsymbol{e}_\eta). \tag{3.56}$$

The transport locally perpendicular to the iso-contour is gathered in the right-hand side of equation (3.56). The terms on the left-hand side can be considered as the amount of mass that is transported along the iso-contours. This phenomenon is also known as flame stretch, which is described by the stretch rate K. In [39], the stretch rate is defined as the change of mass $M(t)$, which is defined as

$$M(t) = \int_{V(t)} \rho \mathrm{d}V, \tag{3.57}$$

in an infinitesimal volume $V(t)$ that moves with a velocity $\boldsymbol{u}_f$:

$$K = \frac{1}{M} \frac{\mathrm{d}M}{\mathrm{d}t}. \tag{3.58}$$

Using the Reynolds transport theorem, the following expression for K is obtained

$$\rho K = \frac{\partial \rho}{\partial t} + \nabla \cdot (\rho \boldsymbol{u}_f). \tag{3.59}$$

Combination of (3.56) and (3.59) leads to

$$\nabla \cdot (\rho s_L \boldsymbol{e}_\eta) = -\rho K. \tag{3.60}$$

The conservation equation for $\mathcal{Y}$ in the original coordinate system is given by

$$\frac{\partial \mathcal{Y}}{\partial t} + \nabla \cdot (\rho \boldsymbol{u} \mathcal{Y}) - \nabla \cdot \left(\frac{\lambda'}{c_p Le_y} \nabla \mathcal{Y} \right) = s_y. \tag{3.61}$$

Together with (3.53), (3.54), and (3.59), equation (3.61) can be written as

$$\nabla \cdot (\rho s_L \mathcal{Y} \boldsymbol{e}_\eta) - \nabla \cdot \left(\frac{\lambda'}{c_p Le_y} \nabla \mathcal{Y} \right) = s_y - \rho K \mathcal{Y}. \tag{3.62}$$

Analogous to equation (3.60), the transport processes along the iso-contours are gathered in the perturbation term $\rho K \mathcal{Y}$. With the introduction of the mass-burning rate $m = \rho s_L$ and σ, which is a measure of the area through which the transport

takes place, the three-dimensional conservation equations for mass, species mass fractions and enthalpy can be rewritten in a one-dimensional form,

$$\frac{\mathrm{d}}{\mathrm{d}s}(\sigma m) = -\sigma \rho K, \tag{3.63}$$

$$\frac{\mathrm{d}}{\mathrm{d}s}(\sigma m Y_i) - \frac{\mathrm{d}}{\mathrm{d}s}\left(\sigma \frac{\lambda'}{c_p Le_i}\frac{\mathrm{d}Y_i}{\mathrm{d}s}\right) - \sigma s_i = -\sigma \rho K Y_i + Q_i, \quad i \in [1, N_s - 1], \tag{3.64}$$

and

$$\frac{\mathrm{d}}{\mathrm{d}s}(\sigma m h) - \frac{\mathrm{d}}{\mathrm{d}s}\left(\sigma \frac{\lambda'}{c_p}\frac{\mathrm{d}h}{\mathrm{d}s}\right) - \frac{\mathrm{d}}{\mathrm{d}s}\left(\sigma \frac{\lambda'}{c_p}\sum_{i=1}^{N_s} h_i^* \left(\frac{1}{Le_i} - 1\right)\frac{\mathrm{d}Y_i}{\mathrm{d}s}\right) = -\sigma \rho K h + Q_h. \tag{3.65}$$

The equations are parameterised with the spatial coordinate s, which is the arc-length perpendicular to the iso-surfaces, i.e. $\mathrm{d}s = h_\eta \mathrm{d}\eta$. The perturbation terms Q_i and Q_h describe instationary terms within the moving frame, and diffusion of Y_i and h along the iso-contours of $\mathcal{Y}$, which originate from the fact that the iso-contours of the progress variable generally do not coincide with the iso-contours of Y_i and Y_h. The set of equations (3.63)-(3.65) are also known as the flamelet equations, which completely describe the internal structure of a flame. Together with the kinematic equation for the flame front (3.53), the flamelet equations fully represent the three-dimensional conservation equations for mass, species mass fractions, and the enthalpy. The only assumption that is made in this analysis, is the presence of a flame front, which means that ignition and extinction phenomena are not taken into account.

3.4.2 Manifold method

In this section, the FGM reduction method is explained. Only the general principles will be presented. For more details, the reader is referred to [68]. In the FGM method, the solution of one-dimensional premixed flames, i.e the solution of (3.63)-(3.65) for the case that $K = Q_i = Q_h = 0$ and $\sigma = 1$, is used to construct a manifold. It is assumed that the effect of the perturbation terms K, Q_i, Q_h, and σ on the chemistry is small. This implies that, even though the result of a three-dimensional flame may be quite different from a one-dimensional flame in the spatial domain, the difference in the composition space is small. This assumption has been confirmed by numerical tests of two-dimensional flames in [68].

Like in the ILDM method, a distinction is made between reacting controlling variables $\mathcal{Y}$ and non-reacting controlling variables c. The reacting controlling variables describe the reaction progress for a given value of the non-reacting controlling variables. The non-reacting controlling variables describe the variation of the conserved variables. For convenience, the FGM procedure is first explained for a one-dimensional manifold, i.e. a manifold with a single controlling variable $\mathcal{Y}$.

A one-dimensional FGM is obtained from the solution of the flamelet equations for the case of a freely propagating adiabatic flame. Hence, boundary conditions at the unburnt side are given by

$$\boldsymbol{Y}(s \to -\infty) = \boldsymbol{Y}^{\text{ref}}, \tag{3.66}$$

$$h(s \to -\infty) = h^{\text{ref}}. \tag{3.67}$$

The boundary conditions at the burnt side are given by

$$\frac{\mathrm{d}\boldsymbol{Y}}{\mathrm{d}s}(s \to \infty) = \boldsymbol{0}, \tag{3.68}$$

$$\frac{\mathrm{d}h}{\mathrm{d}s}(s \to \infty) = 0. \tag{3.69}$$

In addition, the flame is one-dimensional, which implies that $K = Q_i = Q_h = 0$ and $\sigma = 1$.

The solution of the flamelet equations is a trajectory in the composition space. This trajectory can be parameterised by a controlling variable $\mathcal{Y}$. An example of such a one-dimensional FGM is shown in figure 3.10, which shows the solution of the flamelet equations for a hydrogen/air system.

Once the manifold is obtained, it is stored in a database. During the application, only the conservation equation for the controlling variable is solved, together with conservation equations for mass and momentum. The dependent variables, such as e.g. the chemical source term of the controlling variable, the density and the temperature are retrieved from the database. Similar to the ILDM method, perturbations which cause deviations from the manifold should be projected on the manifold. However, in the ILDM method, the perturbation terms are projected on the manifold, using the eigenvectors of the Jacobian. On the other hand, in the FGM method, these eigenvectors are not available and projection is not straight-forward, as the result depends on the choice of the controlling variable. However, in case of ILDM, the major perturbations are caused by diffusion. In the FGM, diffusive processes are included in the manifold and perturbations mainly originate from multi-dimensional effects. If the multi-dimensional perturbations are small, the differences caused by the choice of the controlling variable will also be small and projection is obtained by taking only the component of the perturbations that is in the manifold into account [68].

Analogous to the ILDM method, the dimension of the manifold can be increased to capture more time scales. However, the procedure to increase the dimension of the manifold is not straight-forward. In this case, a series of one-dimensional flamelets is computed, with a varying inlet composition. The inlet composition is varied in such a manner that the chemical equilibrium composition remains unchanged, i.e. the enthalpy, element fractions and the pressure of the inlet mixtures are unchanged. Unlike an ILDM, the shape of the manifold depends on the choice of the additional controlling variable(s), so the choice of the additional controlling variables depends on the insight and experience of the user.

Equivalent to the ILDM method, extra dimensions can be added to the manifold to capture variations in the enthalpy, element fractions, and the pressure. For example, to be able to model a flame, which is partially premixed, the mixture fraction can be added as an additional degree of freedom to the manifold. In this case, a series of flamelets is computed with different mixture fractions at the inlet. In Van Oijen and De Goey [71], a two-dimensional FGM, with the mixture fraction as additional controlling variable, is used to model a so-called triple flame successfully. Similarly, the enthalpy can be added as an additional controlling variable to model flames with heat-losses [69,72].

3.5   Comparison of ILDM and FGM

In this chapter, a number of chemical reduction methods are briefly discussed. Furthermore, the ILDM method and the FGM method are discussed in more detail. The chapter is concluded with a qualitative comparison between the ILDM and the FGM method, as both methods have a number of advantages and disadvantages. Two major distinctions can be made between the ILDM and the FGM method. The first difference is found in the way the manifold is obtained. In the ILDM analysis, the choice of which processes are assumed in steady-state is based on a time scale analysis of the chemical source term, whereas such a time scale analysis is not performed in the FGM method. Secondly, as the FGM method is based on one-dimensional flamelet equations, transport processes are included in the manifold, whereas the ILDM manifold is based on an analysis of the chemical system, without transport processes. From these two major differences, a number of advantages and disadvantages arise, which are summarised in table 3.1.

The major advantage of the time scale analysis that is performed in the ILDM method, is that information about the attractiveness of the manifold is available. On the other hand, if the fast and slow time scales are badly separated, the ILDM will be inaccurate. Furthermore, if eigenvalues cross, it can be a problem to obtain a solution.

The inclusion of transport processes in the FGM, results in a high accuracy with only a few controlling variables. To obtain a comparable accuracy with ILDM, the number of controlling variables is increased, which results in a large database and a less efficient reduction. Furthermore, especially a one-dimensional FGM is relatively easy to obtain. On the other hand, the extension to more dimensions is less straight-forward than in case of an ILDM. As an FGM is based on the solution of premixed flames, the manifold is only applicable to (partially-) premixed systems, whereas the ILDM is applicable to both premixed and non-premixed flames. The applicability of FGM to partially-premixed systems will be investigated further in chapter 4.

In chapter 5, the Phase Space ILDM method is introduced [7]. This method is

Table 3.1 : The advantages and disadvantages of ILDM and FGM.

	ILDM	FGM
Advantages:	Manifold based on time scale analysis	accurate
	suited for premixed and non-premixed systems	few progress variables are sufficient
	-	relatively simple to obtain
	-	no projection needed
Disadvantages:	difficult to obtain solution in entire domain (crossing eigenvalues)	no time scale analysis: no information about attractiveness
	more dimensions needed to obtain high accuracy	not straight-forward to extend to more dimensions
	transport processes not included	developed for premixed systems

basically a combination of the ILDM and the FGM method. It combines the time scale analysis of the ILDM method with the flamelet equations, which are used to construct a FGM.

The Flamelet-Generated Manifold method applied to partially-premixed counterflow flames

As stated in the previous chapter, the FGM method is originally designed for premixed flames. Therefore, its applicability to systems, which are not purely premixed is questionable. In this chapter, the FGM method is tested in a counterflow configuration that is not purely premixed. The accuracy of the reduced computations is analysed by means of a time scale analysis of the terms that cause deviations from a purely premixed flame, which is one-dimensional. Furthermore, the results are compared with computations, performed with a flamelet database, which is based on non-premixed flamelets.

The chapter starts with a motivation of this study in section 4.1. In the subsequent section 4.2, the research strategy is defined. First, the counterflow configuration is discussed. Subsequently, it is specified how the FGM method can be used in a system, which is not purely premixed. In the third section, an overview of the results is given. The results are analysed in section 4.4. In subsequent section 4.5, a comparison with results obtained with a non-premixed database is presented. Finally, a number of conclusions is drawn in section 4.6.

4.1   Introduction

Partially-premixed flames constitute a special field of interest, as they are found in a wide range of practical applications, varying from gas turbines, reciprocating engines, and industrial and domestic burners. It is well known that purely premixed flames and purely non-premixed flames can be modelled by using one-dimensional premixed and non-premixed flamelets, respectively. For partially-premixed flames, however, it is unclear which model to use. A combination between premixed and non-premixed flamelets to model partially premixed flames was proposed by Müller *et al.* [62] and Chen *et al.* [14]. In this method, the $\mathcal{G}$-equation approach was used to describe the position and the propagation of the premixed flame front, whereas a li-

brary based on counterflow diffusion flames was used to predict the concentrations of the chemical components. However, as the premixed character of the combustion processes has been identified as the most dominant part [14, 77], the use of non-premixed flamelets is questionable and using premixed flamelets to construct a database seems to be more appropriate. A number of references in which the FGM method has been used to model partially-premixed flames can be found in literature. Accurate reproduction of detailed results of temperature and species profiles are obtained in a two-dimensional triple flame [71] and a two-dimensional Bunsen flame [35]. Notice that in the second example, the FPI method was used. However, this method is similar to the FGM method. In this chapter, the FGM method, which is based on premixed flamelets, is tested in a system that is partially-premixed. Furthermore, the FGM results are compared with results obtained with a non-premixed flamelet library.

A typical example of a partially-premixed flame is a so-called triple flame. Triple flames are found in e.g. lifted-jet diffusion flames. Furthermore, triple flames play an important role in the stabilisation of turbulent diffusion flames [22]. Figure 4.1 shows a schematic picture of a triple flame structure propagating in a non-uniform mixture. Several areas can be distinguished in this flame. First, the triple point is situated at the position on the premixed flame front, where the mixture fraction Z equals its stoichiometric value Z_{st}. Furthermore, two premixed flames can be seen: a lean premixed flame at the fuel lean side of the mixture ($Z < Z_{st}$) and a rich premixed flame at the fuel rich side of the mixture ($Z > Z_{st}$). Finally, a diffusion flame is found in the tail of the triple, or tri-brachial flame structure. The behaviour and characteristics of triple flames are not studied here. For experimental studies of a triple flame, the reader is referred to e.g. [44, 52, 53, 77]. Furthermore, theoretical studies of triple flames are reported in, for example, [10, 21, 46] and numerical studies can be found in, for instance, [22, 24, 83]. In this chapter, it is analysed to what extent the FGM method, which is based on premixed flamelets, can be used in triple flame systems. By means of a time scale analysis of chemical and physical processes, it is analysed which processes lead to inaccuracies in the reduced computation.

In a triple flame, a number of features, which are not present in one-dimensional premixed flames, can be distinguished:

1. Curvature and stretching due to the non-uniform velocity field and the curved flame front.
2. A rich and a lean premixed flame front, in which the mixture fraction Z is not constant, unlike in purely premixed flames.
3. A diffusion flame front, in which CO and H_2, which are left over from the rich premixed flame, react with O_2, which is left over from the lean premixed flame.

As none of these processes are taken into account during the generation of an FGM, all may cause inaccuracies in the reduced computation with FGM. Unfortunately,

Within the figure:

rich premixed flame

CO, H_2

$Z > Z_{st}$

triple point

diffusion flame

unburnt mixture

burnt mixture

$Z = Z_{st}$

$Z < Z_{st}$

O_2

lean premixed flame
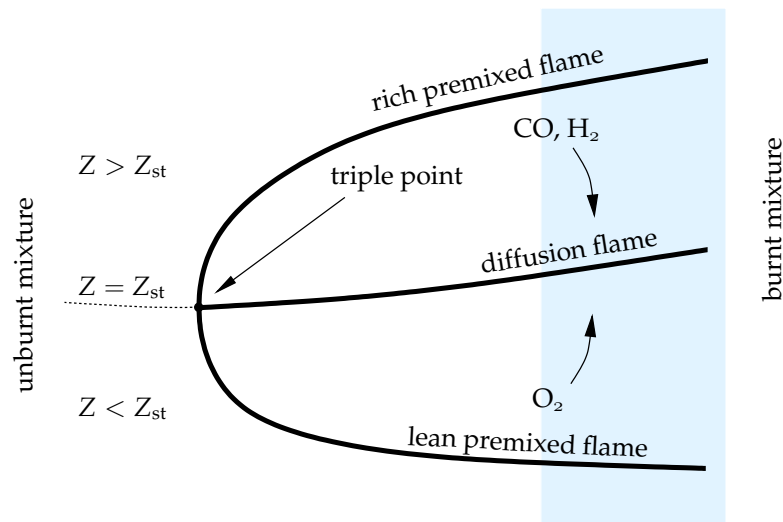
Figure 4.1 : A schematic example of a triple flame structure. The flame structure in the grey box is similar to the structure in a one-dimensional counterflow system, which is partially-premixed. The flame propagates towards the left.

in the triple flame structure, these features can not be isolated to investigate the individual contributions to the inaccuracies in the reduced computations.

As stated earlier, the results of FGM are also compared with results obtained with a non-premixed flamelet library. In the non-premixed counterflow flames, which are used to construct a non-premixed flamelet library, especially the premixed flame structure is not present. Therefore, it is expected that the largest deviations from detailed results are found in the premixed parts of the partially-premixed flame.

The effect of stretch and curvature on the accuracy of computations with the FGM method has already been investigated [68]. It is expected that the main deviation from one-dimensional premixed behaviour is caused by the gradients in the mixture fraction. In a two or three-dimensional triple flame simulation, it is difficult to control the gradient of the mixture fraction directly. The gradient of the mixture fraction is supplied at the left boundary of the domain in figure 4.1. However, due to diffusion processes, the mixture fraction gradient diminishes in the stream-wise direction. Hence, it is hard to find a relation between the gradient of the mixture fraction and the accuracy of the FGM computation. The tail of the triple flame (the box in figure 4.1) can be simulated with a one-dimensional counterflow flame, which is partially-premixed.

The one-dimensional counterflow setup can be considered as a one-dimensional triple flame, in which it is possible to change the local strain rate and the mixture fraction gradient more or less independently. It is assumed that all Lewis numbers are equal to one (i.e. $Le_i = 1$ for $i \in [1, N_s]$) to eliminate the effects of preferential diffusion. In this manner, the individual contributions of straining and a gradient of the mixture fraction to inaccuracies of the reduced computations can be analysed. The
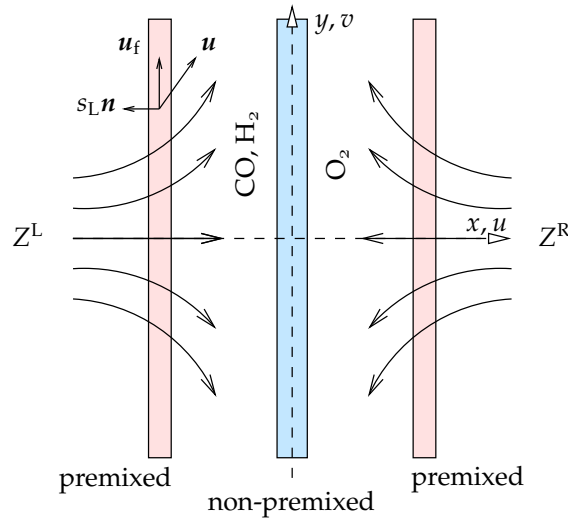
Figure 4.2 :   A schematic example of a planar counterflow flame, which is partially-premixed. In this example, it is assumed that $Z^L > Z_{st}$ and $Z^R < Z_{st}$. Note that the location of the non-premixed flame depends on position, where $Z = Z_{st}$.

accuracy of the reduced computation is analysed by means of a time scale analysis of the terms, which cause perturbations from one-dimensional premixed behaviour. Recently, in Fiorina *et al.* [36] counterflow flames that are partially-premixed are used to study the accuracy of the FGM/FPI method. However, in their work, the main focus was not on the individual contributions of the perturbation terms, but on how a database generated with premixed flamelets can be combined with a database generated with non-premixed flamelets to model partially-premixed flames with a large mixture fraction gradient.

4.2   Partially-premixed counterflow flames

The one-dimensional counterflow flame that is studied, is formed by two opposed methane/air jets with mixture fractions Z^L and Z^R, respectively, which impinge and form a stagnation plane (see figure 4.2). If Z^L and Z^R are both within the flammability limits and $Z^L = Z^R$, a so-called twin flame with two premixed flame fronts appears. If $Z^L = 1$ and $Z^R = 0$, a single diffusion flame front appears around the position where $Z = Z_{st}$. If the mixture fraction on one side is larger than the stoichiometric value and on the other side, the mixture fraction is smaller than the stoichiometric value, then the counterflow flame can be considered as a partially-premixed flame. Figure 4.2 shows an example of a partially-premixed counterflow flame, with two premixed flame fronts and a non-premixed flame front in between.

4.2.1 One-dimensional counterflow flames

A derivation of the set of steady one-dimensional equations that describes the counterflow flame can be found in, e.g. [20, 70]. Here only the resulting equations are presented. As the counterflow flames are considered to be flat and stationary, the variables ρ, T, Y_i, and h only depend on the coordinate x, which is the coordinate perpendicular to the flame front(s). The pressure and v, which is the y-component of the velocity, depend both on x and y. As the flame is steady, the velocity of the flame surfaces is given by $\boldsymbol{u}_f = v\boldsymbol{e}_y$. Combining this expression with equation (3.59) leads to

$$K = \frac{\partial v}{\partial y}. \tag{4.1}$$

Together with this expression for the stretch rate, the conservation equations for mass, species mass fractions, and enthalpy can be written as,

$$\frac{dm}{dx} = -\rho K, \tag{4.2}$$

$$\frac{d}{dx}(mY_i) - \frac{d}{dx}\left(\frac{\lambda'}{c_p Le_i}\frac{dY_i}{dx}\right) - s_i = -\rho K Y_i, \qquad i \in [1, N_s - 1], \tag{4.3}$$

and

$$\frac{d}{dx}(mh) - \frac{d}{dx}\left(\frac{\lambda'}{c_p}\frac{dh}{dx}\right) = \frac{d}{dx}\left(\frac{\lambda'}{c_p}\sum_{i=1}^{N_s-1} h_i^*\left(\frac{1}{Le_i} - 1\right)\frac{dY_i}{dx}\right) - \rho K h. \tag{4.4}$$

It should be noticed that this set of equations is equal to the flamelet equations (3.63)-(3.65) for the case that $\sigma = 1$ (no curvature) and $Q_i = Q_h = 0$ (all flame variables are a function of x only). As the iso-contours of the progress variable $\mathcal{Y}$ are flat and parallel, the spatial coordinate x is analogous to the coordinate s, which is used in the flamelet equations.

In this flame configuration, two perturbations from one-dimensional unstretched premixed flames are significant. Firstly, straining of the flame front, expressed by the stretch rate K, influences the mass burning rate m. Even though it has been shown in [37, 70] that this effect on the chemistry is relatively small for premixed flames, this is uncertain for partially-premixed flames. Secondly, if $Z^L \neq Z^R$, the gradient of the mixture fraction may lead to deviations from purely one-dimensional behaviour. An expression for the stretch rate K can be derived from the conservation equations for momentum [20]. The equation that is solved for the stretch rate K yields,

$$m\frac{dK}{dx} - \frac{d}{dx}\left(\mu\frac{dK}{dx}\right) = \rho^R a^2 - \rho K^2, \tag{4.5}$$

where a is the applied strain at the right boundary. In this equation, it is assumed that the flow in the unburnt mixture behaves as a potential flow. Since it is assumed that $Le_i = 1$ for all species, the conservation equation for the mixture fraction is given by,

$$\frac{d}{dx}(mZ) - \frac{d}{dx}\left(\frac{\lambda'}{c_p}\frac{dZ}{dx}\right) = -\rho K Z. \tag{4.6}$$

where Z is given by equation (3.15) In addition, a scaled mixture fraction $\tilde{Z}$ can be defined, which varies between 1 at the left-hand (rich) side and 0 at the right-hand (lean) side, according to $\tilde{Z} = (Z - Z^{\mathrm{R}})/(Z^{\mathrm{L}} - Z^{\mathrm{R}})$, provided that $Z^{\mathrm{L}} \neq Z^{\mathrm{R}}$.

The system of equations is solved with the one-dimensional flame code CHEM1D [12], with the following boundary conditions,

$$
\begin{aligned}
&m(0) = 0, \\
&Y_i(x \to -\infty) = Y_i^{\mathrm{L}}, \qquad Y_i(x \to +\infty) = Y_i^{\mathrm{R}}, \quad i \in [1, N_{\mathrm{s}}], \\
&h(x \to -\infty) = h^{\mathrm{L}}, \qquad h(x \to +\infty) = h^{\mathrm{R}}, \\
&K(x \to -\infty) = a\sqrt{\tfrac{\rho^{\mathrm{R}}}{\rho^{\mathrm{L}}}}, \quad K(x \to +\infty) = a, \\
&Z(x \to -\infty) = Z^{\mathrm{L}}, \qquad Z(x \to +\infty) = Z^{\mathrm{R}}.
\end{aligned}
\tag{4.7}
$$

4.2.2   FGM for partially-premixed flames

In order to capture mixture fraction variations, a two-dimensional FGM is constructed. The manifold consists of a series of premixed flamelets, with different inlet mixture fractions, parameterised with the progress variables Z and $\mathcal{Y}$. The mixture fraction represents the mixing between fuel and oxidiser, whereas $\mathcal{Y}$ parameterises the reaction progress. To obtain a higher accuracy, additional reaction progress variables can be added to the manifold. However, this is not done here. The reaction progress variable $\mathcal{Y}$ is defined as

$$
\mathcal{Y} = \frac{Y_{\mathrm{CO_2}}}{M_{\mathrm{CO_2}}} + \frac{Y_{\mathrm{H_2O}}}{M_{\mathrm{H_2O}}} + \frac{Y_{\mathrm{H_2}}}{M_{\mathrm{H_2}}},
\tag{4.8}
$$

with M_i the molar mass of species i [71]. This progress variable is continuously increasing for both rich and lean premixed flames. Note that the choice of the controlling variable is not arbitrary. Firstly, one must guarantee a unique parameterisation of the manifold. Secondly, the controlling variable must be suited for non-premixed and partially-premixed flames. It should be noted that the main purpose is an accurate prediction of the reaction layer (see figure 1.2). However, an accurate prediction of the density profile is essential for a correct prediction of the flow and hence also the flame behaviour.

A series of 80 premixed adiabatic unstrained flamelets has been computed of methane/air mixtures with the inlet mixture fraction varying between $Z = 0.022$ (which is equivalent to an equivalence ratio of $\varphi \approx 0.39$) for the leanest flamelet and $Z = 2Z_{\mathrm{st}} \approx 0.11$ (or $\varphi \approx 2.12$) for the richest flamelet. The inlet mixture fraction is modified by adjusting the ratio between fuel and air. Since the Lewis numbers are equal to one, the mixture fraction is constant in each flamelet. A projection of the computed manifold onto the $(\mathcal{Y}, Z)$-plane is shown in figure 4.3. Points at intermediate values of Z can be obtained by interpolation.

The values of the mixture fraction that can be chosen to compute a premixed flamelet, are restricted to the flammability limits. If the value of Z reaches values
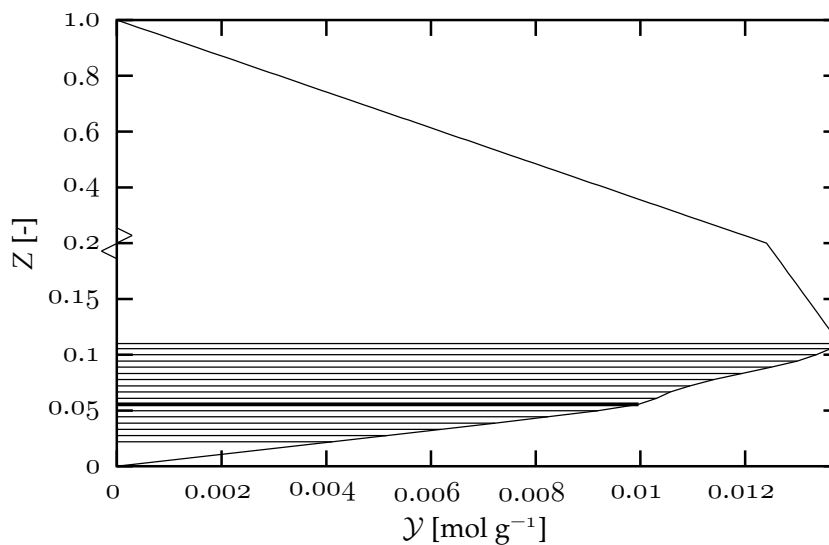
Figure 4.3 : The FGM manifold projected on the $(\mathcal{Y}, Z)$-plane. Notice that the scale changes on the vertical axis at $Z = 0.2$. The thick solid line represents the stoichiometric flamelet. Furthermore, only 17 of the 80 flamelets are shown.

outside the flammability limits during the application of the FGM, an extrapolation of the dependent variables like T and ρ must be used. Since the chemical source terms are very small outside the flammability limits, a reasonable approximation for the solution of Y_i is proportional to the solution of Z, i.e. $Y_i \sim Z^{Le_i}$. Since the Lewis numbers are assumed to be equal to one, the enthalpy is also a linear function of Z. Once the species mass fractions and the enthalpy are known, the temperature can be calculated with the caloric equation of state (2.6). Finally, the density is obtained from the thermal equation of state (2.11). A more detailed description of data retrieval from the database is given in appendix B.

4.2.3 Non-premixed flamelets

Instead of using premixed flamelets to model a partially-premixed flame, it is also possible to construct a database with non-premixed flamelets. A database is constructed with the solution of non-premixed counterflow flames (i.e. counterflow flames with $Z^L = 1$ and $Z^R = 0$), with a varying strain rate a. A series of 52 flamelets is computed with a strain rate varying between $a = 0.05 \text{ s}^{-1}$ and $a = 315 \text{ s}^{-1}$. The database is completed with a chemical equilibrium flamelet, which represents the limit $a \rightarrow 0$. In this equilibrium flamelet, the composition is determined by the chemical equilibrium values as a function of Z.

The manifold is parameterised by the mixture fraction Z and the scalar dissipation rate χ. Analogous to the FGM method, the mixture fraction represents the mixing between fuel and oxidiser. A second controlling variable is added to capture finite rate chemistry effects. Similar to the FGM method, this can be a (linear combination of) species mass fractions. However, in standard non-premixed flamelet
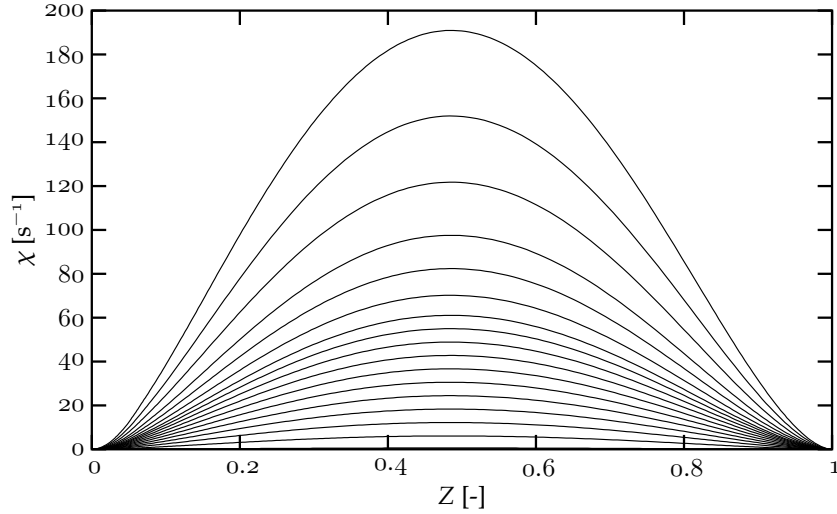
Figure 4.4 : The diffusion flamelet database, projected on the (Z, χ)-plane. Note that not all the flamelets are shown.

techniques, the scalar dissipation rate is usually chosen as additional controlling variable [76]. A projection of the manifold on the (Z, χ)-plane is shown in figure 4.4.

In most flamelet libraries, the flamelets are computed in Z-space rather than in x-space [76]. In that case, spatial information of the flame is not available. It is assumed that the χ-profile can be approximated with an analytical function. Here, the diffusion flame is computed in the spatial domain, so no assumptions for the χ-profile are needed, and the solutions of Z and χ can be used to parameterise the database.

During the application of the database, Z and χ are used as controlling variables. This means that equation (4.6) is solved for the mixture fraction and the value of χ is retrieved from the definition of χ, i.e. $\chi = 2D_Z \|\nabla Z\|^2$. The data is retrieved from the database in a similar fashion as in the FGM method, i.e. by means of linear interpolation between the available manifold data. As the manifold grid is not rectangular, linearly interpolating may lead to errors. However, if the number of points in each flamelet is significantly large, the error induced by interpolation will be small. The flamelets, which are used to construct the database, contain 400 grid points per flamelet.

4.3 Results with FGM

In this section, results are presented for partially-premixed counterflow flames that are computed with the FGM. The results are compared with the results of detailed computations. In section 4.5, the results which are obtained with the FGM method are compared with results obtained with non-premixed flamelets.

As stated in the previous section, there are two effects that contribute to errors using FGM in the simulations of partially-premixed counterflow flames, i.e. strain

and a gradient in Z, which can be expressed by the stretch rate K and the scalar dissipation rate χ, respectively. However, as effects due to the gradients of Z are of interest, a more appropriate mixing time scale in terms of the local dissipation rate is introduced according to

$$\tilde{\chi} = \frac{\chi}{2(Z_r - Z_l)^2},$$
(4.9)

which is a rescaled dissipation rate. The subscripts 'r' and 'l' stand for the rich and the lean flammability limits of the premixed CH_4/air flames. In this analysis, the values for Z_r and Z_l are given by $Z_r = 0.11$ and $Z_l = 0.022$. The two effects that cause deviations from premixed behaviour can be controlled in two ways:

1. The stretch rate K can be influenced by changing the strain rate at the oxidiser boundary a. Unfortunately, when a is changed, the dissipation rate $\tilde{\chi}$ changes as well.

2. The mixture fractions at the boundaries, i.e. Z^L and Z^R, can be changed. In order to keep the value of K constant or nearly constant at $Z = Z_{st}$, Z^L and Z^R are changed symmetrically with respect to $Z_{st} \approx 0.055$, such that $Z^L + Z^R = 2Z_{st}$. The limits of the Z-range are given by the twin flame, i.e. by $Z^L = Z^R = Z_{st}$ and a flame with $Z^L = 2Z_{st}$ and $Z^R = 0$. In the second limiting case, a rich premixed flame front appears together with a non-premixed flame front, in which the remaining CO and H_2 react with the oxygen that is coming from the lean side. In the other cases, a triple flame appears as shown in figure 4.2.

Figure 4.5 shows the test data as a function of K and $\tilde{\chi}$, evaluated at $Z = Z_{st}$. Each point represents a different flame configuration, in which open symbols correspond to steps in the applied strain a and closed symbols correspond to steps in Z^L and Z^R. From the test data, the effects of straining and mixing are extracted. First the effect of strain is evaluated. Subsequently, the effect of a gradient of Z is studied. Furthermore, the combined effect of strain and mixing is presented. In addition, the profiles of a number of variables are given. Finally, the results are briefly summarised.

4.3.1 Straining of the flow

To show the effect of straining of the flow, the results of two flames with different strain rates are evaluated. The values of Z^L and Z^R are chosen in such a manner that the profile of the scalar dissipation rate is approximately the same for both flames, so the effect of mixing is also almost the same for both flames. Figure 4.6a shows profiles of K and $\tilde{\chi}$ as a function of the mixture fraction for the two different flames. The first flame has a strain rate $a = 100 \text{ s}^{-1}$ and inlet mixture fractions $Z^L = 2Z_{st} \approx 0.11$ and $Z^R = 0.0$, respectively. The second flame has a strain rate of $a = 1000 \text{ s}^{-1}$ and inlet mixture fractions $Z^L = 0.07267$ and $Z^R = 0.03767$, respectively. Notice that the mixture fraction is scaled with the values at the boundaries, so it varies between $0 \leq \tilde{Z} \leq 1$. Figure 4.6a shows that the dissipation rate of both flames are
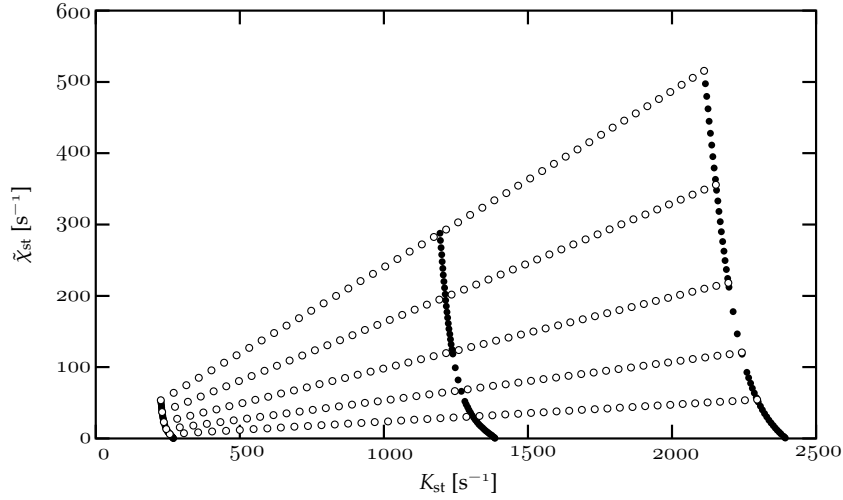
Figure 4.5 : The tested flame configurations as a function of K_{st} and $\tilde{\chi}_{st}$. The open circles represent steps in the applied strain, and the closed circles represent steps in Z^L and Z^R.

comparable, whereas the strain rate is completely different. Figure 4.6b shows the profiles of the progress variable $\mathcal{Y}$, as a function of the (unscaled) mixture fraction Z. The profiles of the detailed simulations are compared with the FGM solutions. To quantify the error of the FGM simulation, the following expression is used

$$\epsilon_{\mathcal{Y}} = \frac{\int_{Z^R}^{Z^L} |\mathcal{Y}^{det} - \mathcal{Y}^{FGM}| dZ}{\int_{Z^R}^{Z^L} \mathcal{Y}^{det} dZ}, \tag{4.10}$$

where $\mathcal{Y}^{det}$ and $\mathcal{Y}^{FGM}$ are the profiles of the progress variable of the detailed solution and the profile of the FGM solution, respectively. The error for the flame with $a = 1000\ \mathrm{s}^{-1}$ is $\epsilon_{\mathcal{Y}} \approx 4.8\%$ and for the flame with $a = 100\ \mathrm{s}^{-1}$, the error is $\epsilon_{\mathcal{Y}} \approx 3.4\%$. From this observation, it can be concluded that, for a given value of the gradient of Z, strain has only little effect on the accuracy of the reduced computation.

At high strain rates, the flame fronts are pressed against each other. This leads to an extra deviation from one-dimensional premixed behaviour, because radicals like H, OH, and O, which are present in the burnt gases, diffuse from one flame front to the other. Figure 4.7 shows the overall chemical time scale τ_c, as defined in equation (3.13), for two flames with $Z^L = 2Z_{st}$ and $Z^R = 0$, and strain rates $a = 100$ s^{-1} and $a = 1000\ \mathrm{s}^{-1}$, respectively. The flame with $a = 100\ \mathrm{s}^{-1}$ clearly has two flame fronts: a rich premixed flame front at the right-hand side and a diffusion flame front around $Z = Z_{st} \approx 0.055$. In the flame with $a = 1000\ \mathrm{s}^{-1}$, the two separate flame fronts can not be distinguished. Note that the time scales in both flames are different. This phenomenon will be analysed later in this chapter. The merging of the flame fronts also occurs in flames with other mixture fraction at the boundaries. In the FGM computation, the diffusion that is caused by the merging of the flame fronts can not be reproduced, as it is not taken into account in the construction of the database. This result is analogous to earlier results found for purely premixed

(a)   (b)
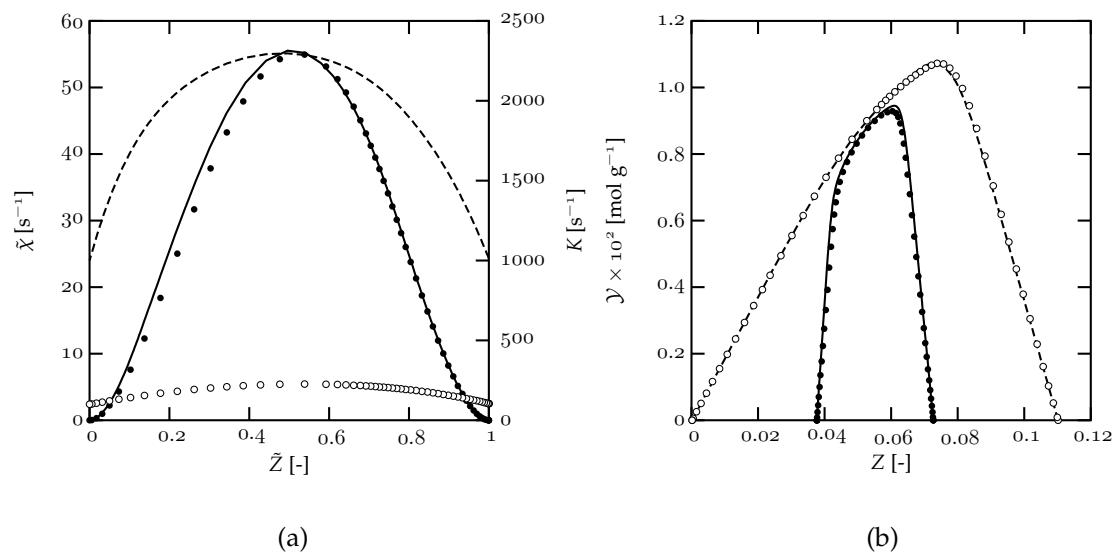
Figure 4.6 : The effect of straining on the FGM solution. The left figure shows the $\tilde{\chi}$-profile
(solid line) and the K-profile (dashed line) for $a = 1000$ s^{-1} and the $\tilde{\chi}$-profile
(closed symbols) and the K-profile (open symbols) for $a = 100$ s^{-1}. Note that
the profiles are plotted as function of $\tilde{Z}$. The right figure shows the profiles
of $\mathcal{Y}$ for both flames: the detailed (solid line) and the FGM (closed symbols)
solution for $a = 1000$ s^{-1} and the detailed (dashed line) and the FGM (open
symbols) solution for $a = 100$ s^{-1}.

counterflow flames [70]. The effect of the merging of the flame fronts is not very
large in figure 4.6b. In the flame with $a = 1000$ s^{-1}, both Z^L and Z^R are within
the flammability limits, so most of the chemistry takes place in the premixed flame
fronts, which are relatively far apart.

4.3.2   The effect of mixing

In the second test case, the strain rate a is kept constant and the inlet mixture frac-
tions are changed, corresponding to the closed symbols in figure 4.5. The inlet mix-
ture fraction on the left hand side changes from $Z^L \in [Z_{st}, 2Z_{st}]$, whereas the mixture
fraction on the right-hand side varies from $Z^R \in [Z_{st}, 0]$. Furthermore, Z^L and Z^R
satisfy the condition $Z^L + Z^R = 2Z_{st}$. The test is done for three different strain rates,
i.e. $a = 100$ s^{-1}, $a = 550$ s^{-1}, and $a = 1000$ s^{-1}, respectively. Figure 4.8 shows the
error as a function of $\tilde{\chi}_{st}$. The corresponding strain rates can be obtained from fig-
ure 4.5. The error grows for increasing $\tilde{\chi}_{st}$, as expected. Note that $\epsilon_\mathcal{Y} > 0$ for $\tilde{\chi}_{st} \to 0$,
since K_{st} is still positive (see figure 4.5).

However, at a certain value of $\tilde{\chi}_{st}$, the error increases less or even decreases, de-
pending on the applied strain. The cause of this phenomenon is shown in figure 4.9,
which shows profiles of $\mathcal{Y}$ and τ_c of two flames at a strain rate of $a = 100$ s^{-1} with
different mixture fractions at the inlet. The profile in figure 4.9b, with $\tilde{\chi}_{st} \approx 55$ s^{-1},
results in a lower value of $\epsilon_\mathcal{Y}$ than the profile of figure 4.9a, with $\tilde{\chi}_{st} \approx 30$ s^{-1}. The
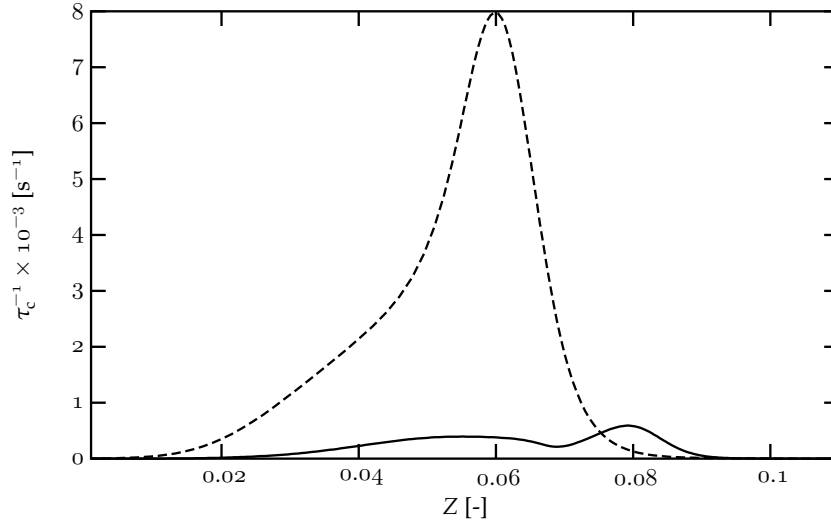
Figure 4.7 :   The merging of two flame fronts at higher strain rates, shown by the chemical time scales as a function of the mixture fraction. Solid line: $a = 100\,\text{s}^{-1}$, dashed line: $a = 1000\,\text{s}^{-1}$.

main difference between the two flames is shown by the profile of τ_c. The flame in the left figure has two premixed flame fronts with a non-premixed flame in between. The decrease in the error is mainly caused by the extinction of the lean premixed flame in figure 4.9b, because the inlet mixture fraction on the lean side reaches values below the lean flammability limit. The reproduction by FGM of the diffusion flame is clearly more accurate than the lean premixed flame. This will be explained in detail in section 4.4.

4.3.3   The combined effect of strain and mixing

Finally, the inlet mixtures are kept constant, but the strain rate is varied, i.e. the lines with open symbols in figure 4.5. The strain rate varies between $a = 100\,\text{s}^{-1}$ and $a = 1000\,\text{s}^{-1}$. The test is repeated with five different inlet mixture fractions, i.e. $Z^L = 0.11, 0.10, 0.91, 0.82$, and 0.73, while Z^R is changed according to $Z^L + Z^R = 2Z_{st}$. Figure 4.10 shows the error of the FGM computation as a function of K_{st}. The crossing of the lines at low strain rates can be explained by the decrease in the growth of the error shown in figure. 4.8. Also the slower increase of the error for computations with higher values of $\tilde{\chi}_{st}$ can be subscribed to this phenomenon. Note that for higher strain rates and relatively low values of $\tilde{\chi}_{st}$, the error increases linearly with K_{st}.

4.3.4   Profiles of retrieved variables

In this section, temperature, density, and species profiles of the reduced computations are compared with corresponding profiles of detailed computations. The profiles are evaluated for flames with $Z^L = 2Z_{st}$ and $Z^R = 0$. Note that in this con-
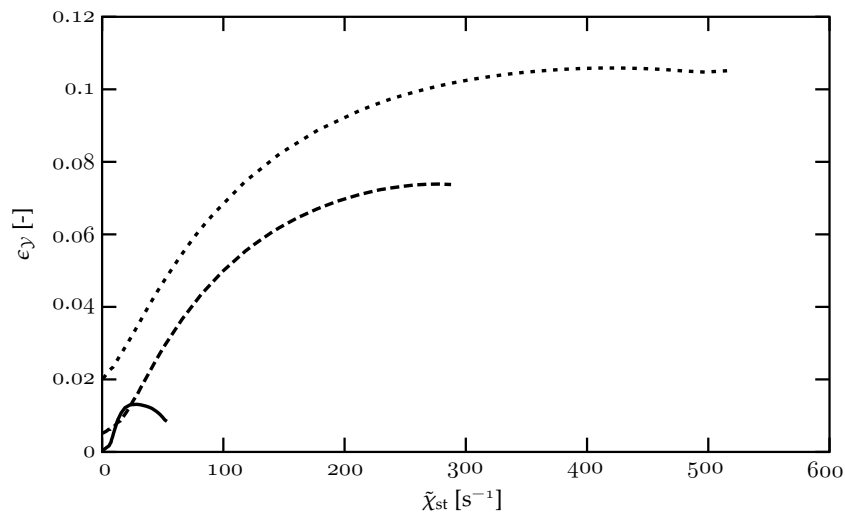
Figure 4.8 : The error as a function of $\tilde{\chi}_{st}$ at three different strain rates: $a = 100 \text{ s}^{-1}$ (solid line), $a = 550 \text{ s}^{-1}$ (long dashes), and $a = 1000 \text{ s}^{-1}$ (short dashes).

(a)   (b)
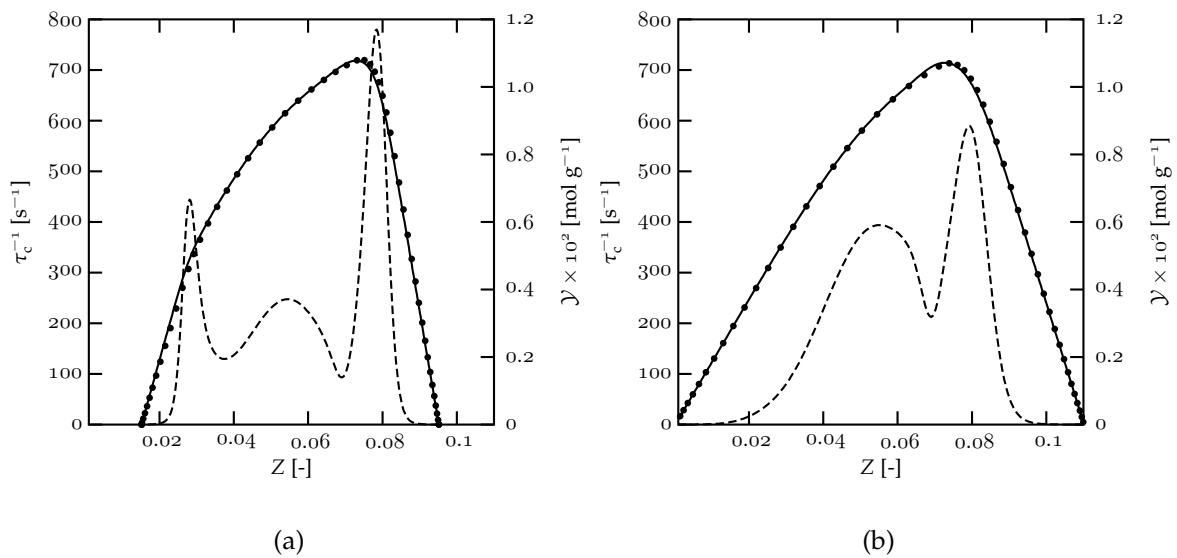
Figure 4.9 : The profiles of the controlling variable $\mathcal{Y}$ and the chemical time scale τ as a function of Z at a strain of 100 s^{-1}. The left figure has the inlet mixture fractions $Z^L = 0.095$ and $Z^R = 0.015$, whereas the right figure has the inlet mixture fractions $Z^L = 0.11$ and $Z^R = 0.0$. The solid lines represent the detailed solutions and symbols the FGM solutions of $\mathcal{Y}$. The dashed lines represent τ_c^{-1} of the detailed solutions.
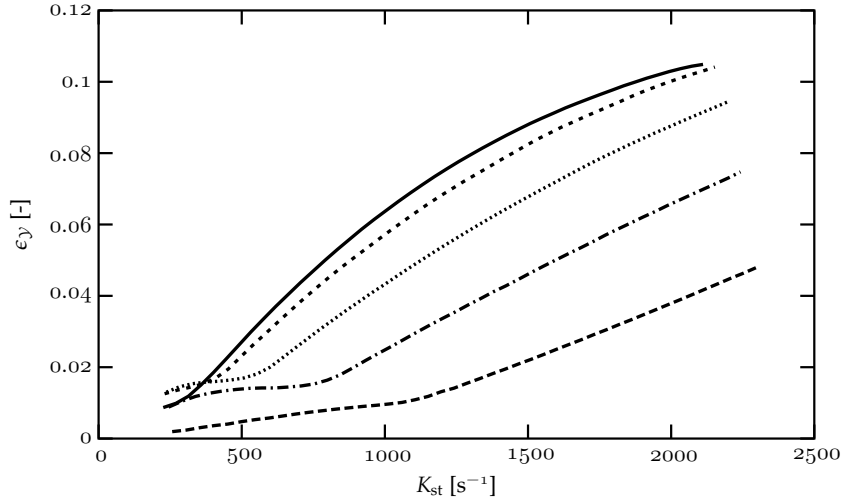
Figure 4.10 : The figure shows the error as a function of K_{st} for five different inlet composi-
tions varying between: $Z^L = 2Z_{st}$ and $Z^R = 0$ (solid line), $Z^L = 0.07267$ and
$Z^R = 0.03767$ (long dashes).

figuration two instead of three flame fronts appear: a rich premixed flame front and
a non-premixed flame front, in which remaining CO and H_2 react with the oxidiser
from the right-hand side. The figures 4.11, 4.12 and 4.13 show profiles for $a = 100$
s^{-1} (left figures) and $a = 1000$ s^{-1} (right figures), respectively.

Firstly, the density and temperature profiles are evaluated. The density plays an
important role in the prediction of the mixture fraction profile. An inaccurate pre-
diction of the Z-profile will lead to large errors in the spatial domain in the profiles
of the other dependent variables. Figure 4.11a shows that the density and temper-
ature profiles are accurately predicted by FGM for the flame with $a = 100$ s^{-1}. On
the other hand, for the flame with $a = 1000$ s^{-1}, which is shown in 4.11b, the FGM
profile significantly deviates from the detailed solution (errors up to 10%). In both
figures, the largest errors are found at the left-hand side of the domain, i.e. in the
rich premixed flame structure. The error in the diffusion flame, at the right-hand
side of the domain is much smaller. This result is in correspondence with the results
shown in figure 4.9.

Furthermore, it can be concluded that the extrapolation outside the flammability
limits of the FGM leads to an accurate prediction of the temperature and density
profiles. In the flames studied in this section, extrapolation is needed only at the
lean side of the flame, i.e. the right-hand side of the flame, where $Z < 0.022$. The
accuracy of the extrapolation is e.g. shown in figures 4.11a and b. In these figures,
an extrapolation is used at the right hand side, where $T \lesssim 1100$ K.

Figure 4.12 shows profiles of O_2, H_2O, and H_2. Especially, the profiles of O_2
and H_2O are predicted accurately for $a = 100$ s^{-1}. The error of the H_2 error is
somewhat larger. For $a = 1000$ s^{-1}, also the errors in the profiles of O_2 and H_2O are
larger. Figure 4.11b also shows that O_2 is not fully consumed by the rich premixed
flame at the left hand side. Due to the high strain rate, the premixed flame and

(a) (b)

Figure 4.11 : Density and temperature profiles for a counterflow flame with $Z^L = 2Z_{st}$, $Z^R = 0$, $a = 100$ s^{-1} (left figure), and $a = 1000$ s^{-1} (right figure). Temperature T (detailed: solid lines, reduced: crosses), and density ρ (detailed: short dashed lines, reduced: solid circles).

the non-premixed flame (at the left-hand side) are pressed against each other, as already shown in figure 4.7. Diffusion of radicals from one flame front into the other leads to additional inaccuracies from one-dimensional premixed behaviour. This phenomenon was already observed for counterflow premixed flames [70].

Finally, profiles of the H-radical and CH_3OH (methanol) are shown in figure 4.13, because these are often very hard to predict using reduction techniques like ILDM. Even though the error in the profiles of the temperature, density, and the major species is relatively small, the errors in intermediate species is significantly larger. Especially in the flame with $a = 100$ s^{-1}, this difference is significant. This phenomenon is probably caused by by the high sensitivity of intermediates to small changes in the species concentrations and temperature.

4.3.5 Brief summary of the results

In general, it can be concluded that the important features of the one-dimensional counterflow flames, which are partially-premixed, are reproduced with the FGM method. However, a number of deviations from the detailed results are observed. The main results that are presented in this section can be summarised in a few points:

1. Flow straining has only little effect on the chemistry. However, at higher strain rates, merging of the flame fronts may lead to errors.

2. Mixing processes, which are caused by a gradient in the mixture fraction Z lead to errors especially in the premixed flame fronts. The largest errors are

(a)   (b)

Figure 4.12 : Species profiles for a counterflow flame with $Z^L = 2Z_{st}$, $Z^R = 0$, $a = 100$ s^{-1} (left figure), and $a = 1000$ s^{-1} (right figure). ϕ_{O_2} (detailed: solid lines, reduced: crosses), ϕ_{H_2O} (detailed: long dashed lines, reduced: open circles), and ϕ_{H_2} (detailed: short dashed lines, reduced: solid circles).

(a)   (b)

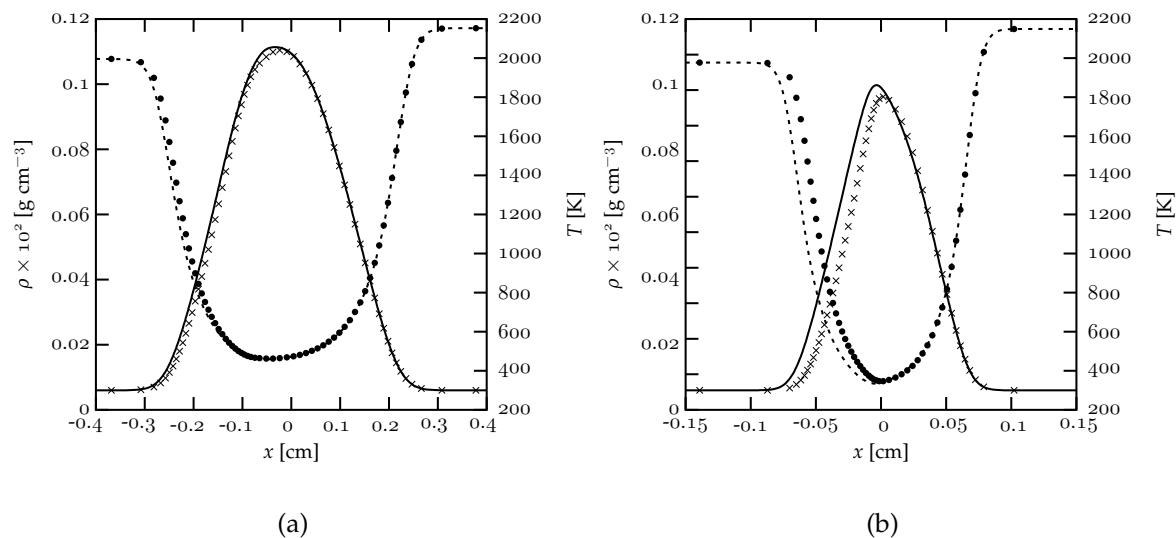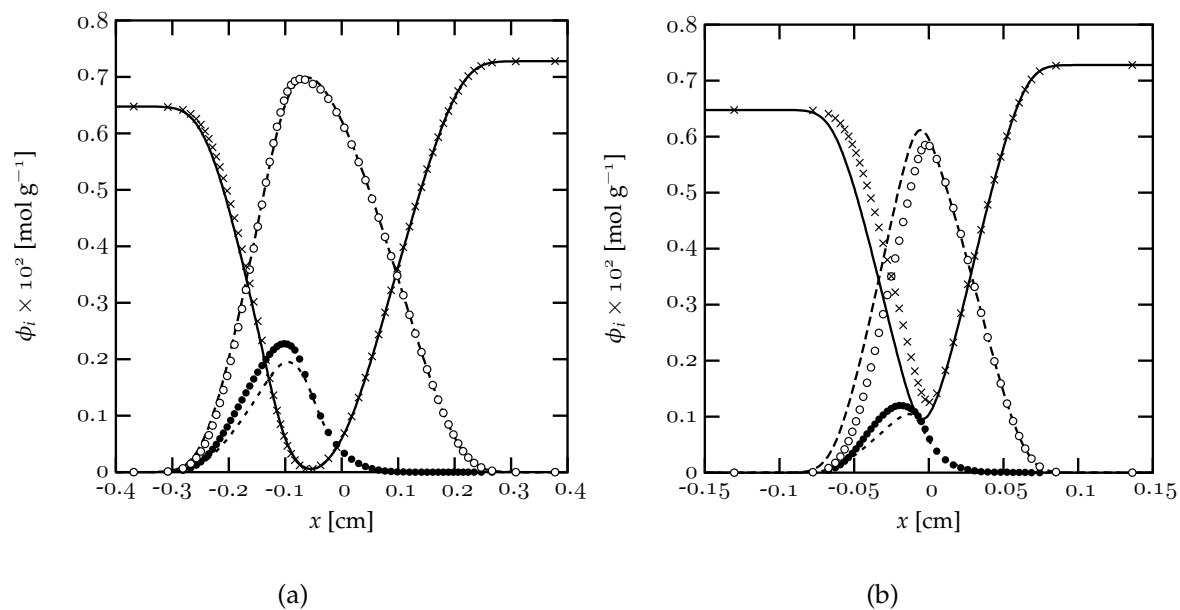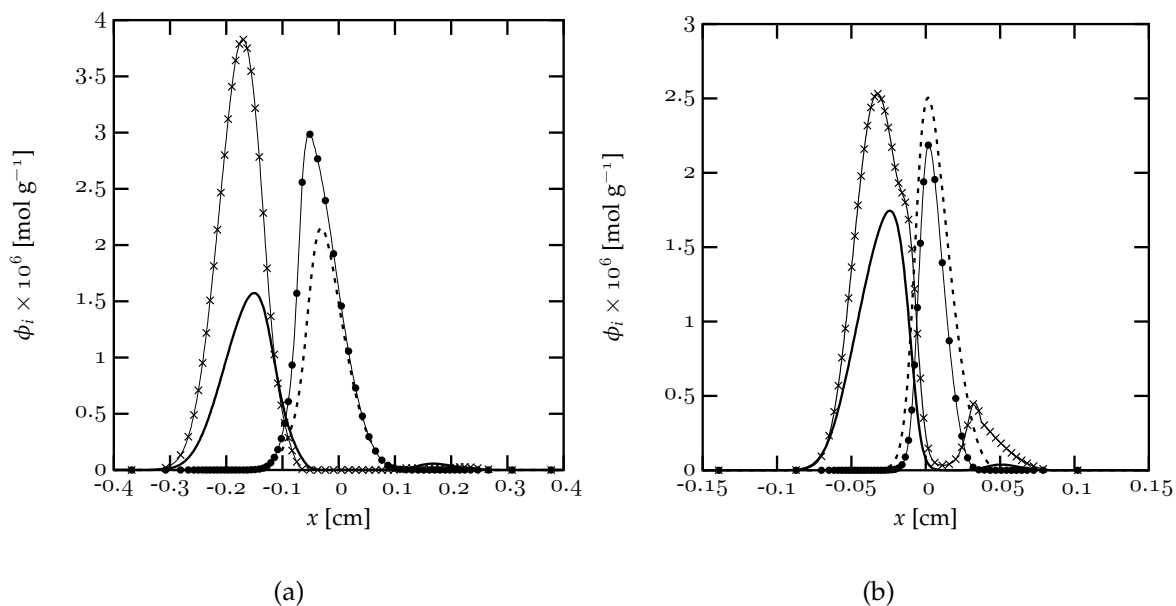**Figure 4.13** : Species profiles for a counterflow flame with $Z^L = 2Z_{st}$, $Z^R = 0$, $a = 100$ s^{-1} (left figure), and $a = 1000$ s^{-1} (right figure). $\phi_H/100$ (detailed: short dashed lines, reduced: thin solid line and solid circles) and ϕ_{CH_3OH} (detailed: solid lines, reduced: thin solid line and crosses).

Table 4.1: The order of the error ϵ_y of the FGM computation (in %) as a function of τ_{FGM}/τ_f and τ_{FGM}/τ_m. Note that the error can not be given for all combinations of τ_{FGM}/τ_f and τ_{FGM}/τ_m, because data is not available for all combinations.

	τ_{FGM}/τ_f [-]				
τ_{FGM}/τ_m [-]	0.5	1.0	1.5	2.0	2.5
0.1	2.4	3.9	4.7	5.5	6.5
0.2	-	5.6	7.3	8.3	9.3
0.3	-	-	8.2	9.3	10.4
0.4	-	-	-	9.8	10.5
0.5	-	-	-	-	10.5

found in the rich premixed flame structure.

3. The profiles of major species and temperature are predicted accurately, especially if the gradients in Z are small. On the other hand, the errors in the radical profiles are larger.

4.4 Analysis of the FGM results

In the previous section, results showed that the largest errors of the reduced computations with FGM were found in the premixed flame structures, instead of the non-premixed flame structures. At first, this seems rather strange, because the FGM is based on the solutions of premixed flames. However, this can be clarified by a comparison of time scales of the different processes in the flame with the general time scale of the FGM flamelets. The flow and mixing time scale of the counterflow flame, and a general time scale of the FGM database can be defined as

$$\tau_f = K_{st}^{-1}, \quad \tau_m = \tilde{\chi}_{st}^{-1}, \quad \text{and} \quad \tau_{FGM} = \frac{\delta_{f,st}}{s_{L,st}}, \tag{4.11}$$

respectively. In τ_{FGM}, $\delta_{f,st}$ and $s_{L,st}$ are the flame thickness and the laminar burning velocity of the stoichiometric flamelet, respectively. The burning velocity of the stoichiometric flamelet is $s_{L,st} \approx 28$ cm/s and the flame thickness is $\delta_{f,st} \approx 0.3$ mm, so the FGM time scale yields $\tau_{FGM} \approx 1.1 \times 10^{-3}$ s.

In Table 4.1, the error ϵ_y is shown as a function of τ_{FGM}/τ_f and τ_{FGM}/τ_m. Note that the errors are somewhat over-predicted, because ϵ_y is based on the whole flame structure, while the purpose of FGM is to model the chemical processes accurately, which are non-zero in only a part of the flame. In general, it is observed that FGM leads to a small error of a few percent when flow and mixing time scales are larger than the FGM time scale and this error still remains relatively small (≈ 10 %) for faster mixing and flow processes. Especially straining of the flow has only a small
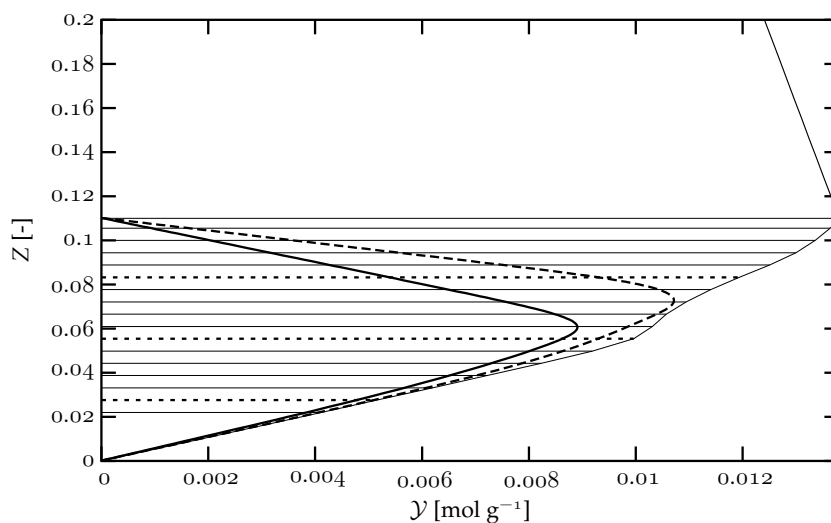
Figure 4.14 : The flame trajectories of two counterflow flames with $Z_L = 2Z_{st}$ and $Z_R = 0$ at different strain rates (thick solid line: $a = 1000 \text{ s}^{-1}$, thick dashed line: $a = 100$ s^{-1}). The thin lines represent the flamelets from the FGM database, and the dotted lines represent the flamelets with $Z = 0.5Z_{st}$, $Z = Z_{st}$, and $Z = 1.5Z_{st}$, respectively.

effect on the accuracy. However, at high strain rates, the flame fronts are pressed against each other, which leads to additional inaccuracies. It is more appropriate to compare the physical time scales (i.e. τ_m and τ_f) with chemical time scales inside the counterflow flame. The analysis in this section is separated in two parts. Firstly, the accuracy of the non-premixed part is analysed. Secondly, the time scales in the premixed structures are evaluated.

4.4.1 Analysis of the non-premixed flame structure

In figure 4.14, two $(Z, \mathcal{Y})$-trajectories are shown for flames with $a = 100 \text{ s}^{-1}$ and $a = 1000 \text{ s}^{-1}$, respectively. In both flames, the boundary mixture fractions are given by $Z^L = 2Z_{st}$ and $Z^R = 0$. In the figure, also a number of premixed flamelets from the FGM are shown. The three dashed FGM flamelets correspond to flamelets with $Z = 1.5Z_{st}$, $Z = Z_{st}$, and $Z = 0.5Z_{st}$. In addition, the thin solid line, which connects the premixed flamelets on the right-hand side represents the chemical equilibrium solutions. In this figure, it can be observed that the values of $\mathcal{Y}$ in the non-premixed flame (around $Z = Z_{st}$) are relatively close to the local chemical equilibrium values, even for flames with a high strain rate. Close to chemical equilibrium, chemical processes are much faster than other processes in the flame. In addition, the chemical processes can be accurately described by a two-dimensional FGM, with Z and $\mathcal{Y}$ as controlling variables. This was also shown for example in figure 3.10, where a one-dimensional FGM is compared with a one-dimensional ILDM and a homogeneous solution of a H_2/air mixture. Close to chemical equilibrium, all solutions are equal, which implies that the behaviour is dominated by chemical processes. In addition,

(a)   (b)
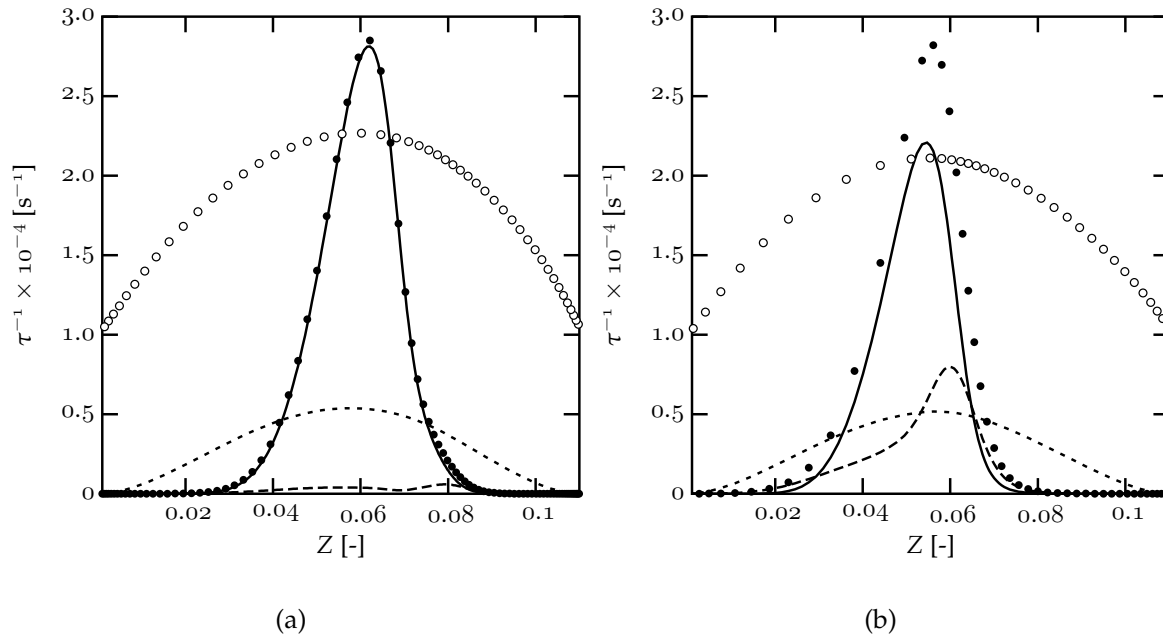
Figure 4.15 : The (inverse of the) time scales in a counterflow flame with $a = 100$ s^{-1} (left figure) and $a = 1000$ s^{-1} (right figure), $Z^L = 2Z_{st}$, and $Z^R = 0$ (both figures: $1/\tau_c^-$ (solid line), $1/\tau_c^+$ (solid symbols), $1/\tau_c$ (long dashes). In the left figure: $1000 \times 1/\tau_m$ (short dashed line) and $1000 \times 1/\tau_f$ (open symbols) and in the right figure: $100 \times 1/\tau_m$ (short dashed line) and $100 \times 1/\tau_f$ (open symbols))

the behaviour can be described by a single reaction progress variable $\mathcal{Y}$.

By means of a time scale analysis of the chemical and physical processes in the flame, it can be shown that the non-premixed part of the flame is dominated by chemical processes. Figure 4.15 shows the inverse of chemical and physical time scales for the two flame trajectories shown in figure 4.14. Note that in the left figure, the mixing and flow time scale are multiplied by 1000, whereas these time scales are multiplied by 100 in the right figure. Close to equilibrium, the chemical production and consumption rates are very large, but the overall chemical rate is small. Since the chemical consumption and production time scales are very small compared to the flow and mixing time scale in figure 4.15a (note that the figure shows the inverse of the time scales), it can be concluded that the behaviour is mainly determined by chemistry around $Z = Z_{st}$. Furthermore, as the chemistry is close to equilibrium, it can be reproduced accurately by the FGM, so the error in the reduced computation is small. In figure 4.15b, the time scales are not so clearly separated as in figure 4.15a. However, in the region around $Z = Z_{st}$, the chemical production and consumption rate are much faster then the overall chemistry rate. Hence, the error in the non-premixed flame structure is still relatively small in the FGM computation (see e.g. figure 4.11b).

4.4.2   Analysis of the premixed flame structures

A significant part of the error in the reduced computations arises in the premixed parts of the partially-premixed counterflow flames. For example in figure 4.9, it was shown that the decrease of the error for increasing strain rate was mainly caused by the extinction of the lean premixed flame. Furthermore, in the species and temperature profiles shown in figures 4.11 and 4.12, the largest differences between the detailed and the FGM solution were observed in the rich premixed part of the flame. Apparently, the gradient in Z has quite some effect on the flame response. In figures 4.15a, the rich premixed flame front is located around $Z = 0.08$. In the figure, it can be observed that the chemical production and consumption rates are in the same order as the overall chemical rate at $Z = 0.08$. Furthermore, the overall chemical reaction rate is in the same order as the mixing scale.

As stated earlier in this section, especially close to chemical equilibrium, the chemical processes are much faster than other processes in the flame. On the other hand, in lower temperature regions, chemical and physical time scales are in the same order. Therefore, especially in the rich premixed flame structure, errors are expected, because in the rich branch, the compositions are further away from chemical equilibrium (see figures 4.15 and 4.14).

To show that the largest errors are obtained in the rich branch of the partially-premixed counterflow flames, the temperature profiles of premixed flamelets are compared with temperatures of the counterflow flames. Figure 4.16 shows the temperature T as a function of the progress variable $\mathcal{Y}$ for three different premixed flamelets with $Z = 1.5Z_{st}$, $Z = Z_{st}$, and $Z = 0.5Z_{st}$ (lines) and the data obtained from the counterflow flames at the corresponding Z-values (symbols), with $Z^L = 2Z_{st}$, $Z^R = 0$, and $a \in [0, 1000]$. The figure clearly shows that the errors are larger and that compositions are further removed from chemical equilibrium at the rich branch.

4.5   Comparison with non-premixed flamelets

In this section, a non-premixed flamelet library is used to model partially-premixed counterflow flames. Not the complete analysis of the previous sections is repeated, only a few illustrative example are discussed. Figure 4.17 shows results of a detailed computation and reduced computations, obtained with a non-premixed flamelet database and a FGM, for a flame with $Z^L = 2Z_{st}$, $Z^R = 0$, and $a = 250 \text{ s}^{-1}$. The left figure shows profiles of the controlling variables Z and χ as a function of the spatial coordinate. Especially at the premixed part (at the left-hand side of the domain) the differences between the detailed computation and the solution obtained with the non-premixed database are large. The cause of the large error is clarified in the right figure, which shows the corresponding temperature profiles and the profiles of $\mathcal{Y}$ as a function of the mixture fraction. In the non-premixed flames, which are used to construct the database, the mixture fraction Z varies between 0 at the oxidiser side
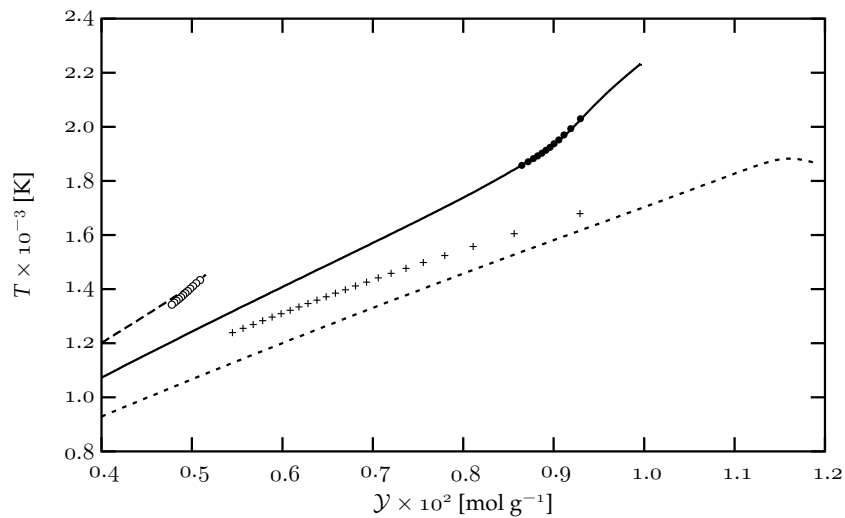
Figure 4.16 : The temperature obtained from counterflow flames, with $a \in [100, 1000]\ \mathrm{s}^{-1}$, $Z_L = 2Z_{st}$ and $Z_R = 0$, compared with the data obtained from the FGM, for three different values of Z. The lines represent premixed flamelets with $Z = 0.5Z_{st}$ (long dashes), $Z = Z_{st}$ (solid line), and $Z = 1.5Z_{st}$ (short dashes). The open symbols represent the data obtained from the counterflow flames, with $Z = 0.5Z_{st}$ (open circles), $Z = Z_{st}$ (solid circles) and $Z = 1.5Z_{st}$ (addition signs)

(a) (b)
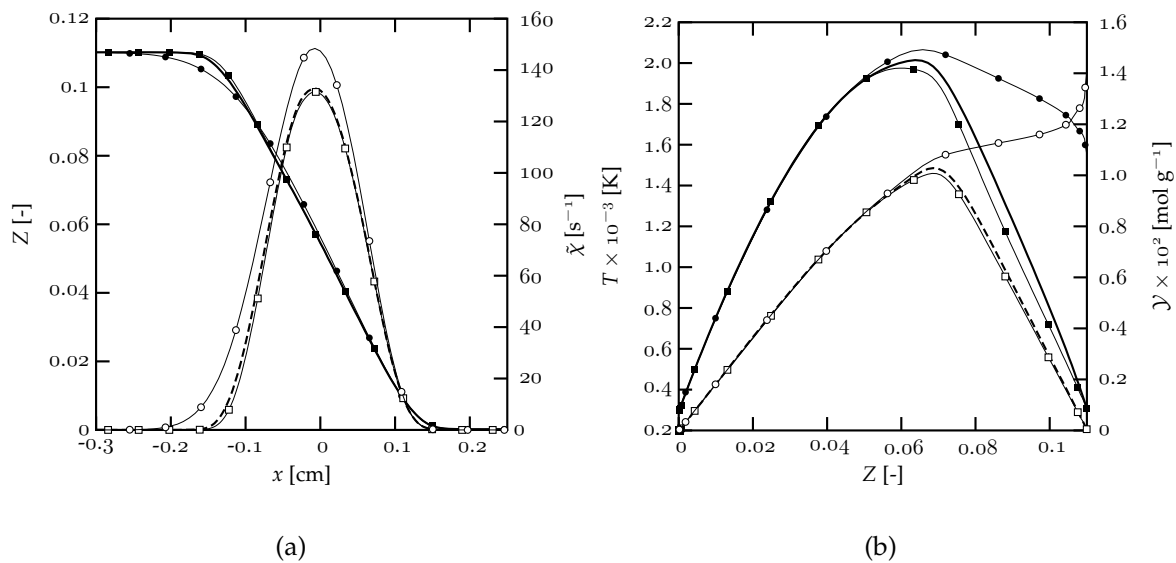
Figure 4.17 : Profiles of a partially-premixed counterflow flame with $Z^L = 2Z_{st}$, $Z^R = 0$, and $a = 250\ \mathrm{s}^{-1}$. The thick lines represent the detailed solutions, the thin lines with squares represent the FGM solution, and the thin dashed lines with circles represent the solution obtained with non-premixed flamelets. The left figure shows profiles of the controlling variables Z (detailed: solid line, reduced: closed symbols) and $\tilde{\chi}$ (detailed: dashed line, reduced: open symbols). The right figure shows profiles of the temperature T (detailed: solid line, reduced: closed symbols) and the temperature $\mathcal{Y}$ (detailed: dashed line, reduced: open symbols).
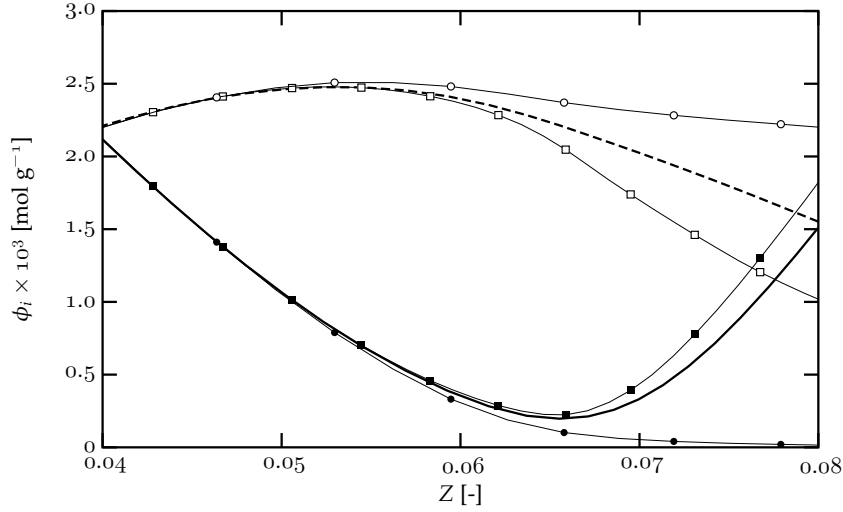
Figure 4.18 : Species profiles of ϕ_{O_2} (detailed: thick solid line, FGM: thin line with solid squares, and non-premixed flamelet solution: thin line with solid circles) and ϕ_{CO_2} (detailed: thick dashed line, FGM: thin line with open squares, and non-premixed flamelet solution: thin line with open circles). in a partially-premixed counterflow flame with $Z^L = 2Z_{st}$, $Z^R = 0$, and $a = 250\,\mathrm{s}^{-1}$.

and 1 at the fuel side. In the partially-premixed flame of figure 4.17, however, the boundaries are different. Hence, the corresponding variables, like e.g. T and $\mathcal{Y}$, at Z^L correspond to values inside the non-premixed flame front. The over-prediction of the temperature at the rich side leads to an incorrect density profile, which causes the large deviations in the $Z(x)$-profile. It can be concluded that it is not possible to reproduce the premixed flame structures in a partially-premixed flame with a database that is based on purely non-premixed flamelets (a similar behaviour would be observed at the lean side if $Z^R \neq 0$). The errors decrease if the values of Z^L and Z^R approach 1 and 0, respectively.

Since the flamelet database is based on non-premixed flamelets, it is interesting to investigate the non-premixed flame structure in the partially-premixed flame. Figure 4.18 shows profiles of ϕ_{O_2} and ϕ_{CO_2}. In the region where the non-premixed flame front is situated ($0.04 \lesssim Z \lesssim 0.07$), the difference between the detailed solutions and the reduced solution obtained with the non-premixed flamelets are in the same order as the difference between the detailed and the FGM solution. The inaccurate prediction of the premixed flame front also affects the accuracy of the profiles of the non-premixed flame front.

4.6 Discussion

In this chapter, the Flamelet-Generated Manifold method, which is based on the solution of premixed flames, is used to describe partially-premixed counterflow flames. In the tested flames, two parameters describe the deviation from the one-

dimensional premixed flame structure, i.e. the strain rate K and the scalar dissipation rate $\tilde{\chi}$. The flamelet equations (3.63-3.65) are derived, by assuming that the time and length scales of the processes along the iso-contours of $\mathcal{Y}$ are much larger than the scales of the processes perpendicular to the iso-surfaces. The results show that, as already observed in [70], even though the flow time scale τ_{f} is in the same order as the premixed flame time scale τ_{FGM}, the effect on the chemistry is relatively small. However at higher strain rates, the flame fronts merge, which leads to some inaccuracies.

As the solutions of premixed flames are used to construct the FGM, intuitively one would expect that the largest problems are found in the reproduction of the non-premixed flame structure. However in the non-premixed flame front, the temperatures are so high that the flame behaviour is mostly determined by chemistry. Since the chemical compositions are close to chemical equilibrium, they can accurately be described by the FGM. It should be noted that the maximum scalar dissipation rate $\tilde{\chi}_{\mathrm{st}}$ in this study was rather large: $\tilde{\chi}_{\mathrm{st}} = 517 \text{ s}^{-1}$. For comparison, the extinction dissipation rate of a fully non-premixed methane/air flame is $\tilde{\chi}_{\mathrm{st}} = 1162 \text{ s}^{-1}$ [11].

On the other hand, the largest difficulties are observed in the premixed flame fronts. Part of the difficulties are caused by the effect of the gradient in Z on the chemistry. For low values of $\tilde{\chi}_{\mathrm{st}}$, detailed temperature, density, and major species profiles are reproduced accurately, whereas the errors in the radical profiles are much larger. These errors are probably caused by the sensitivity of radicals to small deviations in the major species and temperature profiles. On the other hand, at higher values of the scalar dissipation rate, also the temperature, density, and major species profiles contain errors up to 10%. The largest deviations from the detailed solutions were obtained at the rich branch of the counterflow flame. In this part of the flame the species concentrations are further away from chemical equilibrium than at the lean branch.

The accuracy of the FGM computation could be enhanced by adding a third dimension to the manifold. By the inclusion of a second reacting controlling variable, additional chemical time scales are added to the manifold. Especially at the rich branch of the partially-premixed triple flame, the errors are caused by the fact that only one reacting progress variable was used. However, as the FGM manifolds are always based on the solution of premixed flames, the effect of mixing on the chemistry is still not taken into account in the manifold. Even though the inclusion of an extra controlling variable leads to additional degrees of freedom, in parts of the flame where both mixing and chemistry are important (especially the colder parts of the premixed flame structures) it will probably still be difficult to reproduce detailed profiles accurately.

In section 4.5, the FGM results are compared with results that are obtained with a non-premixed database. The results show that it is not possible to reproduce information of the premixed flame fronts in a laminar partially-premixed flame. In [14], a non-premixed flamelet database was used to model triple flames and the results

show a rich and a lean premixed flame front, and a non-premixed flame in the tail. However, in that case, the premixed flame front was modelled with the $\mathcal{G}$-equation approach in combination with a non-premixed database, in a turbulent environment. In that case, the species and temperature profiles in the premixed flame front are determined by the turbulence and do not correspond to profiles of a laminar premixed flamelet. Furthermore, the results in this chapter also show that the errors in the non-premixed part were in the same order as the errors in the results obtained with FGM.

The counterflow triple flame is a simple and effective test case to evaluate the applicability of FGM in partially-premixed systems, although it does not account for all effects in practical systems. For instance, diffusion along the iso-contours of $\mathcal{Y}$ is not present, because the contours of $\mathcal{Y}$ and Z are parallel. On the other hand, it is the gradient in Z that causes the main deviation from the premixed flame structure. In addition, all Lewis numbers were assumed to be equal to one, so higher order effects caused by preferential diffusion have not been taken into account yet. However, the results show that even though mixing times are in the same order as time scales of the FGM database, it is still possible to simulate the processes accurately. Therefore, it is reasonable to expect that preferential diffusion will not significantly influence the accuracy.

To conclude, the FGM method is a suitable method to model partially-premixed flames efficiently and accurately. With only two controlling variables, i.e. the mixture fraction Z and a reaction progress variable $\mathcal{Y}$, accurate results are obtained for the major species, temperature, and density, which is not expected for standard reduction techniques. On the other hand, errors in the radical profiles are significantly larger. Especially, the premixed part of the partially-premixed system is difficult to reproduce accurately if the gradients in Z become large. In that case, mixing time scales and chemical time scales are of the same order in the premixed parts of the partially-premixed flame. The non-premixed part of the flame is modelled accurately, because the chemistry in the diffusion part of the partially-premixed flames is close to chemical equilibrium, where the ILDM and FGM manifolds are nearly identical.

Phase Space ILDM

In section 3.5, a number of advantages and disadvantages of the ILDM and FGM method was listed. These disadvantages and advantages can be summarised in two categories. Firstly, as diffusion processes are not included in an ILDM, the ILDM method may lead to inaccuracies during the application of the manifold. Secondly, the mathematical background of the FGM method is less strong than in the ILDM method. Therefore, it is not trivial to extend the FGM to more dimensions. In this chapter, a new method is proposed, which can be regarded as a combination of the ILDM method and the FGM method: it combines the mathematical procedure of the ILDM method with the equations that are used to construct an FGM. This new method will be referred to as the Phase Space ILDM (PS-ILDM) method. Firstly, an introduction to the general idea of PS-ILDM is given. Secondly, the equations that are used for the construction of a PS-ILDM are derived. In the subsequent sections 5.3 and 5.4, the PS-ILDM method is illustrated with simple but illustrative examples. In sections 5.5 and 5.6, the PS-ILDM method is applied to a hydrogen/air-mechanism and syngas/air-mechanism, respectively. Finally in section 5.7, the PS-ILDM method is evaluated.

5.1   Introduction

The FGM method has proven to be an efficient method to compute premixed and partially-premixed flames. As already suggested in section 4.6, the accuracy of the method can be enhanced by increasing the dimension of the manifold. In this manner, more time scales are captured in the manifold. As stated in chapter 3, the extension of the manifold to more dimensions is not straightforward in the FGM method. In [70], a second dimension was added to the FGM by changing the inlet composition, while keeping the enthalpy and the element mass fractions constant. It requires experience of the user to define how the inlet mixture should be changed. For comparison, the ILDM method is based on a time scale analysis, to ensure that the slowest time scales are taken into account. All fast processes are assumed in steady-state. To capture more time scales, a higher dimensional ILDM can be constructed by relaxing one or more steady-state relations. However, the ILDM method may be inaccurate, because diffusion is not taken into account during the construction of the database.

The PS-ILDM method can be seen as a combination of the ILDM method and the FGM method. To include information about diffusion processes in the manifold, a PS-ILDM is based on the flamelet equations (3.63)-(3.65), which are used to construct a FGM. However, instead of directly solving the flamelet equations, the ILDM strategy is used to decouple the fast and slow processes. The purpose of the PS-ILDM method is twofold. Firstly, the possibility of developing a mathematical reduction technique, which includes transport processes is investigated. Secondly, the PS-ILDM method can be seen as a theoretical test case for the FGM method. Since a time scale analysis is not performed during the construction of a FGM, it is uncertain whether the manifold is attractive. In other words, it is unknown if small perturbations from the manifold are attracted back to the manifold rapidly. In the PS-ILDM method, a time scale analysis of the flamelet equations is performed. To be able to do a time scale analysis, which is analogous to the ILDM method, the set of flamelet equations, which are second-order ODEs, is rewritten into a set of first-order ODEs. The set of first-order equations describes processes in the so-called combustion phase-space $\mathcal{P}$. In this operation, the size of the system, i.e. the number of equations, is enlarged with a factor of two compared to the ILDM method. Hence, also the number of eigenvalues is twice as large. An illustration of a combustion process in the combustion phase space is given in section 5.2.2.

In section 3.3.1, it was discussed how the eigenvalues of the Jacobi matrix **J** are used to decouple the fast and slow processes in the ILDM method. In the PS-ILDM method, a similar procedure is followed. Generally, the eigenvalues of the ILDM system reappear in pairs of positive and negative eigenvalues. In the original ILDM method, the processes only depend on the time t. Therefore, positive eigenvalues are associated with growing modes, so these eigenvalues may not be assumed in steady-state (see figure 3.6). On the other hand in the FGM method, hence also in the PS-ILDM method, the processes are described in the spatial domain. The positive eigenvalues may correspond to damping modes in the direction of -s (upstream), so in that case they may be assumed in steady-state. Diffusion processes proceed in the positive and negative s-direction, called the s^+-direction and the s^--direction in the following. In figure 5.1, a schematic example is given of the solution of a convection-diffusion-reaction problem, which is one-dimensional. In this example, it is assumed that a source of Y_i is located at $s = s_0$. Due to diffusion, Y_i is transported in the s^+ and the s^--direction. The processes in the s^+-direction are dominated by the negative eigenvalue λ^-, like $\exp(\lambda^+ s)$, whereas the processes in the s^--direction are dominated by the positive eigenvalue λ^+, like $\exp(\lambda^+ s)$. A more detailed description of the eigenvalue spectrum is given in sections 5.2 and 5.3. A PS-ILDM is a manifold, which describes the slowest processes accurately, both upstream and downstream. All fast processes are assumed in steady-state. Note that on the manifold, one is interested in the correlation between the chemical components. It is insignificant whether the processes on the manifold are parameterised by time t or position s. The procedure to compute a manifold is similar to the ILDM method, with the difference
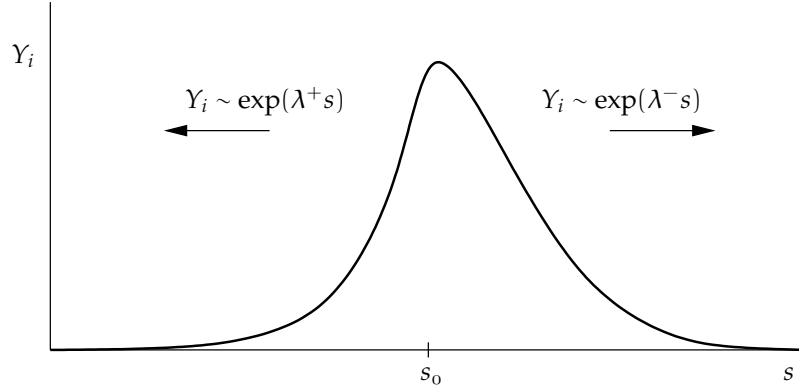
Figure 5.1 : A schematic example of a typical diffusion process. This can be, e.g. a station-
ary solution of a convection-diffusion-reaction problem, with a source at $s = s_0$.
Processes in the direction of s^- are dominated by λ^+, whereas processes in the
direction of s^+ are dominated by λ^-.

that processes that proceed in space are taken into account. A complete description
of the PS-ILDM procedure is given in the next section.

The application of a PS-ILDM is similar to the application of a FGM and a ILDM.
The manifold is parameterised by controlling variables and stored in a database.
During a CFD application, equations are solved for the controlling variables and
the other variables are retrieved from the database.

5.2   Phase Space ILDM theory

In this section, the PS-ILDM algorithm is discussed. The derivation is started with
the quasi one-dimensional equations for species and enthalpy that are used to con-
struct an FGM, i.e. equation (3.64)-(3.65). To be able to compare the flamelet equa-
tions with the ILDM equations, the flamelet equations are written in terms of specific
mole numbers. In that case, the species equations become

$$m\frac{d\phi_i}{ds} - \frac{d}{ds}\left(\frac{\lambda'}{c_p Le_i}\frac{d\phi_i}{ds}\right) = \omega_i, \qquad i \in [1, N_s - 1], \tag{5.1}$$

$$\sum_{i=1}^{N_s} M_i\phi_i = 1. \tag{5.2}$$

Note that the mass burning rate m is constant, since it is assumed that the premixed
flame is flat, i.e. $K = Q_i = Q_h = 0$ and $\sigma = 1$. With this assumption, the enthalpy
equation can be written as

$$m\frac{dh}{ds} - \frac{d}{ds}\left(\frac{\lambda'}{c_p}\frac{dh}{ds}\right) = \frac{d}{ds}\left(\frac{\lambda'}{c_p}\sum_{i=1}^{N_s-1} M_i h_i^*\left(\frac{1}{Le_i} - 1\right)\frac{d\phi_i}{ds}\right). \tag{5.3}$$

In the remainder of this section, the PS-ILDM method is derived in a number of
steps. In sections 5.3 and 5.4, the basic ideas of the method are illustrated with sim-

ple analytical examples. To be able to use the ILDM algorithm, the second-order differential equations are transformed into a system of first-order differential equations, which has twice the dimension of the original system. The new set of equations describes the combustion process in the composition phase space. To identify the low-dimensional manifold in the phase space, the ILDM algorithm is applied to this system of first-order equations.

5.2.1 Transformation into a system of first-order equations

To transform the FGM equations into a set of first order equations, the diffusive flux terms of species i and the enthalpy h are introduced according to

$$\psi_i = \frac{\lambda'}{c_p Le_i} \frac{d\phi_i}{ds}, \qquad i \in [1, N_s - 1], \tag{5.4}$$

and

$$\psi_h = \frac{\lambda'}{c_p} \frac{dh}{ds} + \frac{\lambda'}{c_p} \sum_{i=1}^{N_s-1} h_i^* M_i \left(\frac{1}{Le_i} - 1 \right) \frac{d\phi_i}{ds}, \tag{5.5}$$

respectively. As the Lewis numbers are only defined for $i \in [1, N_s - 1]$, the set of equations for the species fluxes is completed with

$$\sum_{i=1}^{N_s} M_i \psi_i = 0. \tag{5.6}$$

Together with the expressions for the diffusive fluxes and after reorganising, the flamelet equations (5.1) and (5.3) can be written as

$$mLe_i \frac{c_p}{\lambda'} \psi_i - \frac{d\psi_i}{ds} = \omega_i, \qquad i \in [1, N_s - 1], \tag{5.7}$$

$$m \frac{c_p}{\lambda'} \psi_h - \frac{d\psi_h}{ds} = m \frac{c_p}{\lambda'} \sum_{i=1}^{N_s-1} M_i h_i^* (1 - Le_i) \psi_i. \tag{5.8}$$

Equations (5.2), and (5.4)-(5.8) describe the combustion process in the so-called composition phase-space, which is $2(N_s + 1)$-dimensional. Combination of equations (5.4) and (5.7) leads to a set of first-order differential equations,

$$\frac{d\phi_i}{ds} = Le_i \frac{c_p}{\lambda'} \psi_i, \qquad i \in [1, N_s - 1], \tag{5.9}$$

$$\frac{d\psi_i}{ds} = mLe_i \frac{c_p}{\lambda'} \psi_i - \omega_i, \qquad i \in [1, N_s - 1]. \tag{5.10}$$

Furthermore, the constraints (5.2) and (5.6) can be written as

$$\frac{d\phi_{N_s}}{ds} = -\sum_{i=1}^{N_s-1} \frac{M_i}{M_{N_s}} Le_i \frac{c_p}{\lambda'} \psi_i, \tag{5.11}$$

$$\frac{d\psi_{N_s}}{ds} = -m \sum_{i=1}^{N_s-1} \frac{M_i}{M_{N_s}} Le_i \frac{c_p}{\lambda'} \psi_i - \omega_{N_s}. \tag{5.12}$$

Due to preferential diffusion effects, the enthalpy is not necessarily constant in a flame. Therefore, also enthalpy variations must be taken into account in the PS-ILDM method. Note that the system of ILDM equations (3.32) was derived for constant enthalpy. For the enthalpy equation a similar set of equations can be derived,

$$\frac{\mathrm{d}h}{\mathrm{d}s} = \frac{c_p}{\lambda'}\psi_h + \frac{c_p}{\lambda'}\sum_{i=1}^{N_s-1} M_i h_i^* \left(Le_i - 1\right)\psi_i, \tag{5.13}$$

$$\frac{\mathrm{d}\psi_h}{\mathrm{d}s} = m\frac{c_p}{\lambda'}\psi_h + m\frac{c_p}{\lambda'}\sum_{i=1}^{N_s-1} M_i h_i^* \left(Le_i - 1\right)\psi_i. \tag{5.14}$$

The complete system of equations can be written as

$$\frac{\mathrm{d}\boldsymbol{\Theta}}{\mathrm{d}s} = \boldsymbol{\Omega}(\boldsymbol{\Theta}) \tag{5.15}$$

where the vector $\boldsymbol{\Theta} = (\phi_1, \ldots, \phi_{N_s}, h, \psi_1, \ldots, \psi_{N_s}, \psi_h)^{\mathrm{T}}$ is a vector in the $N_{\mathrm{ph}} = 2(N_s + 1)$-dimensional composition phase space and $\boldsymbol{\Omega}(\boldsymbol{\Theta})$ is a vector that contains the source terms presented in equations (5.9)-(5.14). Note that the form of this equation is identical to the form of equation (3.5), which was the starting point of the ILDM algorithm. In equation (5.15), the derivative is a spatial derivative instead of a time derivative. The description of the processes as a function of the spatial coordinate s has a number of consequences for the steady-state assumptions, which will be discussed later in this section. As the pressure is constant in the flames studied in this thesis, the pressure is not included in the vector $\boldsymbol{\Theta}$.

5.2.2 An example of combustion in the phase space

Like the state space $\mathcal{S}$, the composition phase space $\mathcal{P}$ is multi-dimensional. Therefore, it is relatively difficult to visualise a combustion process in the phase-space. To illustrate the behaviour of combustion processes in the phase-space, this section presents a number hydrogen/air flame trajectories in the phase space. The trajectories show the typical chemical and diffusive behaviour of the flames, which forms the basis for the development of the PS-ILDM method. Figure 5.2a and b show trajectories of a number of hydrogen/air flames projected on the (ϕ_{H_2O}, ϕ_H)-plane and the (ϕ_{H_2O}, ψ_H)-plane, respectively. The thick solid line represents a stoichiometric flame at atmospheric conditions, with an initial temperature of 300 K. The other lines represent trajectories of flames with different inlet compositions. The inlet compositions are modified by replacing part of the hydrogen and oxygen by water, in such a manner that the element fractions of H and O remain unchanged. The initial temperature is modified such that the equilibrium state equals the equilibrium state of the stoichiometric flame.

Even though not all dimensions are shown, it can be observed in the figures that the trajectories converge towards a lower-dimensional manifold in the compo-

(a)   (b)
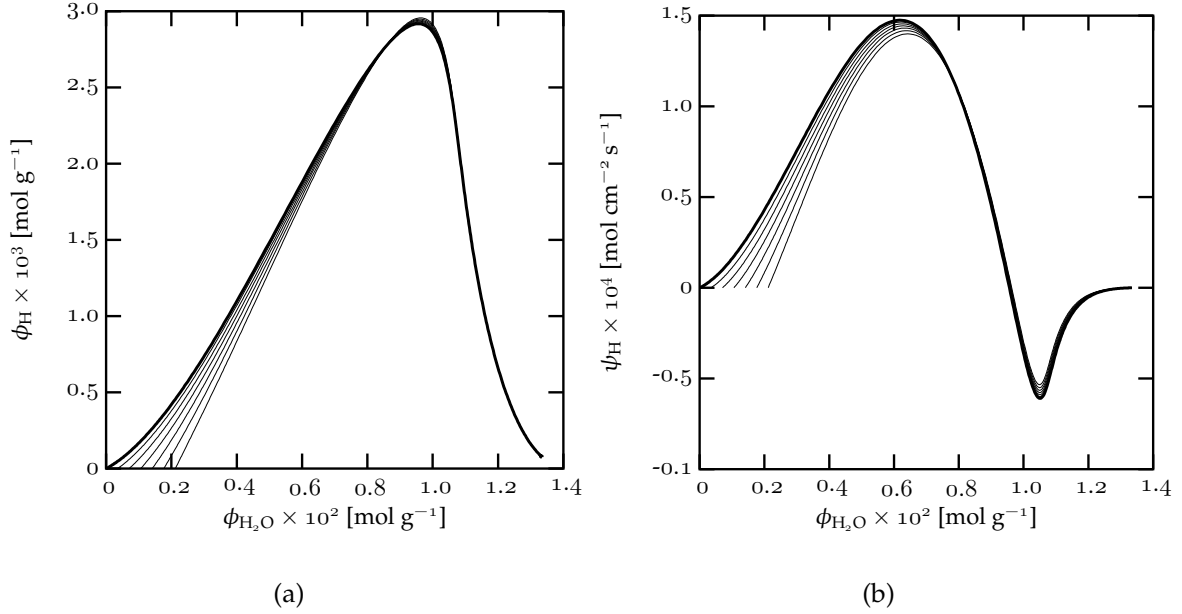
Figure 5.2 : An example of profiles in the combustion phase space $\mathcal{P}$, as a function of various inlet compositions. The left and right figure show profiles projected on the (ϕ_{H_2O}, ϕ_H)-plane and the (ϕ_{H_2O}, ψ_H)-plane, respectively. The thick solid line represents the solution of the stoichiometric H_2/air flame.

sition phase space. The purpose of the PS-ILDM method is to identify this low-dimensional manifold by means of a time scale analysis, which is similar to the time scale analysis of the ILDM method. This time scale analysis is treated in the next section.

5.2.3   Time scale analysis of Ω

Analogous to the ILDM method, a time scale analysis is applied to source term $\Omega(\boldsymbol{\Theta})$. After linearising the source term $\Omega(\boldsymbol{\Theta})$ around a reference composition $\boldsymbol{\Theta}^0$, the evolution of $\boldsymbol{\Theta}(s)$ is described by

$$\frac{d\boldsymbol{\Theta}}{ds} \approx \Omega(\boldsymbol{\Theta}^0) + \mathbf{A}(\boldsymbol{\Theta} - \boldsymbol{\Theta}^0), \tag{5.16}$$

where the Jacobi matrix $\mathbf{A}$ is introduced according to

$$\mathbf{A} = \begin{pmatrix} \mathbf{O} & \mathbf{L} \\ -m\mathbf{J}^* & m\mathbf{L} \end{pmatrix}. \tag{5.17}$$

The structure of the matrix $\mathbf{L}$ is given in Appendix C. The matrix $\mathbf{J}^*$ is a scaled sub-matrix of the Jacobi matrix $\mathbf{J}$, which appeared in equation (3.29) in the derivation of the ILDM method. The Jacobi matrix $\mathbf{J}$ is $(N_{st} \times N_{st})$-dimensional, with $N_{st} = N_s + 2$. As the pressure is not taken into account in the derivation of the PS-ILDM method,

the $(N_{\text{ph}}/2 \times N_{\text{ph}}/2)$-matrix $\mathbf{J}^*$ is given by $J_{ij}^* = J_{ij}\,\rho/m$, with $i, j \in [1, N_{\text{ph}}/2]$. In the FGM method, the parameter m represents the mass burning rate. In a general flame, m can be seen as the mass flow locally perpendicular to the iso-contours of the controlling variable $\mathcal{Y}$. In the PS-ILDM method, the parameter m is an indication for the ratio between diffusion and chemical processes. In contrast to the FGM method, this parameter can be chosen independently, so it adds an extra dimension to the manifold. The usage of m as an additional controlling variable will be discussed in section 5.2.4.

After introducing $\vartheta(s)$ as the difference between $\boldsymbol{\Theta}(s)$ and the reference state $\boldsymbol{\Theta}^0(s)$, the following expression can be obtained

$$\frac{\mathrm{d}\vartheta}{\mathrm{d}s} = \mathbf{A}\vartheta. \tag{5.18}$$

Similar to the ILDM method, it is assumed that the Jacobi-matrix $\mathbf{A}$ can be diagonalised

$$\frac{\mathrm{d}\vartheta}{\mathrm{d}s} = \mathbf{U_A}\boldsymbol{\Lambda_A}\mathbf{U_A}^{-1}\vartheta, \tag{5.19}$$

with $\boldsymbol{\Lambda_A}$ a matrix which contains the eigenvalues $\lambda_i^{\mathbf{A}}$, for $i \in [1, N_{\text{ph}}]$. Similar to the ILDM method, the columns of the matrix $\mathbf{U_A}$ are the right eigenvectors $\boldsymbol{u}_i^{\mathbf{A}}$ of matrix $\mathbf{A}$ with $i \in [1, N_{\text{ph}}]$. In addition, the left eigenvectors $\boldsymbol{v}_i^{\mathbf{A}}$ of $\mathbf{A}$ with $i \in [1, N_{\text{ph}}]$, are given by the rows of $\mathbf{U_A}^{-1}$. Using the transformation $\vartheta = \mathbf{U_A}\widehat{\vartheta}$, equation (5.19) can be written in the basis of eigenvectors, i.e.

$$\frac{\mathrm{d}\widehat{\vartheta}}{\mathrm{d}s} = \boldsymbol{\Lambda_A}\widehat{\vartheta}. \tag{5.20}$$

The $\mathbf{A}$-matrix has $N_{\text{s}} + 1$ pairs of eigenvalues, corresponding to the solution of the second-order problem (5.1)-(5.3). For each eigenvalue of the Jacobi-matrix $\mathbf{J}$, a pair of eigenvalues appears from the $\mathbf{A}$-matrix (except for the eigenvalue that is equal to zero corresponding to the pressure). In the ILDM method, the processes are a function of time. In that case, the processes evolve only in the direction of t^+. In the PS-ILDM method, the processes are a function of the spatial coordinate s. This means that processes evolve in the direction of s^+ and s^-. Typically, diffusion processes proceed in two directions, whereas the direction of convection is determined by the sign of the mass flow m.

As the chemical nature of the ILDM system and the PS-ILDM system are closely related, also the eigenvalues are related. The eigenvalues of matrix $\mathbf{A}$, which correspond to the eigenvalues $\lambda_i^{\mathbf{J}}$ of matrix $\mathbf{J}$ will be referred to as $\lambda_{\text{a},i}^{\mathbf{A}}$. In most cases, these eigenvalues are negative. Their counterpart will be referred to as $\lambda_{\text{b},i}^{\mathbf{A}}$. In general, these eigenvalues are positive. The eigenvalues $\lambda_{\text{a},i}^{\mathbf{A}}$ correspond to processes in the s^+-direction. The other eigenvalues are responsible for the transport in the s^--direction. In general, the $N_{\text{ph}}/2 = N_{\text{s}} + 1$ pairs of eigenvalues that appear in the PS-ILDM method can be separated roughly in two groups:

1. A first pair of eigenvalues corresponds to the conservation of mass and fluxes, given by equations (5.2) and (5.6). These eigenvalues are equal to zero, i.e. $\lambda^{\mathbf{A}}_{a,1} = \lambda^{\mathbf{A}}_{b,1} = 0$.

2. The remaining eigenvalues appear in pairs $\lambda^{\mathbf{A}}_{a,i}$ and $\lambda^{\mathbf{A}}_{b,i}$, corresponding to the solution of the second-order ODEs (5.1) and (5.3). It can be shown that the relation between a pair of eigenvalues is given by

$$\lambda^{\mathbf{A}}_{a,i} + \lambda^{\mathbf{A}}_{b,i} = \frac{1}{\delta_i}, \qquad i \in [2, N_{\mathrm{ph}}/2], \tag{5.21}$$

where δ_i can be regarded as an expression for the flame thickness. For $Le_i = 1$ for all species, δ_i is given by $\delta_i = \delta = \frac{\lambda'}{mc_p}$. The pairs of eigenvalues in this second group can be subdivided into two groups. Analogous to the ILDM method, as described in section 3.3.1:

   (a) a number of eigenvalues is equal to zero, corresponding to element ($N_e - 1$ eigenvalues) and enthalpy (one eigenvalue) conservation: $\lambda^{\mathbf{A}}_{a,i} = 0$, for $i \in [2, N_e + 1]$. In that case, the positive counterpart is given by $\lambda^{\mathbf{A}}_{b,i} = 1/\delta_i$.

   (b) a number of eigenvalues corresponds to the reaction progress. The corresponding eigenvalues in the ILDM method represent processes in the reaction space $\mathcal{R}$.

The absolute values of the eigenvalues $\lambda^{\mathbf{A}}_{a,i}$ and $\lambda^{\mathbf{J}}_i$ can not be compared directly, because the eigenvalues of the ILDM method correspond to processes in time, whereas the eigenvalues of the PS-ILDM method correspond to processes in space. In the following, the nature of the eigenvalues of (a) and (b) is explained further.

Conserved variables

To illustrate that a pair of eigenvalues is found corresponding to element and enthalpy conservation, an analytical expression for the eigenvalues is derived for the case that all Lewis numbers are equal to one. In that case, the conservation equation for enthalpy (5.3) reduces to

$$m\frac{\mathrm{d}h}{\mathrm{d}s} - \frac{\mathrm{d}}{\mathrm{d}s}\left(\frac{\lambda'}{c_p}\frac{\mathrm{d}h}{\mathrm{d}s}\right) = 0. \tag{5.22}$$

If it is also assumed that $\frac{\lambda'}{c_p}$ is constant, the eigenvalues for this equation are given by $\lambda_a = 0$ and $\lambda_b = 1/\delta = mc_p/\lambda'$. Similar expressions can be obtained for the element numbers χ_j. For the case that $\frac{\lambda'}{c_p}$ is not constant and the Lewis numbers are not equal to one, the expression for λ_b can not be given analytically. The eigenvalues that are equal to zero correspond to the conservation of elements and enthalpy. As the

flamelet equations are derived for premixed flames, enthalpy and element fractions are conserved, but due to preferential diffusion (if the Lewis numbers are not equal to one), the local values of h and χ_j may vary. However, they should always satisfy the conditions

$$m\frac{\mathrm{d}h}{\mathrm{d}s} - \frac{\mathrm{d}\psi_h}{\mathrm{d}s} = 0, \tag{5.23}$$

and

$$\sum_{i=1}^{N_s} \mu_{ij} \left(m\frac{\mathrm{d}\phi_i}{\mathrm{d}s} - \frac{\mathrm{d}\psi_i}{\mathrm{d}s} \right) = 0, \qquad j \in [1, N_e - 1]. \tag{5.24}$$

The corresponding positive eigenvalues $\lambda_{b,i}^{\mathbf{A}}$, with $i \in [2, N_e + 1]$, can be associated with local mixing processes, like for instance in a partially-premixed flame, or enthalpy variations due to heat-loss. If the time scales involved with these processes are smaller than the time scales corresponding to the reaction progress, these processes may not be assumed in steady-state. However, to be able to study to what extent the PS-ILDM method correctly predicts the coupling between chemical and diffusion processes, the enthalpy and the element fractions are considered as conserved variables. Therefore, the equations that are solved for the processes corresponding to the positive eigenvalues $\lambda_{b,i}^{\mathbf{A}}$, with $i \in [2, N_e + 1]$, can be written as a steady-state relation, or

$$\frac{\mathrm{d}\widehat{\Theta}_{b,i}}{\mathrm{d}s} = 0, \qquad i \in [2, N_e + 1], \tag{5.25}$$

with $\widehat{\Theta}_{b,i} = v_{b,i}^{\mathbf{A}} \cdot \Theta$, where the left eigenvectors $v_{b,i}^{\mathbf{A}}$ corresponds to the eigenvalues $\lambda_{b,i}^{\mathbf{A}}$.

Remaining eigenvalues

The remaining eigenvalues generally appear in pairs of positive and negative counterparts. Note that in some occasions, positive eigenvalues are observed in the ILDM method. The corresponding eigenvalues $\lambda_{a,i}^{\mathbf{A}}$ in PS-ILDM can also be positive. In that case, the counterparts $\lambda_{b,i}^{\mathbf{A}}$ of these eigenvalues can be negative, because a pair of eigenvalues satisfies the condition given in equation (5.21). In the ILDM method, positive eigenvalues are associated with growing modes. Hence, they may not be assumed in steady-state. The same holds for the eigenvalues $\lambda_{a,i}^{\mathbf{A}}$, which are positive. The positive eigenvalues $\lambda_{b,i}^{\mathbf{A}}$, however, correspond to damping modes upstream. Therefore, these eigenvalues are treated differently.

In general, two approaches to define the steady-state relations can be distinguished. In the first approach, which will be referred to as PS-ILDM I, all fast processes are assumed in steady-state, i.e. for the downstream processes

$$\frac{\mathrm{d}\widehat{\Theta}_{a,i}}{\mathrm{d}s} = 0, \qquad \forall\, i,\ \mathrm{Re}(\lambda_{a,i}^{\mathbf{A}}) \ll 0, \tag{5.26}$$

and for the upstream processes

$$\frac{d\widehat{\Theta}_{b,i}}{ds} = 0, \qquad \forall\, i,\, \text{Re}(\lambda_{b,i}^{\mathbf{A}}) \gg 0. \tag{5.27}$$

The other eigenvalues, i.e. eigenvalues with a small real part, correspond to slowly damping processes. The processes describe motions in the manifold and may not be assumed in steady-state. Alternatively, only damping modes downstream can be taken into account in the manifold. The processes with positive eigenvalues, which correspond to the reaction progress, i.e. $\lambda_{b,i}^{\mathbf{A}}$ with $i \in [N_e + 2, N_{ph}/2]$, are assumed in steady-state. This approach, which will be referred to as PS-ILDM II, is closer related to the ILDM method, where only processes in the t^+-direction are present. In that case, the steady-state relations become

$$\frac{d\widehat{\Theta}_{a,i}}{ds} = 0, \qquad \forall\, i,\, \text{Re}(\lambda_{a,i}^{\mathbf{A}}) \ll 0, \tag{5.28}$$

and

$$\frac{d\widehat{\Theta}_{b,i}}{ds} = 0, \qquad i \in [N_e + 2, N_{ph}/2]. \tag{5.29}$$

5.2.4 Manifold computation and application

The equations that define a manifold point $\boldsymbol{\Theta}$ are similar to the ILDM equations (3.41)-(3.43). Firstly, a number of steady-state equations must be solved. Secondly, a number of equations describe a manifold point in terms of the conserved variables. Finally, parameterisation equations are needed to describe the reaction progress. The steady-state relations (5.25), (5.26) and (5.27) (or equivalently equations (5.25), (5.28) and (5.29)) can be written as

$$\widehat{\Omega}_i = \boldsymbol{v}_i^{\mathbf{A}} \cdot \boldsymbol{\Omega} = 0, \qquad i \in [1, N_{ss}], \tag{5.30}$$

where the transformation $\widehat{\boldsymbol{\Omega}} = \mathbf{U}_{\mathbf{A}}^{-1}\boldsymbol{\Omega}$ is used. The conserved variables can be parameterised by

$$\mathbf{P}_{\mathbf{A}}^{nr}(\boldsymbol{\Theta} - \boldsymbol{\Theta}_m) = \boldsymbol{\alpha}, \tag{5.31}$$

with $\mathbf{P}_{\mathbf{A}}^{nr}$ a $(N_c^{nr} \times N_{ph})$-dimensional matrix and $\boldsymbol{\Theta}_m$ a point that is already on the manifold. Note that the right hand side of equation (5.31) is not necessarily equal to zero. To capture enthalpy variations due to heat-loss and mixture fraction variations in a non-premixed or partially-premixed system, also steps in the direction of the conserved variables can be taken. However, this will not be done in this thesis. Finally, the parameterisation of the reaction progress is given by

$$\mathbf{P}_{\mathbf{A}}^{r}(\boldsymbol{\Theta} - \boldsymbol{\Theta}_m) = \boldsymbol{\beta}, \tag{5.32}$$

where $\mathbf{P}_{\mathbf{A}}^{r}$ is a $(N_c^{r} \times N_{ph})$-dimensional matrix.

The procedure to compute the manifold is similar to the method described in section 3.3.3, so it will not be discussed here. Due to the positive eigenvalues, the sorting of eigenvalues is more complicated than in the ILDM method. A detailed description of the selection of the eigenvalues is given in appendix C. The database is parameterised by controlling variables $\boldsymbol{\Theta}_c$, which is given by

$$\boldsymbol{\Theta}_c = \mathbf{P}_{p,A}\boldsymbol{\Theta} = \begin{pmatrix} \mathbf{P}_{p,A}^{r} \\ \mathbf{P}_{p,A}^{nr} \end{pmatrix} \boldsymbol{\Theta}, \tag{5.33}$$

and the parameter m, which is an additional controlling variable.

In the CFD computation, only equations for the controlling variables are solved. The parameter m, which represents the mass flow locally perpendicular to the flame surface, is constant in a one-dimensional premixed flame, which is flat. However, in a CFD computation the local mass burning rate may change for instance due to stretch. Hence, m is evaluated every time step. Subsequently, it is used in combination with the other controlling variables as a look-up parameter for the manifold. The conservation equations are projected on the manifold with the eigenvectors. For the ILDM method, the general system of equations can be written as in equation (3.51). For the PS-ILDM method, the flamelet equations (3.63)-(3.65) are written as,

$$\frac{d\boldsymbol{\Theta}}{ds} = \boldsymbol{\Omega}(\boldsymbol{\Theta}) + T(\boldsymbol{\Theta}), \tag{5.34}$$

where the vector T represents the multi-dimensional perturbations like flame stretch and flame curvature. Together with the kinematic equation (3.55), which describes the motion of the flame front, equation (5.34) fully represents the complete system (3.51). Analogous to the ILDM method, the system of equations is projected on the manifold.

$$\frac{\partial\boldsymbol{\Theta}_c}{\partial t} = \boldsymbol{\Omega}_c(\boldsymbol{\Theta}_c) + \mathbf{P}_{p,A}\left(\mathbf{I} - \mathbf{U}_{A,f}\mathbf{V}_{A,f}\right)T(\boldsymbol{\Theta}), \tag{5.35}$$

where $\mathbf{I}$ is the $(N_{ph} \times N_{ph})$-identity matrix, $\mathbf{U}_{A,f}$ is a $(N_{ph} \times N_{ss})$ matrix, which contains the right eigenvectors corresponding to the steady-state processes, and $\mathbf{V}_{A,f}$ is a $(N_{ss} \times N_{ph})$ matrix that contains the corresponding left eigenvectors.

Figure 5.3 shows a schematic example of the projection of the transport terms in the ILDM method (figure 5.3a) and the PS-ILDM method (figure 5.3b). In the ILDM method, the convection and the diffusion terms are projected on the manifold. It can be shown that only the diffusion terms are not necessarily tangential to the manifold [27]. In a large part of the reaction layer of a premixed flame, the diffusion term is in the same order as the chemical source term (cf. figure 3.5). In that case, an inaccurate projection method may lead to significant errors during the application of an ILDM (even though it is expected that these errors are less significant than the inaccuracies in the reduced mechanism itself). In the PS-ILDM method, it is assumed that most of the transport terms are included in the manifold. The terms

(a) ILDM   (b) PS-ILDM
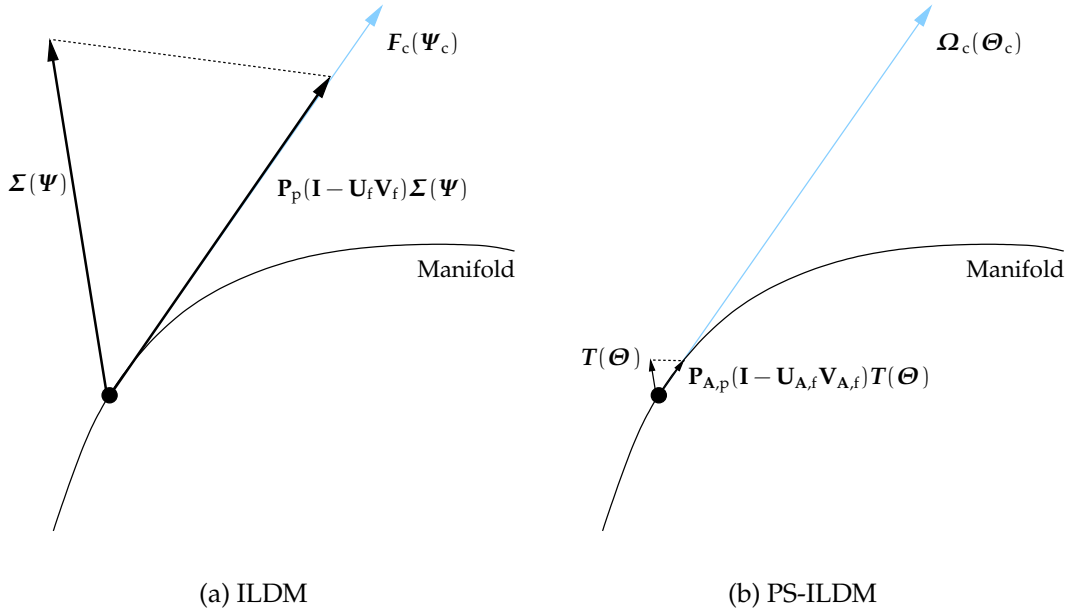
Figure 5.3 : A geometrical representation of the projection method in the ILDM method (figure a) and the PS-ILDM method (figure b). The transport terms $\boldsymbol{\Sigma}(\boldsymbol{\Psi})$ and $\boldsymbol{T}(\boldsymbol{\Theta})$ that are not tangential to the manifold are projected on the manifold by means of an eigenvector projection. Note that the projection is not necessarily orthogonal, because the eigenvectors corresponding to the fast and the slow processes are not necessarily orthogonal.

that are neglected during the construction of a manifold are perturbations caused by the multi-dimensional effects $\boldsymbol{T}(\boldsymbol{\Theta})$. In general, these terms are much smaller than the terms perpendicular to the flame, which are gathered in the source term $\boldsymbol{\Omega}_c(\boldsymbol{\Theta}_c)$. Only if the one-dimensional flame structure is strongly distorted, which happens for example in highly turbulent flames, $\boldsymbol{T}(\boldsymbol{\Theta})$ can not be neglected. However, in case $\boldsymbol{T}(\boldsymbol{\Theta})$ is small, equation (5.35) can be approximated by

$$\frac{\partial \boldsymbol{\Theta}_c}{\partial t} = \boldsymbol{\Omega}_c(\boldsymbol{\Theta}_c) + \boldsymbol{T}_c(\boldsymbol{\Theta}_c), \tag{5.36}$$

with $\boldsymbol{T}_c(\boldsymbol{\Theta}_c) = \mathbf{P}_{p,\mathbf{A}}\boldsymbol{T}(\boldsymbol{\Theta})$. If it is possible to parameterise the manifold uniquely by using only the species concentrations and the enthalpy as controlling variables, the flux terms ψ_i and ψ_h are not needed during the application of a PS-ILDM. In that case, only the species concentrations and enthalpy are stored in the database. Note that in the derivation of equation (5.36), it is assumed that diffusion processes are taken into account in the manifold.

5.3   Analysis of the eigenvalues and eigenvectors of the PS-ILDM method

In this section, the PS-ILDM method is analysed further. The eigenvalues and eigenvectors are analysed by means of a basic example, in which it is assumed that all Lewis numbers are equal to one. For this purpose, the ILDM system (3.32) can be written as

$$m\frac{\mathrm{d}\boldsymbol{\epsilon}}{\mathrm{d}s} = m\mathbf{J}^*\boldsymbol{\epsilon}, \tag{5.37}$$

where for simplicity the pressure is omitted from the vector $\boldsymbol{\epsilon}$. The Jacobi matrix $\mathbf{J}^*$ can be diagonalised according to $\mathbf{J}^* = \mathbf{U}^*\boldsymbol{\Lambda}^*\mathbf{U}^{*-1}$. Using the transformation $\widehat{\boldsymbol{\epsilon}} = \mathbf{U}^{*-1}\boldsymbol{\epsilon}$, the diagonalised system yields

$$m\frac{\mathrm{d}\widehat{\boldsymbol{\epsilon}}}{\mathrm{d}s} = m\boldsymbol{\Lambda}^*\widehat{\boldsymbol{\epsilon}}. \tag{5.38}$$

To make a fair comparison with an ILDM, the PS-ILDM method is evaluated for the case that $Le_i = 1$, for $i \in [1, N_s]$. In that case, the conservation equations of species can be written as

$$m\frac{\mathrm{d}\phi_i}{\mathrm{d}s} - \frac{\mathrm{d}}{\mathrm{d}s}\left(\frac{\lambda}{c_p}\frac{\mathrm{d}\phi_i}{\mathrm{d}s}\right) = \omega_i, \qquad i \in [1, N_s] \tag{5.39}$$

and the fluxes ψ_i are defined according to (5.4) for all species. In addition, the enthalpy equation is given by

$$m\frac{\mathrm{d}h}{\mathrm{d}s} - \frac{\mathrm{d}}{\mathrm{d}s}\left(\frac{\lambda}{c_p}\frac{\mathrm{d}h}{\mathrm{d}s}\right) = 0 \tag{5.40}$$

and the enthalpy flux yields $\psi_h = \frac{\lambda}{c_p}\frac{\mathrm{d}h}{\mathrm{d}s}$. The matrix $\mathbf{A}$ of equation (5.17) for this system is given by

$$\mathbf{A} = \begin{pmatrix} \mathbf{O} & \frac{c_p}{\lambda}\mathbf{I} \\ -m\mathbf{J}^* & m\frac{c_p}{\lambda}\mathbf{I} \end{pmatrix}. \tag{5.41}$$

The PS-ILDM system (5.18) can be transformed according to

$$\frac{\mathrm{d}\tilde{\boldsymbol{\vartheta}}}{\mathrm{d}s} = \tilde{\mathbf{A}}\tilde{\boldsymbol{\vartheta}}, \tag{5.42}$$

where the transformation $\tilde{\boldsymbol{\vartheta}} = \tilde{\mathbf{U}}^{-1}\boldsymbol{\vartheta}$ has been used. The transformation matrix $\tilde{\mathbf{U}}$ is given by

$$\tilde{\mathbf{U}} = \begin{pmatrix} \mathbf{U}^* & \mathbf{O} \\ \mathbf{O} & \mathbf{U}^* \end{pmatrix}. \tag{5.43}$$

In addition, the matrix $\tilde{\mathbf{A}}$ is given by

$$\tilde{\mathbf{A}} = \tilde{\mathbf{U}}^{-1}\mathbf{A}\tilde{\mathbf{U}} = \begin{pmatrix} \mathbf{O} & \frac{c_p}{\lambda}\mathbf{I} \\ -m\boldsymbol{\Lambda}^* & m\frac{c_p}{\lambda}\mathbf{I} \end{pmatrix}. \tag{5.44}$$

The eigenvalues of $\tilde{\mathbf{A}}$ are given by

$$\lambda_{\mathrm{a},i}^{\tilde{\mathbf{A}}} = \frac{1}{2}mL\left(1 - \sqrt{1 - 4\lambda_i^{\mathbf{J}^*}/mL}\right), \qquad i \in [2, N_{\mathrm{ph}}/2], \qquad (5.45)$$

$$\lambda_{\mathrm{b},i}^{\tilde{\mathbf{A}}} = \frac{1}{2}mL\left(1 + \sqrt{1 - 4\lambda_i^{\mathbf{J}^*}/mL}\right), \qquad i \in [2, N_{\mathrm{ph}}/2], \qquad (5.46)$$

where the parameter L is given by $L = c_p/\lambda'$. Note that the pair of eigenvalues equal to zero, which was presented in section 5.2.3, does not appear from $\tilde{\mathbf{A}}$, because the Lewis numbers are defined for all species.

The difference between the ILDM system and the PS-ILDM system can be described by the parameter m. Therefore, it is interesting to investigate the limits $m \to 0$ and $m \to \infty$. For the limit $m \to \infty$, the flamelet equations (5.39) and (5.40) reduce to the homogeneous system (3.2)-(3.3). This behaviour is also shown by the limit of the eigenvalues $\lambda_{\mathrm{a},i}^{\mathbf{A}}$ and $\lambda_{\mathrm{a},i}^{\mathbf{A}}$, i.e.

$$\lim_{m \to \infty} \lambda_{\mathrm{a},i}^{\mathbf{A}} = \lambda_i^{\mathbf{J}^*}, \qquad i \in [1, N_{\mathrm{ph}}/2], \qquad (5.47)$$

$$\lim_{m \to \infty} \lambda_{\mathrm{b},i}^{\mathbf{A}} = mL - \lambda_i^{\mathbf{J}^*} = \frac{Le}{\delta} - \lambda_i^{\mathbf{J}^*}, \qquad i \in [1, N_{\mathrm{ph}}/2]. \qquad (5.48)$$

On the other hand, for the limit $m \to 0$, the equations (5.39)-(5.40) reduce to a diffusion reaction system, which is symmetrical. In that case, also the eigenvalues are symmetrical, with respect to zero:

$$\lim_{m \to 0} \lambda_{\mathrm{a},i}^{\mathbf{A}} = -\sqrt{-mL\lambda_i^{\mathbf{J}^*}} = -\sqrt{-\frac{Le}{\delta}\lambda_i^{\mathbf{J}^*}}, \qquad i \in [1, N_{\mathrm{ph}}/2], \qquad (5.49)$$

$$\lim_{m \to 0} \lambda_{\mathrm{b},i}^{\mathbf{A}} = +\sqrt{-mL\lambda_i^{\mathbf{J}^*}} = +\sqrt{-\frac{Le}{\delta}\lambda_i^{\mathbf{J}^*}}, \qquad i \in [1, N_{\mathrm{ph}}/2]. \qquad (5.50)$$

In addition, the right eigenvectors of $\tilde{\mathbf{A}}$ are given by

$$\mathbf{u}_{\mathrm{a},i}^{\tilde{\mathbf{A}}} = \begin{pmatrix} \widehat{\boldsymbol{\epsilon}} \\ \widehat{\boldsymbol{\epsilon}}\lambda_{\mathrm{a},i}^{\tilde{\mathbf{A}}}/L \end{pmatrix}, \qquad i \in [1, N_{\mathrm{ph}}/2], \qquad (5.51)$$

$$\mathbf{u}_{\mathrm{b},i}^{\tilde{\mathbf{A}}} = \begin{pmatrix} \widehat{\boldsymbol{\epsilon}} \\ \widehat{\boldsymbol{\epsilon}}\lambda_{\mathrm{b},i}^{\tilde{\mathbf{A}}}/L \end{pmatrix}, \qquad i \in [1, N_{\mathrm{ph}}/2]. \qquad (5.52)$$

This analysis shows that the part $\widehat{\boldsymbol{\epsilon}}$ of the PS-ILDM eigenvectors, which corresponds to the composition space $\mathcal{C}$ is equal to the ILDM eigenvectors, even though the corresponding eigenvalues are different. Therefore, the PS-ILDM manifold includes no extra information of diffusion processes for the case that all Lewis numbers are equal to one. However, if the Lewis numbers are not equal to one, the eigenvectors $\mathbf{U}$ can not be used to diagonalise the Jacobi matrix $\mathbf{J}^*$ in the transformation of equation (5.44). Subsequently, the composition part of the PS-ILDM eigenvectors corresponding to the composition space is not equal, so the resulting manifold will be different. In the remaining part of this chapter, only PS-ILDMs with Lewis numbers unequal to one are evaluated.

5.4   A reactive system with three components

In this section, the PS-ILDM and ILDM methods are applied to the simple system with three species, which was introduced in section 3.1.1. Both an ILDM and a PS-ILDM are computed and compared to the exact solution of the flamelet equations (5.1)-(5.3). In this example, only a one-dimensional PS-ILDM is computed, as the example is only meant to show that a PS-ILDM can incorporate diffusion effects. As already introduced in section 3.1.1, the system consists of three species, O^*, O^{**}, and O^{***}, and three reversible reactions,

$$O^* \xrightarrow{k_1} O^{**}, \quad O^{**} \xrightarrow{k_2} O^{***} \text{ and } O^{***} \xrightarrow{k_3} O^{**}, \tag{5.53}$$
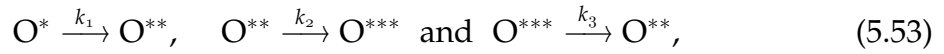
with k_j, $j \in [1, N_r]$ the elementary reaction rates (with dimension 1/s). For simplicity it is assumed that the heat release of the reactions is zero, so the temperature remains constant. The evolution of the system in that case is only described by the equations for the species. Furthermore, the enthalpy and the pressure can be omitted from the state space vector Ψ and the phase space vector Θ.

5.4.1   The ILDM system

This simple example has been used earlier to explain the ILDM method [27]. Therefore, only the main steps are presented here. With equations (2.24) and (2.25), the set of equations (3.2)-(3.4), which describes the chemical evolution of the system can be written as

$$\rho \frac{d\phi_{O^*}}{dt} = -\rho k_1 \phi_{O^*}, \tag{5.54}$$

$$\rho \frac{d\phi_{O^{**}}}{dt} = \rho k_1 \phi_{O^*} - \rho k_2 \phi_{O^{**}} + \rho k_3 \phi_{O^{***}}, \tag{5.55}$$

$$\rho \frac{d\phi_{O^{***}}}{dt} = \rho k_2 \phi_{O^{**}} - \rho k_3 \phi_{O^{***}}. \tag{5.56}$$

Due to the linearity of the source terms, the system of equations can be put in the form of equation (3.32) directly, where the Jacobi matrix $\mathbf{J}$ is given by

$$\mathbf{J} = \begin{pmatrix} -k_1 & 0 & 0 \\ k_1 & -k_2 & k_3 \\ 0 & k_2 & -k_3 \end{pmatrix}. \tag{5.57}$$

The N_s eigenvalues of the ILDM method are $\lambda_1^J = 0$, $\lambda_2^J = -k_1$ and $\lambda_3^J = -(k_2 + k_3)$.

5.4.2   The PS-ILDM system

The set of flamelet equations for this system is given by

$$m\frac{d\phi_{O^*}}{ds} - \frac{d}{ds}\left(\frac{\lambda'}{c_p Le_{O^*}}\frac{d\phi_{O^*}}{ds}\right) = -\rho k_1 \phi_{O^*}, \tag{5.58}$$

$$m\frac{d\phi_{O^{**}}}{ds} - \frac{d}{ds}\left(\frac{\lambda'}{c_p Le_{O^{**}}}\frac{d\phi_{O^{**}}}{ds}\right) = \rho k_1 \phi_{O^*} - \rho k_2 \phi_{O^{**}} + \rho k_3 \phi_{O^{***}}, \tag{5.59}$$

$$M_{\phi_{O^*}}\phi_{O^*} + M_{\phi_{O^{**}}}\phi_{O^{**}} + M_{\phi_{O^{***}}}\phi_{O^{***}} = 1. \tag{5.60}$$

After introducing the fluxes ψ_i according to equation (5.4), the conservation equations can be written in the form of equation (5.15). Due to the simplicity of the chemical reaction mechanism, the source term $\Omega(\Theta)$ is already a linear function of ϕ_i and ψ_i, so the conservation equations can directly be put in the form of equation (5.18), where the matrix $\mathbf{L}$ is given by

$$\mathbf{L} = \begin{pmatrix} Le_{O^*}L & 0 & 0 \\ 0 & Le_{O^{**}}L & 0 \\ -Le_{O^*}L & -Le_{O^{**}}L & 0 \end{pmatrix}, \tag{5.61}$$

$\Theta = (\phi_{O^*}, \phi_{O^{**}}, \phi_{O^{***}}, \psi_{O^*}, \psi_{O^{**}}, \psi_{O^{***}})^{\mathrm{T}}$ is a vector in the composition phase space and $L = c_p/\lambda$. The $2N_s$ eigenvalues of the PS-ILDM system yield

$$\lambda_{a,1}^{\mathbf{A}} = \lambda_{b,1}^{\mathbf{A}} = 0, \tag{5.62}$$

$$\lambda_{a,2}^{\mathbf{A}} = \frac{1}{2}mLe_{O^*}L\left(1 - \sqrt{(1 + 4\rho k_1/Le_{O^*}Lm^2)}\right), \tag{5.63}$$

$$\lambda_{b,2}^{\mathbf{A}} = \frac{1}{2}mLe_{O^*}L\left(1 + \sqrt{(1 + 4\rho k_1/Le_{O^*}Lm^2)}\right), \tag{5.64}$$

$$\lambda_{a,3}^{\mathbf{A}} = \frac{1}{2}mLe_{O^{**}}L\left(1 - \sqrt{1 + 4\rho(k_2 + k_3)/Le_{O^{**}}Lm^2}\right), \tag{5.65}$$

$$\lambda_{b,3}^{\mathbf{A}} = \frac{1}{2}mLe_{O^{**}}L\left(1 + \sqrt{1 + 4\rho(k_2 + k_3)/Le_{O^{**}}Lm^2}\right). \tag{5.66}$$

As described earlier, the eigenvalues found in the ILDM analysis reappear in pairs in case of PS-ILDM. Note that the dimensions of the eigenvalues are different in case of the PS-ILDM method. Therefore, the absolute values of $\lambda_i^{\mathbf{J}}$ and $\lambda_i^{\mathbf{A}}$ can not be compared.

5.4.3   Results

At $s = 0$, the initial mixture is defined as $\phi_{O^*} = 1$ mol/g and $\phi_{O^{**}} = \phi_{O^{***}} = 0$ mol/g. The boundary conditions at $s \to \infty$ describe the fact that the system reaches chemical equilibrium, so the fluxes become zero, i.e. $\psi_{O^*} = \psi_{O^{**}} = \psi_{O^{***}} = 0$ mol/cm² s. In this particular system, the mass flow rate m is not an eigenvalue of the system.
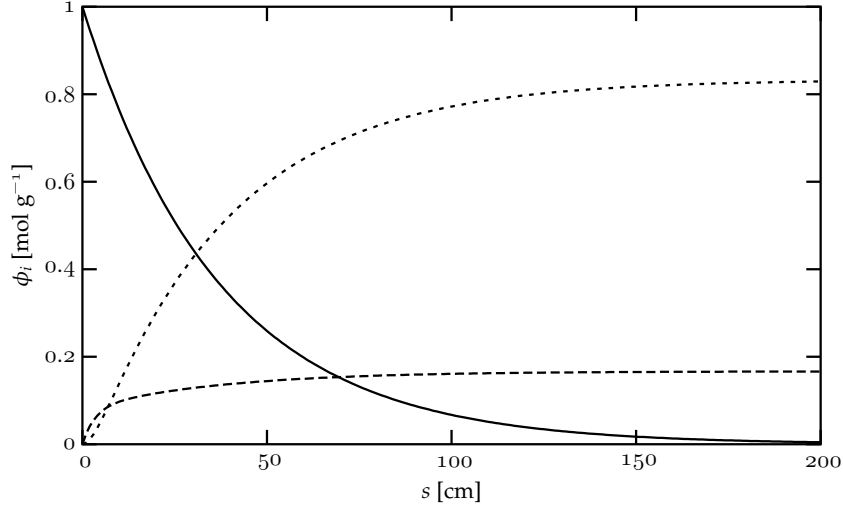
Figure 5.4 :   The exact solution of the flamelet equations (solid line: ϕ_{O^*}, long-dashed line: $\phi_{O^{**}}$, and the short-dashed line: $\phi_{O^{***}}$).

Due to the boundary conditions and the linearity of the source term, the system can be solved for different values of m. In the following analysis, m, ρ, and L are chosen as $m = 1$ g/cm² s, $\rho = 1$ g/cm³, and $L = 1$ cm s/g, respectively. Furthermore, the molar masses of the species are defined as $M_i = 1$ g/mol, for $i \in [1, N_s]$.

The reaction rates k_j are chosen in such a manner that $\lambda_3^J \ll \lambda_2^J$, i.e. $k_1 = 0.1$ s⁻¹, $k_2 = 1.0$ s⁻¹, and $k_3 = 0.2$ s⁻¹. In that case, the evolution of the chemical system is mainly determined by one slow process, corresponding to λ_2^J. Equivalently, a suitable choice is made for the Lewis numbers, so the complete system is also determined by one slowly damping mode, associated with $\lambda_{a,2}^A$. To make sure that diffusion is important, the Lewis numbers are chosen small compared to the reaction rates. Considering these arguments the Lewis numbers are chosen as $Le_{O^*} = 0.01$ and $Le_{O^{**}} = 0.1$. The exact solution of equations (5.58)-(5.60) is shown in figure 5.4.

For this problem, a one-dimensional manifold is computed with ϕ_{O^*} as controlling variable. For the ILDM method, this means that the process associated with λ_3^J is assumed in steady state, or $v_3^J \cdot F = 0$. In case of the PS-ILDM method, the processes corresponding to $\lambda_{b,2}^A$, $\lambda_{a,3}^A$, and $\lambda_{b,3}^A$ are assumed in steady-state, or $v_i^A \cdot \Omega = 0$, for the corresponding left eigenvectors. In figure 5.5a, the profile of $\phi_{O^{**}}$ of the exact solution of equations (5.1)-(5.3) is compared to the one-dimensional ILDM and PS-ILDM. Close to the equilibrium, i.e. $\phi_{O^*} = 0$, both the ILDM and the PS-ILDM are in good agreement with the exact solution. Further upstream the ILDM deviates from the exact solution, whereas the error of the PS-ILDM is still very small. Close to the unburnt mixture both the ILDM and the PS-ILDM give poor results. In figure 5.5b, the error $\epsilon_{\phi_{O^{**}}}$ of the manifolds is plotted as a function of ϕ_{O^*}. The error is defined as the difference between the manifold values of $\phi_{O^{**}}$ and the exact solution of $\phi_{O^{**}}$. Figure 5.5b clearly shows that the neglect of diffusion in the ILDM leads to a large error. The PS-ILDM performs much better, because diffusion is taken into account.

(a)   (b)
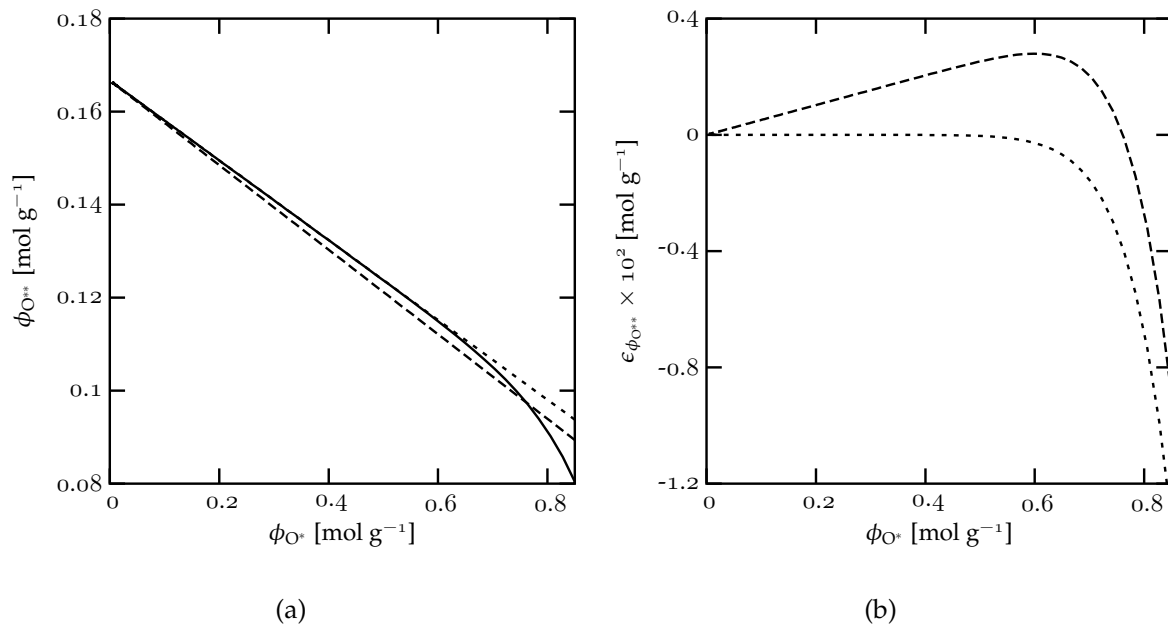
Figure 5.5 :   Results for the analytical example. The left figure shows $\phi_{O^{**}}$ as a function
of the controlling variable ϕ_{O^*} compared to the exact solution. The solid line
represents the exact solution, the long-dashed line corresponds to the ILDM
and the short-dashed line represents the PS-ILDM. The right figure shows
the error in the profile of $\phi_{O^{**}}$ of the PS-ILDM and the ILDM as a function of
ϕ_{O^*}. The long-dashed line corresponds to the ILDM and the short-dashed line
represents the PS-ILDM.

5.5 The PS-ILDM method applied to H_2/air-flames

In the previous section, the general operation of the PS-ILDM method was illustrated by means of a simple analytical example. In this section, other features of the PS-ILDM method are studied by applying the PS-ILDM method to a simple hydrogen/air mechanism. The reaction mechanism consists of 7 species and 7 reversible reactions and is listed in appendix A. The computations are presented for a stoichiometric hydrogen/air mixture with an initial temperature of 300 K at atmospheric conditions. This simple reaction mechanism is chosen, because it is possible to obtain a one-dimensional ILDM, which covers the complete domain from the unburnt mixture to the chemical equilibrium composition.

To illustrate the typical nature of the eigenvalues of a PS-ILDM, the eigenvalue spectrum of a one-dimensional PS-ILDM is analysed first. Subsequently, the PS-ILDM method is analysed for the case that the Lewis numbers are not equal to one. Finally, the effect of the parameter m is elaborated further.

5.5.1 The eigenvalue spectrum of a one-dimensional manifold

This section presents the eigenvalue spectra of one-dimensional PS-ILDMs, to illustrate the nature of the eigenvalue spectrum, discussed in section 5.2.3 The eigenvalue spectra of the one-dimensional PS-ILDMs are compared with the eigenvalue spectrum of a one-dimensional ILDM. Figure 5.6 shows the eigenvalue spectrum of the one-dimensional ILDM, which was shown in figure 3.10. The eigenvalue spectrum of the ILDM is compared with the spectrum of one-dimensional PS-ILDMs, where the processes associated to smallest negative eigenvalue correspond to processes in the manifold (figure 5.7). The parameter m was chosen to be equal to the mass burning rate of the FGM, i.e. $m = 8.137 \times 10^{-2}$ g/cm^2 s. To be able to compare the eigenvalues of the Jacobi matrix $\mathbf{J}$ with the eigenvalues of the matrix $\mathbf{A}$, the eigenvalues $\lambda_i^{\mathbf{A}}$ are multiplied by m/ρ. Figure 5.7a shows the PS-ILDM eigenvalues for the case that $Le_i = 1$, for $i \in [1, N_s]$, whereas figure 5.7b shows the eigenvalues from a PS-ILDM obtained with the Lewis numbers from table A.3. The corresponding manifolds are treated in section 5.5.2. Problems of practical nature make it impossible to obtain a manifold for the entire domain. Due to the crossing of eigenvalues, it was not possible to find a solution close to the unburnt mixture.

The figures show that pairs of eigenvalues appear from matrix $\mathbf{A}$. Furthermore, N_e eigenvalues appear, which are the positive counterpart of the eigenvalues that correspond to element $(N_e - 1)$ and enthalpy conservation (eigenvalues that are equal to zero are not shown in the figure). For the case that all Lewis numbers are equal to one, the so-called $1/\delta_i$-eigenvalues that correspond to element and enthalpy conservation are equal, i.e. $\lambda_{b,i}^{\mathbf{A}} = \frac{c_p}{m\lambda'}$ with $i \in [2, N_e + 1]$. As $\delta_i = \delta$, for the case that the Lewis numbers are equal to one, the eigenvalue spectrum is clearly structured and the pairs of eigenvalues can be distinguished easily. On the other
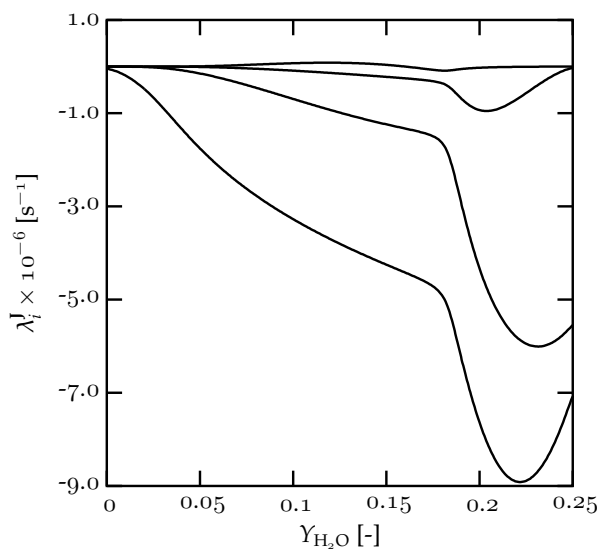
Figure 5.6 :   The eigenvalue spectrum of a one-dimensional ILDM. The eigenvalues that are
equal to zero are not shown.

hand, generally $\delta_i \neq \delta$ if the Lewis numbers are not equal to one, so the eigenvalue spectrum is less structured. However, the pairs of eigenvalues can still be distinguished. Note that the eigenvalues only represent the time scales involved. Even though the difference in the eigenvalue spectra of the PS-ILDMs is not very large, the corresponding manifolds may be completely different. The figures contain no information of the corresponding eigenvectors, which are determinant for the shape of the manifold.

5.5.2   The effect of the Lewis numbers

In section 5.3, it was shown that if the Lewis numbers are equal to one, a PS-ILDM and ILDM are identical in the composition space. Furthermore, the enthalpy and element fractions are constant in a one-dimensional flame solution. However, if the Lewis numbers are not equal to one, preferential diffusion occurs. To show that also preferential diffusion occurs in a PS-ILDM, figure 5.8a shows the enthalpy as a function of Y_{H_2O} of a one-dimensional PS-ILDM. The PS-ILDM is compared with a one-dimensional ILDM and FGM, which contains all the time scales involved. The parameter m in the PS-ILDM is chosen equal to the mass burning rate of the FGM. From figure 5.8a, it can be concluded that the PS-ILDM includes preferential diffusion effects, as enthalpy variations are included in the manifold. Close to the chemical equilibrium, the enthalpy variation of the PS-ILDM is close to the enthalpy variation of the flamelet. However, further upstream, the PS-ILDM deviates from the FGM. Figure 5.8b shows the mass fraction of H_2 for the same manifolds. From this figure, it can be concluded that close to chemical equilibrium, the PS-ILDM is more accurate than the ILDM, also because preferential diffusion effects are included. However, further upstream, both the PS-ILDM and the ILDM strongly de-

(a) $Le_i = 1$

(b) $Le_i \neq 1$
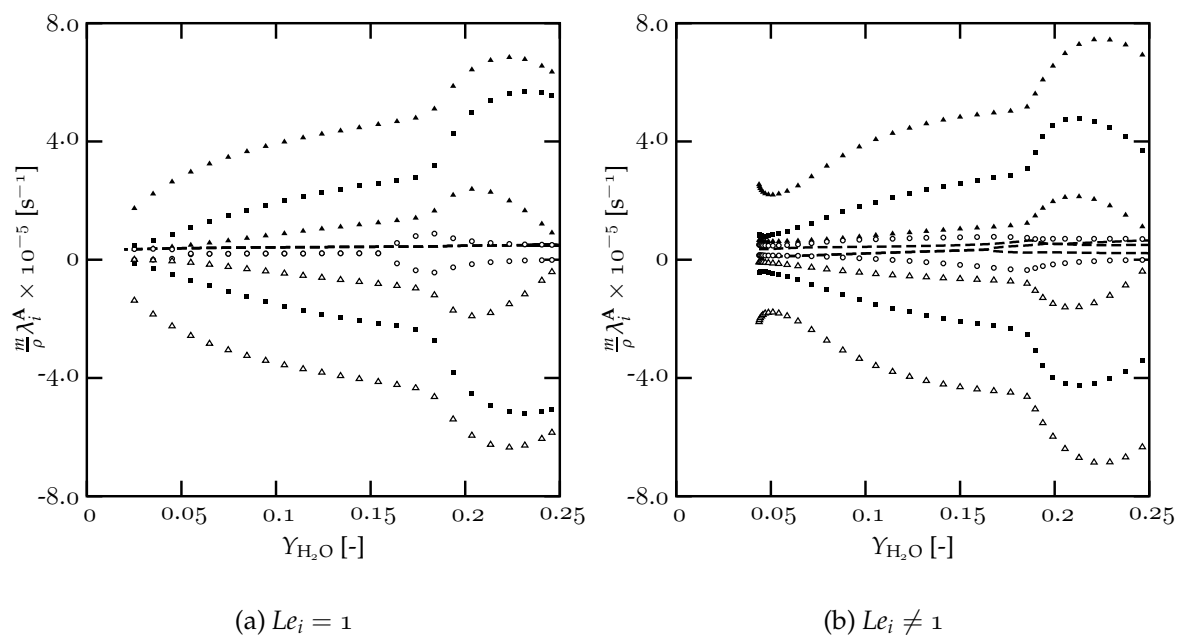
Figure 5.7 : The eigenvalue spectrum of one-dimensional PS-ILDMs, with $Le_i = 1$ (left figure) and $Le_i \neq 1$, (right figure) for $i \in [1, N_s - 1]$. The PS-ILDMs are computed with $m = m_{FGM}$. The dashed lines correspond to element and enthalpy conservation. Finally, the symbols represent the eigenvalues of the reaction progress. Pairs of eigenvalues are denoted with the same symbol. To be able to compare λ_i^A with λ_i^J, the PS-ILDM eigenvalues are multiplied by $\frac{m}{\rho}$.

(a)   (b)
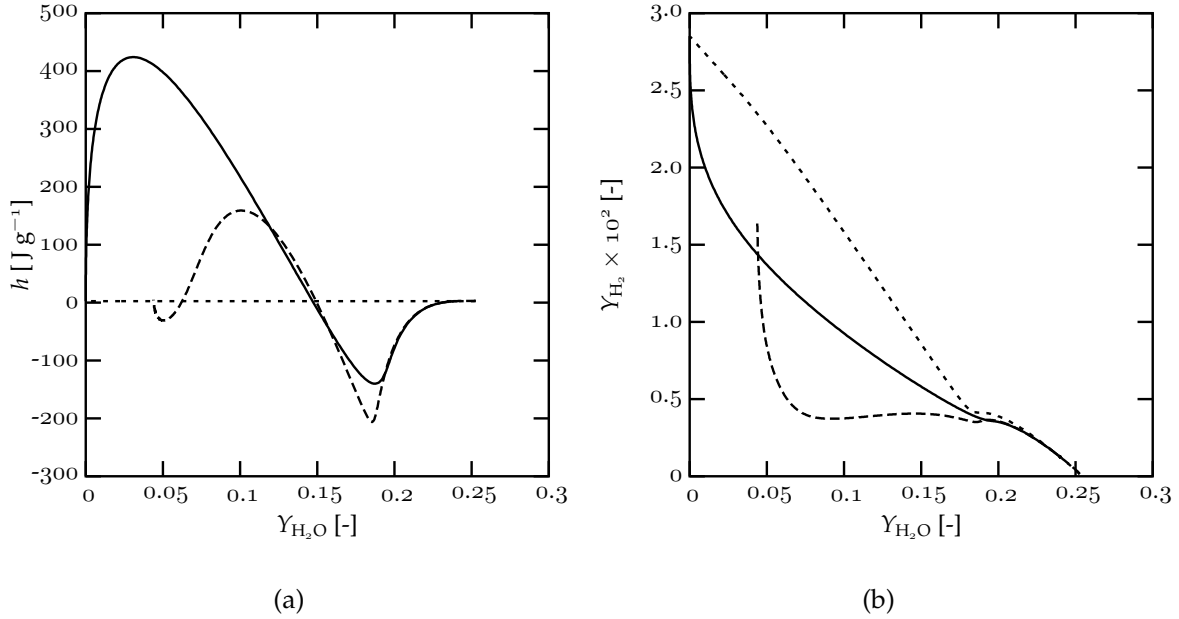
Figure 5.8 :   A one-dimensional PS-ILDM (long-dashed line) compared to a one-
dimensional ILDM (short-dashed line) and FGM (solid line). The left figure
shows h as a function of Y_{H_2O} and the right figure shows Y_{H_2} as a function of
Y_{H_2O}. The parameter m of the PS-ILDM is equal to the mass burning rate of the
FGM, i.e. $m \cong 8.137 \times 10^{-2}\ \mathrm{g\,cm^{-2}\,s^{-1}}$.

viate from the FGM.

Figure 5.8 shows that part of the difference between the ILDM and PS-ILDM is
caused by the variations in the enthalpy and element fractions, which are included
in the PS-ILDM. Therefore, it is interesting to compare the PS-ILDM with an ILDM
that is obtained at the local values of the enthalpy h and the element fractions χ_j from
the PS-ILDM. In figure 5.9a and b, three ILDMs are presented. Besides the original
one-dimensional manifold, two alternative manifolds are computed in which the
enthalpy and element fractions are not constant. In the first alternative ILDM, the
values of h and χ_j are obtained from the PS-ILDM. In the second alternative ILDM,
h and χ_j are obtained from the FGM. Figure 5.9a shows profiles of the radical Y_O.
A similar relation between the manifolds is also observed in the profiles of Y_H and
Y_{OH}. Figure 5.9b shows profiles of the major species Y_{H_2}. A similar relation between
the ILDMs and the PS-ILDM is also seen in the profiles of Y_{O_2}.

The figures show that the ILDM, with h and χ_j obtained from the PS-ILDM is
almost equal to the one-dimensional PS-ILDM. Only a small difference can be ob-
served near $Y_{H_2O} \cong 0.2$. Therefore, it can be concluded that the main difference
between the original ILDM and the PS-ILDM is caused by preferential diffusion ef-
fects in h and χ_j. For completion, an ILDM with h and χ_j obtained from the FGM is
compared with the FGM profile. The ILDM profiles are close to the FGM profile, so
it may be concluded that an ILDM where h and χ_j are used as additional controlling

(a)   (b)
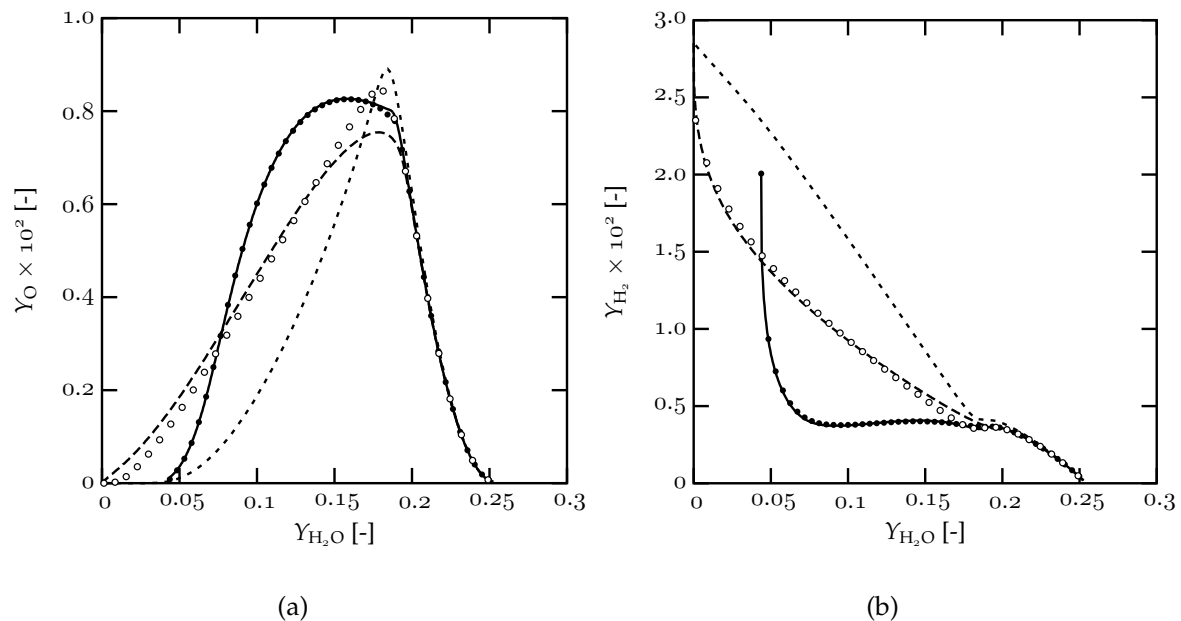
Figure 5.9 :   ILDMs with preferential diffusion included. Short dashed line: original ILDM, solid line: PS-ILDM, solid symbols: ILDM with the local values of h and χ_j from the PS-ILDM, long-dashed line: FGM, open symbols: ILDM with the local values of h and χ_j from the FGM.

variables will give accurate results for this mechanism.

5.5.3   The effect of the parameter m

As stated earlier in this chapter, the parameter m is in an indication for the importance of diffusion processes compared to reaction processes. A PS-ILDM for the limit $m \to \infty$ is equal to an ILDM, which does not include diffusion processes. In other words, an ILDM can be regarded as the limit of a PS-ILDM for an infinite ratio between chemical and diffusion time-scales. In this section, PS-ILDMs are evaluated for a finite ratio between chemical and diffusion time scales.

Figures 5.10a and b show an example of a two-dimensional manifold, with one reaction progress variable and m as additional controlling variable. The figures show Y_H and Y_{OH} as a function of m and Y_{H_2O}, respectively. Processes associated with $\lambda_{a,1}^A$ correspond to processes in the manifold. Before the effect of m on the manifold is discussed, a number of typical features, which are also observed in the ILDM method are mentioned. The first feature that can be observed is the occurrence of a so-called bifurcation. For small values of the parameter m, the manifold can not be described uniquely with the controlling variable Y_{H_2O}. Similar bifurcations are also observed for ILDMs, where the mixture fraction was used as additional controlling variable [6]. The second phenomenon that can be observed is the gap in the manifold. Due to the nature of the eigenvalue spectrum, it is not possible to find

Figure 5.10 : An example of a two-dimensional H_2/air manifold, with one reaction progress variable and m as additional controlling variable.

a solution in the complete computational domain. This phenomenon is not typical for PS-ILDM, as it is also observed in the ILDM method. However, due to the additional eigenvalues in the PS-ILDM method, it is more likely to occur than in the ILDM method.

   To show the effect of the parameter m on the manifold, the manifold of figure 5.10 is projected on the (Y_{H_2O}, Y_{OH})-plane (see figure 5.11). For comparison, the one-dimensional ILDM is added to the figure. From this figure, it can be observed that for increasing values of m, the PS-ILDM approaches the ILDM.

5.6   Manifolds with two reaction controlling variables

In this section, the PS-ILDM method is applied to a syngas/air mechanism. In the figures 5.12 and 5.13, one and two-dimensional ILDMs and PS-ILDMs are compared with the solution of the equations (5.1-5.3) for a CO-H_2/air mechanism. The detailed reaction mechanism contains 11 species and 14 reactions and is listed in appendix A. The Lewis numbers, which also given in appendix A, are obtained from mixture-averaged computations. The manifolds are constructed for a carbonmonoxide/hydrogen ratio of $Y_{CO}/Y_{H_2} = 2.45$ and an equivalence ratio of $\varphi = 1$. The initial temperature is 300 K and the pressure is 1 atm. For the PS-ILDMs, the mass burning rate m is taken from the FGM solution ($m = 0.17$ g/cm²s). This value of m is chosen to make a fair comparison between the exact solution and the manifolds. Figure 5.13 shows results for two different two-dimensional PS-ILDMs. In the manifold referred to as PS-ILDM I, the eigenvalues $\lambda_{a,1}^{\mathbf{A}}$ and $\lambda_{b,1}^{\mathbf{A}}$ are associated with processes in the manifold (corresponding to the steady-state relations of equations (5.26) and (5.27)). In the manifold referred to as PS-ILDM II, the eigenvalues $\lambda_{a,1}^{\mathbf{A}}$ and $\lambda_{a,2}^{\mathbf{A}}$ correspond to processes in the manifold (in combination with the steady-state relations of equations (5.28) and (5.29)).
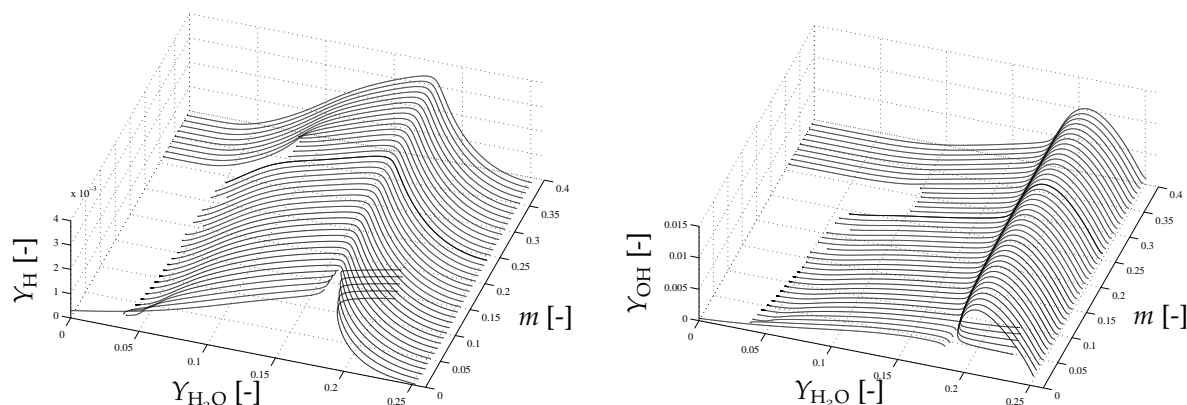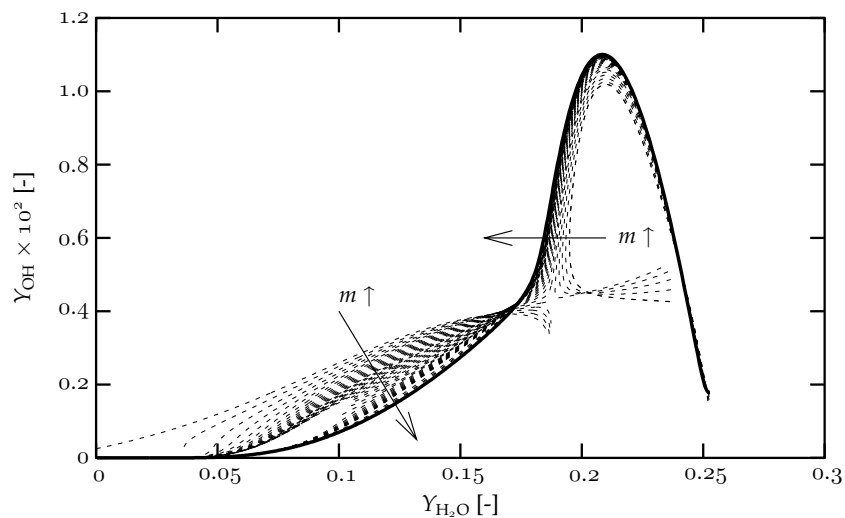
Figure 5.11 : The two-dimensional H_2/air manifold, with one reaction progress variable and m as additional controlling variable, projected on the (Y_{H_2O}, Y_{OH})-plane. The arrows indicate the direction of increasing values of m. The one-dimensional ILDM is represented by the thick solid line.

Figures 5.12a-d and 5.13a-d show profiles of the mass fractions of H_2, H, O and the temperature T as a function Y_{CO}, respectively. In figure 5.12, the FGM result is compared to a one-dimensional ILDM and a one-dimensional PS-ILDM. From the figures 5.12a-d, it can be concluded that close to chemical equilibrium, a PS-ILDM is slightly more accurate than the ILDM, because preferential diffusion is taken into account. However, at colder temperatures both manifolds behave completely different than the FGM, because only one time scale is taken into account. In figure 5.13, the FGM result is compared to a two-dimensional ILDM and two-dimensional PS-ILDMs. The trajectories of the two-dimensional manifolds are obtained by using the values of the controlling variables in the one-dimensional FGM as look-up parameters for the PS-ILDMs and ILDMs. Close to chemical equilibrium, the PS-ILDMs and ILDMs are equal to the detailed solution. However, further upstream, the two-dimensional ILDM deviates from the detailed solution, whereas the two-dimensional PS-ILDM II is still very close to the detailed solution. The two-dimensional PS-ILDM I is very accurate for H_2 and H. However, for O and T, this manifold describes a different behaviour. Even further upstream, both the ILDM and the PS-ILDMs are inaccurate. In this region, the dimension of the manifolds is probably too low to get accurate results.

The results show that especially two-dimensional PS-ILDM II is more accurate than the ILDM manifolds, because diffusion processes are included. On the other hand, two-dimensional PS-ILDM I shows good results for some profiles, while other profiles do not correspond to the FGM solution. It is not quite clear what causes the larger deviations in the Y_O and T profiles. Probably, this part of the composition

(a)

(b)

(c)

(d)

Figure 5.12 : The solution of a one-dimensional FGM (solid line) compared with a one-dimensional ILDM (dotted line) and a one-dimensional PS-ILDM (dashed line).

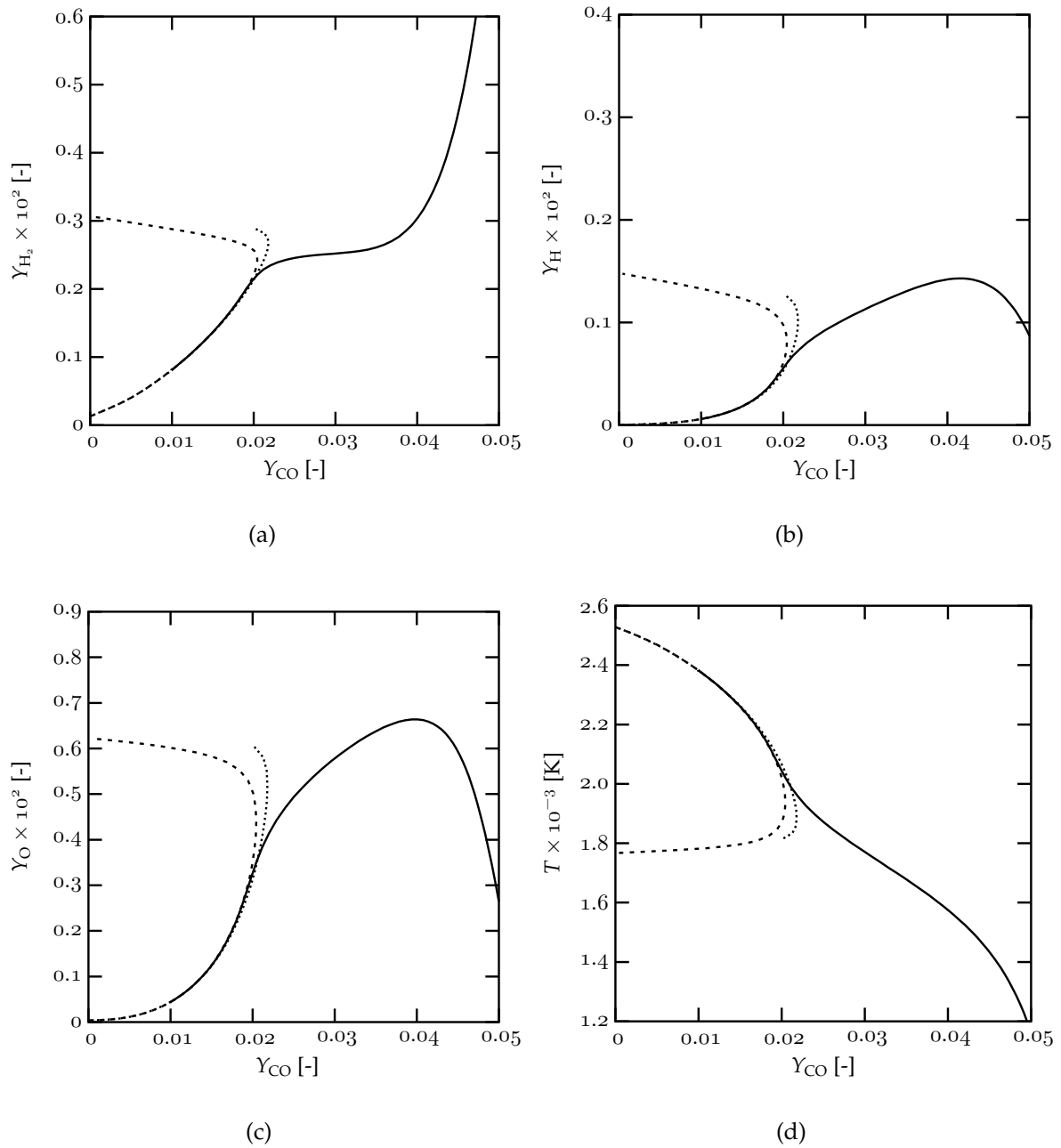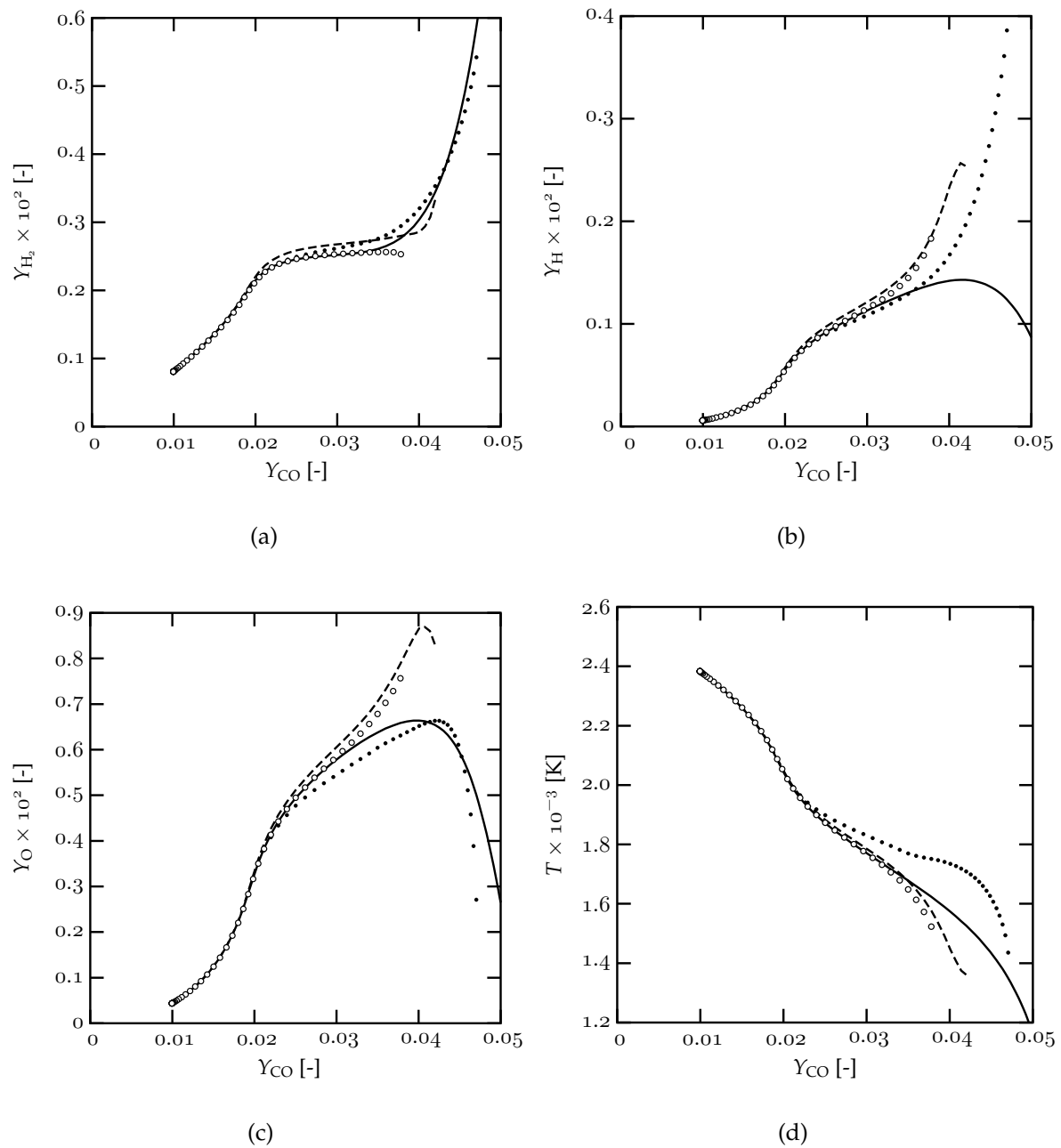**Figure 5.13** : The solution of a 1D FGM compared with two-dimensional manifolds. (solid line: FGM, dashed line: trajectories from a 2D ILDM, closed symbols: trajectories from 2D PS-ILDM I, and open symbols: trajectories from 2D PS-ILDM II.

space is dominated by processes associated with negative eigenvalues. Note that not the entire domain of Y_{CO} is shown, as it was not possible to obtain manifolds that cover the entire domain described by the FGM solution (the maximum value of Y_{CO} in the FGM yields $Y_{CO} \cong 0.056$).

5.7 Discussion

In this chapter, a new reduction method called the PS-ILDM method has been introduced. The purpose of the development of this method is to investigate whether it is possible to develop a reduction method, which has a strong mathematical background and includes information of diffusion processes. If that is the case, the method can fundamentally support the FGM method. The PS-ILDM method can be regarded as a combination of the ILDM method and the FGM method, as it combines the manifold procedure of the ILDM method with the equations that are the basis of the FGM method.

The application of the ILDM algorithm to the FGM equations is not straightforward. Due to the diffusion term, information is transported in two directions. Downstream transport is dominated by negative eigenvalues, while upstream processes are dominated by their positive counterpart. The appearance of positive eigenvalues requires a different approach in the determination of the processes which may be assumed in steady-state. The difference appears in manifolds with at least two reaction controlling variables. In this chapter, two approaches have been proposed. In the first approach, the slowest processes both the up and downstream processes are taken into account in the manifold. In the second approach, only processes associated with negative eigenvalues are taken into account in the manifold and all processes corresponding to positive eigenvalues are assumed in steady-state. In general, the second approach shows more accurate results. Probably, the upstream processes are more important in colder regions of the flame. However, it is difficult to determine the manifold in these regions, due to numerical problems.

An ILDM can be regarded as the limiting case of a PS-ILDM for an infinite ratio between chemical and transport processes. This ratio is governed by the parameter m, which represents the mass flow locally perpendicular to the flame surfaces. In premixed flames, $m = \rho u$ represents the mass burning rate, and u equals the burning velocity. In non-premixed flames, u can be regarded as the propagation velocity of the iso-contours of the progress variable Z. As m can be chosen independently, it adds an additional controlling variable to the manifold. During a CFD application of a PS-ILDM, the mass flow m is evaluated from the solution of the flame at every time step. Consequently, m should be used in combination with the other controlling variables as a look-up parameter for the manifold.

So far, the PS-ILDM method has not been applied in a realistic flame simulation. However, information about the accuracy of the method is obtained by compar-

ing PS-ILDMs qualitatively with FGMs and ILDMs. The main observation from this comparison is that the difference between a PS-ILDM and an ILDM is mainly caused by the inclusion of preferential diffusion effects, which occur if the Lewis numbers are not equal to one. In fact, it was shown in section 5.3 that a PS-ILDM and an ILDM are exactly equal if the Lewis are equal to one. Results show that the inclusion of preferential diffusion effects generally leads to a more accurate manifold than a comparable ILDM. However, if an ILDM would be created at the values of the enthalpy and element fractions from the PS-ILDM, it is shown that a PS-ILDM is nearly identical to an ILDM. On the other hand, to capture these enthalpy and element variations in an ILDM, additional controlling variables are needed.

Like in the ILDM method, the steady-state assumptions in the PS-ILDM method are based on the eigenvalue spectrum, so the same problems may occur during the construction of a PS-ILDM. For example, a bad separation between fast and slow processes leads to inaccuracies in the manifold. Furthermore, the crossing of eigenvalues may lead to numerical difficulties to obtain a manifold solution. In addition, the occurrence of turning points and bifurcations may cause problems in the parameterisation of the manifold.

To conclude, even though the concept of PS-ILDM seems very promising, in practice the method has disadvantages. In the tested examples, the accuracy of the method seems to be of the same order as the original ILDM method, which is already less accurate than the FGM method. Furthermore, similar problems that also emerge from the ILDM method are observed in the PS-ILDM method. Therefore, it is also hard to use the PS-ILDM method as a fundamental support for the FGM method.

Conclusions and recommendations

The subject of this thesis has been the development and further testing of chemical reduction methods, with a main focus on the coupling between chemical and transport processes. The general principles of chemical reduction methods were presented in chapter 3. Two existing methods were treated more intensively, i.e. the ILDM method and the FGM method. The ILDM method has a strong mathematical support, which makes it relatively easy to automate. With the introduction of so-called slow manifolds in earlier studies [65], one of the largest sources of inaccuracy remains the disregard of diffusion during the construction of the manifold. During the ILDM reduction of a detailed reaction mechanism, the fast chemical processes are assumed in steady-state. However, a time scale analysis of chemical, convection, and diffusion time scales in chapter 3 showed that, especially in a premixed flame, chemical and diffusion time scales are of the same order of magnitude in a large part of the reaction layer. Furthermore, the importance of the coupling between chemical and diffusion processes is shown in section 2.3, where several transport models are tested in a one-dimensional premixed flame configuration. Therefore, the neglect of transport processes during the construction of reduced reaction mechanisms may lead to inaccuracies during flame simulations. On the other hand, the FGM method has proven to be accurate and efficient, because both chemical and transport processes are taken into account. However, the mathematical background is less strong than in the ILDM method. As the FGM method is based on premixed flames, which are one-dimensional and adiabatic, the main source of inaccuracy is caused by multi-dimensional perturbations like heat-loss, flame stretch, and inhomogeneous mixing of fuel and oxidiser. The influence of these perturbations on the accuracy was already studied in [68].

In chapter 4, the application of the FGM method to systems that are partially-premixed has been analysed further. In this chapter, the FGM method has been applied to methane/air counterflow flames, which are one-dimensional and partially-premixed. These flames can be regarded as one-dimensional triple flames, in which both premixed and non-premixed flame fronts can be distinguished. For this purpose, a two-dimensional manifold was created, which is parameterised by one reac-

tion controlling variable and the mixture fraction. The FGM simulations were compared with detailed solutions and with results obtained with a flamelet database, which was based on non-premixed flamelets. As the premixed flame fronts appear to be the dominant structures in the flame, the FGM solution is more accurate than the solution based on non-premixed flamelets. With the non-premixed database it is not possible to reproduce the non-premixed flame structures. However, with only a two-dimensional FGM (parameterised with a reaction controlling variable and the mixture fraction) accurate results were obtained for the major species, the temperature, and the density profiles, even if mixing time scales, which correspond to the mixing of fuel and air, are of the same order as the time scales of the FGM database. This is not expected beforehand for reduction techniques, which are purely based on chemistry. Especially the non-premixed flame front is accurately reproduced by the FGM method, in contrast to what one might expect beforehand. In this part of the partially-premixed flame structure, chemistry is much faster than transport. In the premixed flame structures, however, the time scales of chemical and transport processes are of the same order. Therefore, most of the difficulties are obtained in the reproduction of the premixed flame structures, especially at the rich branch.

A number of recommendations considering the applicability of the FGM method in systems that are partially-premixed, can be made. Firstly, the accuracy of the FGM computations might be enhanced by using a three-dimensional database with two reaction controlling variables in combination with the mixture fraction. In that case, more chemical time scales are captured in the database. Secondly, as it appears that the non-premixed flame structure can be reproduced accurately with the FGM method, it is interesting to study the influence on the accuracy if the the gradient in the mixture fraction is even further increased. Thirdly, the effect of two and three-dimensional perturbations have not been studied in the same detail yet.

Although the FGM method has proven to be very accurate, its mathematical background is less strong than the ILDM method. Hence, it is for instance more difficult to automate the construction of multi-dimensional manifolds. Secondly, as stated earlier, one of the main sources of inaccuracy in an ILDM is the neglect of transport processes during the construction of the manifold. Therefore, a new reduction method has been proposed and developed in chapter 5, called the PS-ILDM method. This method can be regarded as the combination of the FGM and the ILDM method, as it uses the ILDM algorithm to obtain a manifold, which is based on the FGM equations. In that perspective, an ILDM can be regarded as a PS-ILDM for a infinite ratio between chemical and transport time scales. The general idea behind the development of the PS-ILDM method is to create a reduction method that is mathematically sound and which accounts for the influence of diffusion processes.

A simple analytical example has shown the benefit of the PS-ILDM method. Results obtained with the PS-ILDM method were more accurate than the results with the ILDM method. However, as not all time scales are included in the PS-ILDM,

it is less accurate than the corresponding FGM, which includes all the time scales involved. If the method is applied to more realistic reaction mechanisms, it appears that basically only preferential diffusion effects are taken into account. Moreover, it was shown that if it is assumed that all Lewis numbers are equal to one, a PS-ILDM is equal to an ILDM. In addition, in the tested examples, the method appears to be less accurate than the FGM method, in which all the involved time scales are taken into account. Finally, it should be remarked that some of the difficulties, which emerged from the ILDM method, also appear in the PS-ILDM method. As PS-ILDM method is strongly based on the ILDM method, it might be more successful to develop a method, which is more related to the FGM method. In addition, the PS-ILDM method can not yet be used as a theoretical support of the FGM method.

Perhaps, the benefit of the PS-ILDM method can be shown in an example, which is realistic and in which the fast and slow processes are clearly separated. This can be achieved, e.g. by regarding systems with large differences in the Lewis numbers (in a similar fashion as in the example of section 5.4). Note that such an example can only be regarded as a fundamental support of the FGM method. It does not really contribute to the PS-ILDM method as a practical reduction method. Furthermore, as the PS-ILDM method is based on the FGM method, which is based on premixed flames, the applicability of the PS-ILDM method to non-premixed flames should be investigated.

To conclude, an important aspect in the further development of reduction methods to obtain a higher accuracy can be found in the coupling between chemical and transport processes. The reduction method preferably should be applicable to both premixed and non-premixed systems. From this point of view, the PS-ILDM method has been proposed as a method in which the time scale analysis of a chemical reduction method is coupled to the accuracy of a flamelet-based method. However, from first results it can be concluded that the PS-ILDM method does not seem to offer an attractive alternative for the ILDM and the FGM method, in order to obtain manifolds which include diffusion processes.

Nomenclature

Roman symbols

A	pre-exponential factor	*
$\mathbf{A}$	phase space system matrix	*
$\mathcal{A}_i$	chemical species symbol	-
a	applied strain rate	s^{-1}
$\boldsymbol{b}_i$	external force vector	$\mathrm{g\,cm\,s}^{-2}$
$\mathcal{C}$	composition space	-
c	sound velocity	$\mathrm{cm\,s}^{-1}$
c_i	non-reacting controlling variable	*
c_p	heat capacity at constant pressure	$\mathrm{J\,g}^{-1}\,\mathrm{K}^{-1}$
$c_{p,i}$	specific heat capacity at constant pressure	$\mathrm{J\,g}^{-1}\,\mathrm{K}^{-1}$
D_i^T	thermal diffusion coefficient	$\mathrm{cm}^2\,\mathrm{s}^{-1}$
D_{ij}	multi-component diffusion coefficient	$\mathrm{cm}^2\,\mathrm{s}^{-1}$
$D_{i\mathrm{m}}$	mixture-averaged diffusion coefficient	$\mathrm{cm}^2\,\mathrm{s}^{-1}$
$\mathbf{D}$	diffusion coefficient matrix	$\mathrm{cm}^2\,\mathrm{s}^{-1}$
$\mathcal{D}_{ij}$	binary diffusion coefficient	$\mathrm{cm}^2\,\mathrm{s}^{-1}$
$\boldsymbol{d}$	direction vector	*
$\boldsymbol{d}_i$	diffusion force vector	cm^{-1}
E_a	activation energy	J
$\boldsymbol{e}$	unit vector	-
$\boldsymbol{F}$	source term vector in the state space	*
$\mathcal{G}$	level set scalar	-
h	total enthalpy	$\mathrm{J\,g}^{-1}$
h_i	specific enthalpy	$\mathrm{J\,g}^{-1}$
h_i^*	corrected specific enthalpy	$\mathrm{J\,g}^{-1}$
h_i^o	enthalpy of formation	$\mathrm{J\,g}^{-1}$
h_η, h_ξ	scale factors	cm
$\boldsymbol{I}$	unit tensor	-
$\mathbf{I}$	unit matrix	-

J	Jacobi matrix	s^{-1}
K	stretch rate	s^{-1}
$\mathcal{K}$	grid cell	-
k	reaction rate coefficient	*
Le_i	Lewis number	-
$\bar{M}$	average molar mass	$g\,mol^{-1}$
Ma	Mach number	-
M	mass	g
M_i	molar mass	$g\,mol^{-1}$
m	mass burning rate	$g\,cm^{-2}\,s^{-1}$
N_c	number of controlling variables	-
N_e	number of elements	-
N_{ph}	number of phase space variables	-
N_s	number of species	-
N_{st}	number of state variables	-
N_{ss}	number of steady-state variables	-
n	molar concentration	$mol\,cm^{-3}$
P	projection matrix	-
p	hydrostatic pressure	$g\,cm^{-1}\,s^{-2}$
Q_h	perturbation term	$J\,cm^{-3}\,s^{-1}$
Q_i	perturbation term	$g\,cm^{-3}\,s^{-1}$
$\boldsymbol{q}$	heat flux vector	$J\,cm^{-2}\,s^{-1}$
$\boldsymbol{q}_R$	radiative heat flux vector	$J\,cm^{-2}\,s^{-1}$
R	universal gas constant	$J\,mol^{-1}\,K^{-1}$
R_C	convection rate	s^{-1}
R_D	diffusion rate	s^{-1}
$\mathcal{R}$	reaction space	-
r	reaction rate	$mol\,cm^{-3}\,s^{-1}$
$\mathcal{S}$	state space	-
s_L	laminar burning velocity	$cm\,s^{-1}$
s_i	chemical source term	$g\,cm^{-3}\,s^{-1}$
s	spatial coordinate in the moving frame	cm
T	temperature	K
t	time	s
$\boldsymbol{U}_i$	diffusion velocity	$cm\,s^{-1}$
U	matrix of right eigenvectors	-
u,v	velocity components in Cartesian coordinate system	$cm\,s^{-1}$
u_s	velocity in the moving frame	$cm\,s^{-1}$
$\boldsymbol{u}_i$	right eigenvector	-

u	flow velocity	$\mathrm{cm\,s^{-1}}$
u_f	flame velocity	$\mathrm{cm\,s^{-1}}$
$\mathbf{V}$	matrix of left eigenvectors	-
V	volume	$\mathrm{cm^3}$
v_i	left eigenvector	-
X_i	mole fraction	-
x	Cartesian coordinate system	cm
x, y	Cartesian coordinates	cm
Y_i	mass fraction	-
$\mathcal{Y}$	progress variable, reacting controlling variable	-
Z	mixture fraction	-
z_j	element mass fraction	-

Greek symbols

$\alpha_{1,2}$	fitted parameter	*
$\boldsymbol{\alpha}$	direction vector	*
β	reaction constant	-
$\beta_{1,2}$	fitted parameter	*
$\boldsymbol{\beta}$	direction vector	*
$\boldsymbol{\Delta}$	diffusion coefficient matrix	$\mathrm{cm^2\,s^{-1}}$
δ	flame thickness	cm
δ_{ij}	Kronecker delta	-
δ_h	heat flux length	cm
δ_m	mixing length	cm
$\boldsymbol{\epsilon}$	difference vector in the state space	*
ϵ	relative error	-
ζ	local continuation parameter	-
η	flame adapted coordinate system	cm
η	shear viscosity	$\mathrm{g\,cm^{-1}\,s^{-1}}$
η, ξ	flame adapted coordinates	cm
η_{ji}	mass fraction of element j in species i	-
$\boldsymbol{\Theta}$	phase space vector	*
ϑ	difference vector in the phase space	*
κ	volume viscosity	$\mathrm{g\,cm^{-1}\,s^{-1}}$
$\boldsymbol{\Lambda}$	diagonalised Jacobi matrix	$\mathrm{s^{-1}}$
λ'	partial thermal conductivity	$\mathrm{J\,cm^{-1}\,s^{-1}\,K^{-1}}$
λ_i	eigenvalue	*
$\boldsymbol{\mu}_j$	element vector	-
μ_{ji}	mole fraction of element j in species i	-

ν	stoichiometric fraction	-
Π	stress tensor	$\mathrm{g\,cm^{-1}\,s^{-2}}$
ρ	mass density	$\mathrm{g\,cm^{-3}}$
Σ	perturbation term	*
σ	surface	$\mathrm{cm^2}$
τ	viscous stress tensor	$\mathrm{g\,cm^{-1}\,s^{-2}}$
τ	time scale	s
Υ	diffusion coefficient matrix	$\mathrm{cm^2\,s^{-1}}$
Φ_{ij}	coefficient in Wilkes approximation	-
ϕ	mole number vector	$\mathrm{mol\,g^{-1}}$
ϕ_i	mole number	$\mathrm{mol\,g^{-1}}$
φ	equivalence ratio	-
χ	scalar dissipation rate	$\mathrm{s^{-1}}$
χ_j	element mole number	$\mathrm{mol\,g^{-1}}$
Ψ	vector in the state space	*
ψ_h	enthalpy diffusive flux	$\mathrm{J\,cm^{-2}\,s^{-1}}$
ψ_i	species diffusive flux	$\mathrm{mol\,cm^{-2}\,s^{-1}}$
Ω	phase space source vector	*
ω	chemical source vector	$\mathrm{mol\,cm^{-3}\,s^{-1}}$
ω_i	chemical source term	$\mathrm{mol\,cm^{-3}\,s^{-1}}$

Subscripts

b	burnt
c	chemical
f	fast
l	lean
m	manifold
r	rich
st	stoichiometric
u	unburnt

Superscripts

+	production
−	consumption
o	initial
b	backward
det	detailed
eq	equilibrium
e	element

fu	pure fuel
f	forward
L	left
nr	non-reacting
ox	pure oxidiser
ref	reference
R	right
r	reacting

Abbrevations

CEM	Constraint Equilibrium Manifold
CFD	Computational Fluid Dynamics
CPU	Central Processing Unit
CSP	Computational Singular Perturbation
FGM	Flamelet-Generated Manifold
FPI	Flame Prolongation of ILDM
ILDM	Intrinsic Low-Dimensional Manifold
ISAT	In-Situ Adaptive Tabulation
LOI	Level Of Importance
ODE	Ordinary Differential Equation
PS-ILDM	Phase Space Intrinsic Low-Dimensional Manifold
RCCE	Rate-Controlled Constraint Equilibrium
TLS	Transport Linear Systems

* The unit depends on the situation

Reaction Mechanisms

In this appendix, the reaction mechanisms that are used in chapter 5 to test the PS-ILDM method are listed. The PS-ILDM method is tested with a hydrogen/air mechanism and a syngas/air mechanism. In section 2.2, it is explained how the chemical source term s_i can be derived from the elementary reactions. The speed of a reaction is determined by the reaction constants A, E_a and β. The elementary reactions and their constants of the hydrogen/air mechanism and the syngas/air mechanism are listed in table A.1 and table A.2, respectively. In a number of reactions, a third molecule is involved. This component M does not react itselve, it is needed to let the reaction proceed. The concentration of species M is given by

$$[\mathrm{M}] = \sum_{i=1}^{N_s} \xi_i [\mathrm{A}_i],\qquad\text{(A.1)}$$

with ξ_i the so-called collision efficiencies.

The hydrogen/air mechanism contains 7 species, i.e. H_2, O_2, H, O, OH, H_2O, and N_2. The reactions and the corresponding constants A, β and E_a are listed in table A.1 [27]. For the hydrogen/air mechanism, the collision efficiencies are given by: $\xi_{O_2} = 0.35$, $\xi_{H_2O} = 6.50$, $\xi_{N_2} = 0.50$, and $\xi_i = 1$ for the other species. The Lewis numbers are obtained from a premixed adiabatic flame computation with a hydrogen/air mixture, which has an equivalence ratio of $\varphi = 1.0$. In this computation, a mixture

Table A.1 : The hydrogen/air mechanism. All units are cm, s, K according to the conventions used in standard literature on combustion chemistry.

Reactions:	A	β	E_a/R
$H + O_2 \leftrightarrows OH + O$	2.00×10^{14}	0.0	8455
$O + H_2 \leftrightarrows OH + H$	5.06×10^{4}	2.67	3163
$H_2 + OH \leftrightarrows H_2O + H$	1.00×10^{8}	1.6	1660
$OH + OH \leftrightarrows O + H_2O$	1.50×10^{9}	1.14	51
$H + H + M \leftrightarrows H_2 + M$	1.80×10^{18}	-1.00	0.0
$O + O + M \leftrightarrows O_2 + M$	2.90×10^{17}	-1.00	0.0
$H + OH + M \leftrightarrows H_2O + M$	2.20×10^{22}	-2.00	0.0

averaged diffusion model is used to model the diffusion velocity (see equation 2.40). The Lewis numbers are defined as a weighted averaged of the Lewis numbers in the complete spatial domain and are given in table A.3.

Table A.2 : The syngas/air mechanism. All units are cm, s, K according to the conventions used in standard literature on combustion.

Reactions:	A	β	E_a/R
$H + O_2 \leftrightarrows OH + O$	2.00×10^{14}	0.0	8455
$O + H_2 \leftrightarrows OH + H$	1.80×10^{10}	1.0	4442
$H_2 + OH \leftrightarrows H_2O + H$	1.17×10^{9}	1.3	1825
$OH + OH \leftrightarrows O + H_2O$	6.00×10^{8}	1.3	0
$H + O_2 + M \leftrightarrows HO_2 + M$	2.30×10^{18}	-0.8	0
$H + HO_2 \leftrightarrows OH + OH$	1.50×10^{14}	0.0	505
$H + HO_2 \leftrightarrows H_2 + O_2$	2.50×10^{13}	0.0	352
$OH + HO_2 \leftrightarrows H_2O + O_2$	2.00×10^{13}	0.0	503
$CO + OH \leftrightarrows CO_2 + H$	1.51×10^{7}	1.3	-382
$HO_2 + HO_2 \leftrightarrows H_2O_2 + O_2$	2.00×10^{12}	0.0	0
$H_2O_2 + M \leftrightarrows OH + OH + M$	1.30×10^{17}	0.0	22900
$H_2O_2 + OH \leftrightarrows H_2O + HO_2$	1.00×10^{13}	0.0	906
$H + OH + M \leftrightarrows H_2O + M$	2.20×10^{22}	-2.00	0.0
$H + H + M \leftrightarrows H_2 + M$	1.80×10^{18}	-1.00	0.0

The CO-H_2/air mechanism is part of a skeletal CH_4/air mechanism [86]. The reaction constants are listed in table A.2 and the Lewis numbers are listed in table A.3. The collision efficiencies for this mechanism are given by $\xi_{O_2} = 0.40$, $\xi_{H_2O} = 6.50$, $\xi_{N_2} = 0.40$, $\xi_{CO_2} = 1.50$, $CO = 0.75$, and $\xi_i = 1$ for the other components.

Table A.3 :   The Lewis numbers and the molar masses for the hydrogen/air and the syn-
gas/air mechanism.

Species:	M_i [g mol^{-1}]	Le_i [-]	
		H$_2$/air	CO-H$_2$/air
CO$_2$	44.010	-	1.68
CO	28.011	-	1.36
H$_2$	2.0159	0.43	0.38
O$_2$	31.999	1.83	1.41
H	1.0080	0.35	0.23
O	15.999	1.18	0.89
OH	19.007	1.22	0.90
OH$_2$	33.007	-	1.48
H$_2$O	18.015	1.41	1.06
H$_2$O$_2$	34.015	-	1.46
N$_2$	28.013	-	-

Additional information on manifold applications

In chapter 4, a two-dimensional FGM was applied to a counterflow flame, which was partially premixed. This appendix discusses the data retrieval from a FGM. Firstly, the interpolation on a one-dimensional manifold is discussed. Secondly, the retrieval of data from a two-dimensional manifold is treated. Finally, the extrapolation outside the flammability limits is illustrated.

B.1   One-dimensional manifold

Consider a one-dimensional manifold, which is parameterised with the controlling variable $\mathcal{Y}$. Furthermore, it is assumed that during the application of the manifold, the value of the controlling is given by $\mathcal{Y}^*$. The entry $\mathcal{Y}^*$ is enclosed by the manifold points $\mathcal{Y}^k$ and $\mathcal{Y}^{k+1}$. The dependent variables $\boldsymbol{y}^* = \boldsymbol{y}(\mathcal{Y}^*)$ are obtained by a simple linear interpolation between the enclosing manifold points, i.e.

$$\boldsymbol{y}^* = \alpha \boldsymbol{y}^k + (1 - \alpha)\, \boldsymbol{y}^{k+1}, \tag{B.1}$$

where α is given by

$$\alpha = \frac{\mathcal{Y}^* - \mathcal{Y}^{k+1}}{\mathcal{Y}^k - \mathcal{Y}^{k+1}}. \tag{B.2}$$

B.2   Two-dimensional manifold

A two-dimensional FGM consists of a series of flamelets. Here, the look-up procedure is discussed for a two-dimensional manifold parameterised with $\mathcal{Y}$ and Z. An example of such a manifold is shown in figure 4.3. The data retrieval can be divided in a number of steps:

1. Determine where the manifold entry $(\mathcal{Y}^*, Z^*)$ is located. The two enclosing flamelets i and $i+1$ are obtained, such that $Z^i \leq Z^* < Z^{i+1}$. Furthermore, the factor β is given by

$$\beta = \frac{Z^* - Z^{i+1}}{Z^i - Z^{i+1}}. \tag{B.3}$$

2. The controlling variable is often scaled between 0 and 1. Note that the minimum and maximum values of $\mathcal{Y}$ in each flamelet can be different. In this case, it is more convenient to use the unscaled values of $\mathcal{Y}$ during the CFD application. However, during the retrieval of the dependent variables, this may cause problems, especially at the edges of the manifold. The extrema of the enclosing flamelets i and $i+1$ are given by $\mathcal{Y}^i_{\min}$, $\mathcal{Y}^i_{\max}$, $\mathcal{Y}^{i+1}_{\min}$, and $\mathcal{Y}^{i+1}_{\max}$, respectively. A correction must be applied if, for instance, the value of $\mathcal{Y}^*$ is larger than $\mathcal{Y}^i_{\max}$, but smaller than $\mathcal{Y}^{i+1}_{\max}$. Applying a correction only if $\mathcal{Y}^*$ is close to the edges of the manifold may lead to discontinuities in the profiles of dependent variables y. Therefore, it is more convenient to map the flamelets to a unit square $(\widehat{\mathcal{Y}}, \widehat{Z}) = [0, 1] \times [0, 1]$ using the extreme values of $\mathcal{Y}$ in the enclosed flamelets (cf. figure B.1). The extreme values for $\mathcal{Y}^*$ are determined according to

$$\mathcal{Y}^*_{\min} = \beta \mathcal{Y}^i_{\min} + (1 - \beta) \mathcal{Y}^{i+1}_{\min} \tag{B.4}$$

$$\mathcal{Y}^*_{\max} = \beta \mathcal{Y}^i_{\max} + (1 - \beta) \mathcal{Y}^{i+1}_{\max}. \tag{B.5}$$

Hence, the scaled value of $\mathcal{Y}^*$ is given by

$$\widehat{\mathcal{Y}}^* = \frac{\mathcal{Y}^* - \mathcal{Y}^*_{\min}}{\mathcal{Y}^*_{\max} - \mathcal{Y}^*_{\min}}. \tag{B.6}$$

Note that $\widehat{\mathcal{Y}}^* = \widehat{\mathcal{Y}}^i = \widehat{\mathcal{Y}}^{i+1}$ (see figure B.1). The scaled value of the mixture fraction is given by $\widehat{Z} = Z$, because the mixture fraction is already scaled between 0 and 1. Subsequently, the (unscaled) values of $\mathcal{Y}^i$ and $\mathcal{Y}^{i+1}$ on the enclosing flamelets can be determined, according to

$$\mathcal{Y}^i = \left(\mathcal{Y}^i_{\max} - \mathcal{Y}^i_{\min}\right) \widehat{\mathcal{Y}}^* + \mathcal{Y}^i_{\min} \tag{B.7}$$

$$\mathcal{Y}^{i+1} = \left(\mathcal{Y}^{i+1}_{\max} - \mathcal{Y}^{i+1}_{\min}\right) \widehat{\mathcal{Y}}^* + \mathcal{Y}^{i+1}_{\min}. \tag{B.8}$$

3. Retrieve the dependent variables y^* by means of a bi-linear interpolation. Because the grid points are not necessarily equally distributed on the enclosing flamelets, the values of the dependent variables are determined on the flamelets separately. Hence, the parameter α in equation (B.1) is determined for both the enclosing flamelets separately, i.e.

$$\alpha^i = \frac{\mathcal{Y}^i - \mathcal{Y}^{k+1,i}}{\mathcal{Y}^{k,i} - \mathcal{Y}^{k+1,i}} \qquad \text{and} \qquad \alpha^{i+1} = \frac{\mathcal{Y}^{i+1} - \mathcal{Y}^{k+1,i+1}}{\mathcal{Y}^{k,i+1} - \mathcal{Y}^{k+1,i+1}} \tag{B.9}$$

respectively. Note that the index i denotes the involved flamelet, whereas the index k corresponds to the enclosing grid points. Subsequently, the values of the dependent variables y can be determined for the enclosing flamelets according to,

$$y^i = \alpha^i y^{k,i} + \left(1 - \alpha^i\right) y^{k+1,i}, \tag{B.10}$$

$$y^{i+1} = \alpha^{i+1} y^{k,i+1} + \left(1 - \alpha^{i+1}\right) y^{k+1,i+1}. \tag{B.11}$$
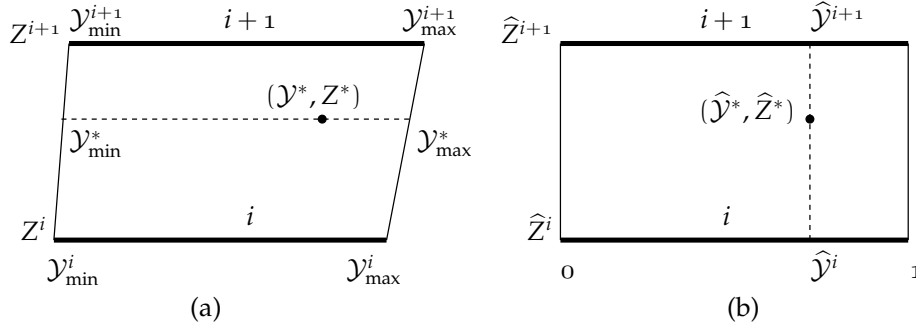
Figure B.1 : Mapping the original enclosing flamelets i and $i + 1$ (left figure) to a square (right figure) to determine the values of $\mathcal{Y}^i$ and $\mathcal{Y}^{i+1}$ (cf. equations (B.7) and (B.8)).

Finally, the dependent variables corresponding to the manifold entry $(\mathcal{Y}^*, Z^*)$ can be determined:

$$y^* = \beta y^i + (1 - \beta) y^{i+1}. \tag{B.12}$$

B.3   Data retrieval outside the flammability limits

The Z-range, for which premixed flamelets can be computed, is restricted to the flammability limits. If during the application, the value of the entry Z^* reaches values outside the flammability limits, an extrapolation of the dependent variables y must be applied. As the values $\mathcal{Y}_{\min}$ and $\mathcal{Y}_{\max}$ are equal for both $Z = 1$ and $Z = 0$, special attention must be paid to the scaling of $\mathcal{Y}$. This problem can be solved by simply assuming that the mixtures in $Z = 0$ (pure oxidiser) and $Z = 1$ (pure fuel) can be represented by flamelets, which consist of two grid points $k = 1$ and $k = 2$, with $\widehat{\mathcal{Y}}^1 = 0$ and $\widehat{\mathcal{Y}}^2 = 1$ and $y^1 = y^2$.

Outside the flammability limits ($Z \lesssim 0.02$ and $Z \gtrsim 0.11$), the chemical source terms s_i are almost zero [68], so the conservation equation for the species (3.64) reduces to

$$\frac{\mathrm{d}}{\mathrm{d}s}(mY_i) - \frac{\mathrm{d}}{\mathrm{d}s}\left(\frac{\lambda}{c_p Le_i}\frac{\mathrm{d}Y_i}{\mathrm{d}s}\right) = 0, \quad i \in [1, N_s - 1]. \tag{B.13}$$

Note that the identity of this equation is similar to the conservation equation that can be derived for the mixture fraction, i.e.

$$\frac{\mathrm{d}}{\mathrm{d}s}(mZ) - \frac{\mathrm{d}}{\mathrm{d}s}\left(\frac{\lambda}{c_p}\frac{\mathrm{d}Z}{\mathrm{d}s}\right) = 0. \tag{B.14}$$

Therefore, the solution of $Y_i(s)$ is proportional to the solution of $Z(s)$, i.e. $Y_i(s) \sim Z^{Le_i}(s)$. Since it is assumed that all Lewis numbers are equal to one, the solution of the enthalpy equation (3.65) is also proportional to the solution of $Z(s)$. Hence, the species mass fractions and the enthalpy can be interpolated linearly between the premixed flamelets and the artificial flamelets representing a mixture with pure fuel

or pure oxidiser. The temperature T can be obtained from the caloric equation of state, i.e. equation (2.6). Once the temperature is known, the density is computed with the thermal equation of state (2.11).

A less accurate, but more efficient extrapolation can be obtained by simply linearly extrapolating the density and the temperature as well. In that case, not all the species concentrations are needed during the application of an FGM.

PS-ILDM theory

In chapter 5, the PS-ILDM theory was presented. In this appendix some additional information about the PS-ILDM method is given. Firstly, the structure of the system matrix $\mathbf{A}$ is treated in more detail. Secondly, the sorting of the eigenvalues during the construction of a PS-ILDM is discussed.

C.1   The system matrix A

In equation (5.18), the starting point of the PS-ILDM theory was written as

$$\frac{\mathrm{d}\vartheta}{\mathrm{d}s} = \mathbf{A}\vartheta. \tag{C.1}$$

in which the system matrix $\mathbf{A}$ is given by

$$\mathbf{A} = \begin{pmatrix} \mathbf{O} & \mathbf{L} \\ -m\mathbf{J}^* & m\mathbf{L} \end{pmatrix}. \tag{C.2}$$

Furthermore, the matrix $\mathbf{L}$ can be written as

$$\mathbf{L} = \begin{pmatrix} L_{11} & & & & 0 & 0 \\ & & \varnothing & & & \\ & & \ddots & & \vdots & \vdots \\ & \varnothing & & & & \\ & & & L_{N_s-1,N_s-1} & 0 & 0 \\ L_{N_s,1} & \cdots & & L_{N_s,N_s-1} & 0 & 0 \\ L_{N_s+1,1} & \cdots & & L_{N_s+1,N_s-1} & 0 & L_{N_s+1,N_s+1} \end{pmatrix}, \tag{C.3}$$

with

$$L_{1,1} = Le_1 \frac{c_p}{\lambda'}, \tag{C.4}$$

$$L_{N_s-1,N_s-1} = Le_{N_s-1} \frac{c_p}{\lambda'}, \tag{C.5}$$

$$L_{N_s,1} = -\frac{M_1}{M_{N_s}} Le_1 \frac{c_p}{\lambda'}, \tag{C.6}$$

$$L_{N_s,N_s-1} = -\frac{M_{N_s-1}}{M_{N_s}} Le_{N_s-1} \frac{c_p}{\lambda'}, \tag{C.7}$$

$$L_{N_s+1,1} = M_1 h_1 \frac{c_p}{\lambda'} (Le_1 - 1), \tag{C.8}$$

$$L_{N_s+1,N_s-1} = M_{N_s-1} h_{N_s-1} \frac{c_p}{\lambda'} (Le_{N_s} - 1), \tag{C.9}$$

and

$$L_{N_s+1,N_s+1} = \frac{c_p}{\lambda'}. \tag{C.10}$$

C.2   The separation of PS-ILDM eigenvalues

To be able to define a PS-ILDM point, equations (5.30), (5.31), and (5.32) must be solved. The processes, which are assumed in steady-state are based on an eigenvalue analysis. The selection of eigenvalues differs from the ILDM method, because a number of positive eigenvalues corresponding to element and enthalpy conservation appear in the eigenvalue spectrum (cf. figure 5.7). In contrast to other positive eigenvalues, the processes corresponding to these eigenvalues are always assumed in steady-state.

The relation between the positive and negative eigenvalues is given by $\lambda_{b,i}^{A} = 1/\delta_i - \lambda_{a,i}^{A}$, for $i \in [2, N_{ph}/2]$ (cf. section 5.2.3). For the case that $Le_i \neq 1$, the expressions for δ_i can not be obtained analytically. Hence, it is not straightforward to distinguish between positive eigenvalues originating from the conserved quantities or positive eigenvalues that correspond to the reaction progress. However, if it is assumed that all Lewis numbers are equal to one, it can be shown that $\delta_i = \lambda'/mc_p$. Therefore, the procedure to select the eigenvalues is as follows:

1. The manifold computation is started in the chemical equilibrium point. This point is obtained without an eigenvalue analysis, as it is based purely on thermodynamics.

2. Once the chemical equilibrium point is found, the eigenvalues in this point are evaluated for the case that $Le_i = 1$, for $i \in [1, N_s - 1]$ and $|m| \ll 1$. The absolute value of the parameter m is chosen small, so the eigenvalues associated with the reaction progress become symmetrical with respect to zero (cf. section 5.3). In that case, pairs of positive and negative eigenvalues can easily be distinguished.

3. Subsequently, the mass burning rate is enlarged in small steps towards the desired value m^{ref}. Here, the observation is used that the left eigenvectors corresponding to the reaction progress only change slightly during a small change of m, i.e. $|v_{\text{a},i}^{\mathbf{A}\,k} \cdot v_{\text{a},i}^{\mathbf{A}\,k+1}| \cong 1$ and $|v_{\text{b},i}^{\mathbf{A}\,k} \cdot v_{\text{b},i}^{\mathbf{A}\,k+1}| \cong 1$, with $i \in [N_{\text{e}} + 2, N_{\text{ph}}/2]$ and k an index indicating a step in m. Hence, the left eigenvectors corresponding to the reaction progress are used to distinguish between positive eigenvalues associated with conserved variables and other positive eigenvalues.

4. In a next step, the Lewis numbers are changed in small steps towards the desired values Le_i^{ref}, with $i \in [1, N_{\text{s}} - 1]$.

5. Finally, the manifold construction is continued with the computation of the other manifold points. During the computation of a manifold point, the eigenvalues are separated using the left eigenvectors corresponding to the reaction progress.

References

[1] PDF/CFD-based methods: Development and validation for low emissions combustor technology, project nummer: AERO-2018-P, 1999.

[2] M.J.H. Anthonissen. *Local Defect Correction Techniques: Analysis and Application to Combustion*. PhD thesis, Eindhoven University of Technology, 2001.

[3] B.A.V. Bennett and M.D. Smooke. Local rectangular refinement with application to axisymmetric laminar flames. *Combust. Theory Modelling*, 2(10):221–258, 1998.

[4] R.W. Bilger. The structure of nonpremixed turbulent flames. *Proc. Combust. Inst.*, 22:475–488, 1988.

[5] T. Blasenbrey. *Entwicklung und Implementiering automatisch reduzierter Reaktionsmechanismen für die Verbrennung von Kohlenwasserstoffen*. PhD thesis, Universität Stuttgart, 2000.

[6] T. Blasenbrey and U. Maas. Accurate reduced models for the chemistry of hydrocarbon combustion. In *Proc. Second European Conf. on Small Burner and Heating Technology,Stuttgart*, volume 2, pages 313–322. ECSBT 2, March 2000.

[7] H. Bongers, J.A. van Oijen, and L.P.H. de Goey. Intrinsic low-dimensional manifold method extended with diffusion. *Proc. Combust. Inst.*, 29:1371–1378, 2002.

[8] C.T. Bowman, R.K. Hanson, D.F. Davidson, W.C. Gardiner, Jr., V.V. Lissianski, G.P. Smith, D.M. Golden, M. Frenklach, and M. Goldenberg. Gri-mech 2.11. http://www.me.berkeley.edu/gri_mech/, 1995.

[9] D. Bradley, A.K.C. Kwa, L.K. Lau, and M. Missaghi. Laminar flamelet modeling of recirculating premixed methane and propane-air combustion. *Combust. Flame*, 71:109–122, 1988.

[10] J. Buckmaster and M. Matalon. Anomalous Lewis number effects in tribrachial flames. *Proc. Combust. Inst.*, 22:1527–1535, 1988.

[11] H. K. Chelliah, K. Seshadri, and C. K. Law. Reduced kinetic mechanisms for counterflow methane-air diffusion flames. In N. Peters and B. Rogg, editors, *Reduced kinetic mechanisms for applications in combustion systems*, Lecture Notes in Physics m15, pages 224–240. Springer-Verlag, Berlin, 1993.

[12] CHEM1D. *a one-dimensional laminar flame code*. Eindhoven University of Technology, 2002. http://www.combustion.tue.nl.

[13] J.H. Chen, T. Echekki, and W. Kollmann. The mechanism of two-dimensional pocket formation in lean premixed methane-air flames with implications to turbulent combustion. *Combust. Flame*, 116:15–48, 1999.

[14] M. Chen, M. Herrmann, and N. Peters. Flamelet modelling of lifted turbulent methane/air and propane/air jet diffusion flames. *Proc. Combust. Inst.*, 28:167–174, 2000.

[15] F. C. Christo, A. R. Masri, and E.M. Nebot. Artificial neural network implementation of chemistry with pdf simulation of H_2/CO_2 flames. *Combust. Flame*, 106:406–427, 1996.

[16] T.P. Coffee and J.M. Heimerl. Transport algorithms for premixed, laminar steady-state flames. *Combust. Flame*, 43:273–289, 1981.

[17] T.P. Coffee and J.M. Heimerl. Transport algorithms for methane flames. *Combust. Sci. Technol.*, 34:31–43, 1983.

[18] C.F. Curtiss. Symmetric gaseous diffusion coefficients. *Journ. of Chemical Physics*, 49:2917–2919, 1968.

[19] G. Dixon-Lewis. Flame structure and flame reaction kinetics ii. transport phenomena in multicomponent systems. *Proc. Roy. Soc.*, A. 307:111–135, 1968.

[20] G. Dixon-Lewis. Structure of laminar flames. *Proc. Combust. Inst.*, 23:305–324, 1990.

[21] J. W. Dold. Flame propagation in a non-uniform mixture: Analysis of a slowly-varying triple-flame. *Combust. Flame*, 76:71–88, 1989.

[22] P. Domingo and L. Vervisch. Triple flames and partially-premixed combustion in autoignition of non-premixed turbulent mixtures. *Proc. Combust. Inst.*, 26:233–240, 1996.

[23] C.C. Douglas, A. Ern, and M.D. Smooke. Multigrid solutions of flame sheet problems on serial and parallel computers. *Parallel Algorithms and Applications*, 10:225–235, 1997.

[24] T. Echekki and J.H. Chen. Structure and propagation of methanol-air triple flames. *Combust. Flame*, 114:231–245, 1998.

[25] T. Echekki and J.H. Chen. Direct numerical simulation of autoignition in non-homogeneous hydrogen-air mixtures. *Combust. Flame*, 134:169–191, 2003.

[26] C.A. Eckett. *Numerical and Analytical Studies of the Dynamics of Gaseous Detonations*. PhD thesis, California Institute of Technology, Pasadena, California, 2000.

[27] R.L.G.M. Eggels. *Modeling of Combustion Processes and NO Formation with Reduced Reaction Mechanisms*. PhD thesis, Eindhoven University of Technology, http://www.combustion.tue.nl, 1996.

[28] R.L.G.M. Eggels and L.P.H. de Goey. Mathematically reduced reaction mechanisms applied to adiabatic flat hydrogen/air flames. *Combust. Flame*, 100:559–570, 1995.

[29] A. Ern and V. Giovangigli. *Multicomponent Transport Algorithms*. Springer-Verlag, Berlin, 1994. Lecture Notes in Physics, m24, New Series Monographs.

[30] A. Ern and V. Giovangigli. Thermal conduction and thermal diffusion in dilute polyatomic gas mixtures. *Physica A*, 214:526–546, 1995.

[31] A. Ern and V. Giovangigli. Eglib server with user's manual. http:/blanche.polytechnique.fr/www.eglib, 1996.

[32] A. Ern and V. Giovangigli. Thermal diffusion effects in hydrogen-air and methane-air flames. *Combust. Theory Modelling*, 2:349–372, 1998.

[33] A. Ern and V. Giovangigli. Impact of detailed multicomponent transport on planar and counterflow hydrogen/air and methane/air flames. *Combust. Sci. Technol.*, 149:157–181, 1999.

[34] F. Fenichel. Geometric singular perturbation theory for ordinary differential equations. *J. Diff. Eqs.*, 31:53–98, 1979.

[35] B. Fiorina, R. Baron, O. Gicquel, D. Thévenin, S. Carpentier, and N. Darabiha. Modelling non-adiabatic partially premixed flames using flame-prolongation of ILDM. *Combust. Theory Modelling*, 7:449–470, 2003.

[36] B. Fiorina, O. Gicquel, L. Vervisch, S. Carpentier, and N. Darabiha. Approximating the chemical structure of partially premixed and diffusion counterflow flames using FPI flamelet tabulation. *Combust. Flame*, 140:147–160, 2004.

[37] O. Gicquel, N. Darabiha, and D. Thévenin. Laminar premixed hydrogen/air counterflow flame simulations using flame prolongation of ILDM with differential diffusion. *Proc. Combust. Inst.*, 28:1901–1908, 2000.

[38] O. Gicquel, D. Thévenin, M. Hilka, and N. Darabiha. Direct numerical simulation of turbulent premixed flames using intrinsic low-dimensional manifolds. *Combust. Theory Modelling*, 3:479–502, 1999.

[39] L.P.H. de Goey and J.H.M. ten Thije Boonkkamp. A mass-based definition of flame stretch with finite thickness. *Combust. Sci. Technol.*, 122:399–405, 1997.

[40] L.P.H. de Goey and J.H.M. ten Thije Boonkkamp. A flamelet description of premixed laminar flames and the relation with flame stretch. *Combust. Flame*, 119:253–271, 1999.

[41] José Goldemberg, editor. *World Energy Assessment: Energy and the challenge of Sustainability*. United Nations Development Programme, 2000.

[42] G.H. Golub and C.F. Van Loan. *Matrix Computations*. John Hopkins University Press, Baltimore, 1983.

[43] J.B. Greenberg. On the prediction of thermal diffusion effects in laminar one-dimensional flames. *Combust. Sci. Technol.*, 24:83–88, 1980.

[44] Phillips H. Flame in a buoyant layer. *Proc. Combust. Inst.*, 10:1277–1283, 1965.

[45] R.D. Hancock, F.R. Schauer, R.P. Lucht, V.R. Katta, and K.Y. Hsu. Thermal diffusion effects and vortex-flame interactions in hydrogen jet diffusion flames. *Proc. Combust. Inst.*, 26:1087–1093, 1996.

[46] L. J. Hartley and J. W. Dold. Flame propagation in a nonuniform mixture: Analysis of a propagating triple-flame. *Combust. Sci. Technol.*, 80:23–46, 1991.

[47] J.O. Hirschfelder and C.F. Curtiss. Flame propagation in explosive gas mixtures. *Proc. Combust. Inst.*, 3:121–127, 1949.

[48] J.O. Hirschfelder, C.F. Curtiss, and R.B. Bird. *Molecular Theory of Gases and Liquids*. Wiley, New York, 1954.

[49] W.W. Jones and J.P. Boris. An algorithm for multispecies diffusion fluxes. *Comput. Chem.*, 5:139–146, 1981.

[50] J.C. Keck and D. Gillespie. Rate-controlled partial-equilibrium method for treating reacting gas mixtures. *Combust. Flame*, 17:237–241, 1971.

[51] R. J. Kee, G. Dixon-Lewis, J. Warnatz, M. E. Coltrin, and J. A. Miller. A fortran computer code package for the evaluation of gas-phase multicomponent transport properties. Sandia Report SAND86-8246, Sandia National Laboratories, 1986.

[52] P. N. Kioni, B. Rogg, K. N. C. Bray, and A. Liñán. Flame spread in laminar mixing layers: The triple flame. *Combust. Flame*, 95:276–290, 1993.

[53] Y.S. Ko and Chung S.H. Propagation of unsteady tribrachial flames in laminar non-premixed jets. *Combust. Flame*, 118:151–163, 1999.

[54] S.H. Lam and D.A. Goussis. Conventional asymptotics and computational singular perturbation for simplified kinetics modeling. In M.D. Smooke, editor, *Reduced kinetic mechanisms for asymptotic approximations for methane-air flames*, Lecture Notes in Physics 384, pages 227–242. Springer-Verlag, Berlin, 1991.

[55] T. Løwås, D. Nilsson, and Mauss. F. Automatic reduction procedure for chemical mechanisms applied to premixed methane/air flames. *Proc. Combust. Inst.*, 28:1809–1815, 2000.

[56] U. Maas. Efficient calculation of intrinsic low-dimensional manifolds for the simplification of chemical kinetics. *Comp. Vis. in Sci.*, 1:69–81, 1998.

[57] U. Maas and S.B. Pope. Implementation of simplified chemical kinetics based on intrinsic low-dimensional manifolds. *Proc. Combust. Inst.*, 24:103–112, 1992.

[58] U. Maas and S.B. Pope. Simplifying chemical kinetics: Intrinsic low-dimensional manifolds in composition space. *Combust. Flame*, 88:239–264, 1992.

[59] U. Maas and S.B. Pope. Laminar flame calculations using simplified chemical kinetics based on intrinsic low-dimensional manifolds. *Proc. Combust. Inst.*, 25:1349–1356, 1994.

[60] A. Massias, D. Diamantis, E. Mastorakos, and D.A. Goussis. An algorithm for the construction of global reduced mechanisms with CSP data. *Combust. Flame*, 117:685–708, 1999.

[61] S. Mathur, P. K. Tondon, and S.C. Saxena. Thermal conductivity of binary, ternary and quaternary mixtures of rare gases. *Mol. Phys.*, 12:569, 1967.

[62] C. M. Müller, H. Breitbach, and N. Peters. Partially premixed turbulent flame propagation in jet flames. *Proc. Combust. Inst.*, 25:1099–1106, 1994.

[63] L. Monchick, R.J. Munn, and E.A. Mason. Thermal diffusion in polyatomic gases: a generalized Stefan-Maxwell diffusion equation. *Journ. Chemical Physics*, 45:3051–3058, 1966.

[64] C. Muckenfuss and C.F. Curtiss. Thermal conductivity of multicomponent gas mixtures. *Journ. Chemical Physics*, 29:1273–1277, 1958.

[65] J. Nafe and U. Maas. A general algorithm for improving ILDMs. *Combust. Theory Modelling*, 6:697–709, 2002.

[66] H.N. Najm, P.H. Paul, C.J. Mueller, and P.S. Wyckoff. On the adequacy of certain experimental observables as measurements of flame burning rate. *Combust. Flame*, 113:312–332, 1998.

[67] A.T. Norris and S.B. Pope. Modeling of extinction in turbulent diffusion flames by the velocity-dissipation-composition PDF method. *Combust. Flame*, 100:211–220, 1995.

[68] J.A. van Oijen. *Flamelet-Generated Manifolds: Development and Application to Premixed Laminar Flames*. PhD thesis, Eindhoven University of Technology, http://www.combustion.tue.nl, 2002.

[69] J.A. van Oijen and L.P.H. de Goey. Modelling of premixed laminar flames using flamelet-generated manifolds. *Combust. Sci. Technol.*, 161:113–137, 2000.

[70] J.A. van Oijen and L.P.H. de Goey. Modeling of premixed counterflow flames using the flamelet-generated manifold method. *Combust. Theory Modelling*, 6:463–478, 2002.

[71] J.A. van Oijen and L.P.H. de Goey. A computational study of confined triple flames using a flamelet-generated manifold. *Combust. Theory Modelling*, 8:141–163, 2004.

[72] J.A. van Oijen, F.A. Lammers, and L.P.H. de Goey. Modeling of complex premixed burner systems using flamelet-generated manifolds. *Combust. Flame*, 127:2124–34, 2001.

[73] E.S. Oran and J.P. Boris. Detailed modelling of combustion systems. *Prog. Energy Combust. Sci.*, 7:1–72, 1981.

[74] N. Peters. Laminar flamelet concepts in turbulent combustion. *Proc. Combust. Inst.*, 21:1231–1250, 1986.

[75] N. Peters. Reducing mechanisms. In M.D. Smooke, editor, *Reduced kinetic mechanisms for asymptotic approximations for methane-air flames*, Lecture Notes in Physics 384, pages 48–85. Springer-Verlag, Berlin, 1991.

[76] N. Peters. *Turbulent Combustion*. Cambridge University Press, 2000.

[77] T. Plessing, P. Terhoeven, N. Peters, and M. S. Mansour. An experimental and numerical study of a laminar triple flame. *Combust. Flame*, 115:335–353, 1998.

[78] T. Poinsot and D. Veynante. *Theoretical and Numerical Combustion*. Edwards, Philadelphia, 2001.

[79] S. B. Pope. Computationally efficient implementation of combustion chemistry using *in situ* adaptive tabulation. *Combust. Theory Modelling*, 1:41–63, 1997.

[80] P. Popp and M. Baum. Analysis of wall heat fluxes, reaction mechanisms, and unburnt hydrocarbons during the head-on quenching of a laminar flame. *Combust. Flame*, 108:327–348, 1997.

[81] R. Rook. *Acoustics in Burner-Stabilised Flames*. PhD thesis, Eindhoven University of Technology, http://www.combustion.tue.nl, 2001.

[82] E.D. Rosner, R.S. Israel, and B. La Mantia. Heavy species Ludwig-Soret transport effects in air-breathing combustion. *Combust. Flame*, 123:547–560, 2000.

[83] G. R. Ruetsch, L. Vervisch, and A. Liñán. Effects of heat release on triple flames. *Phys. Fluids*, 7:1447–1454, 1995.

[84] R. Seydel. *From Equilibrium to Chaos, Practical Bifurcation and Stability Analysis*. Elsevier, New York, Amsterdam, London, 1988.

[85] G.P. Smith, D.M. Golden, M. Frenklach, N.W. Moriarty, B. Eiteneer, M. Goldenberg, C.T. Bowman, R.K. Hanson, S. Song, W.C. Gardiner, Jr., V.V. Lissianski, and Z. Qin. Gri-mech 3.0. http://www.me.berkeley.edu/gri_mech/.

[86] M.D. Smooke and V. Giovangigli. Formulation of the premixed and non-premixed test problems. In M.D. Smooke, editor, *Reduced kinetic mechanisms for asymptotic approximations for methane-air flames*, Lecture Notes in Physics 384, pages 1–28. Springer-Verlag, Berlin, 1991.

[87] L.M.T. Somers. *The Simulation of Flat Flames with Detailed and Reduced Chemical Models*. PhD thesis, Eindhoven University of Technology, http://www.combustion.tue.nl, 1994.

[88] Q. Tang and S.B. Pope. A more accurate projection in the rate-controlled constrained equilibrium method for dimension reduction of combustion chemistry. *Combust. Theory Modelling*, 8:255–279, 2004.

[89] J.H.M. ten Thije Boonkkamp. Numerical modelling of laminar flames. In K.R.A.M. Schreel, editor, *Course on Combustion*, J.M. Burgerscentrum courses, pages 55–69. J.M. Burgerscentrum, 2001.

[90] J.H.M. ten Thije Boonkkamp and L.P.H. de Goey. A flamelet model for premixed stretched flames. *Combust. Sci. Technol.*, 149:183–200, 2000.

[91] D. Thévenin, F. Behrendt, U. Maas, and J. Warnatz. Development of a parallel direct numerical simulation code to investigate reactive flows. *Comp. Fluids*, 25:485–496, 1996.

[92] A. N. Tikhonov, A. B. Vasil'eva, and A. G. Sveshnikov. *Differential Equations*. Springer-Verlag, Berlin, 1985.

[93] T. Turanyi. Parameterization of reaction mechanisms using orthonormal polynomials. *Comp. Chem.*, 18:45–54, 1994.

[94] J. van de Ree. On the definition of the diffusion coefficient in reacting gases. *Physica*, 36:118–126, 1967.

[95] L. Waldmann and E. Trübenbacher. Formale kinetische Theorie von Gasgemischen aus anregbaren Molekulen. *Zeitschr. Naturforsch.*, 17a:363–376, 1962.

[96] J. Warnatz, U. Maas, and R.W. Dibble. *Combustion: Physical and Chemical Fundamentals, Modeling and Simulation, Experiments, Pollutant Formation*. Springer-Verlag, Berlin, 1996.

[97] C.R. Wilke. A viscosity equation for gas mixtures. *Journal of Chemical Physics*, 18:517, 1950.

[98] F.A. Williams. Elementary derivation of the multicomponent diffusion equation. *Amer. J. Phys.*, 26:467–469, 1958.

[99] F.A. Williams. *Combustion Theory*. Addison-Wesley Publishing Company, Redwood City, 1985.

[100] K. Xiao, D. Schmidt, and U. Maas. PDF simulations of turbulent non-premixed CH_4/H_2-air flames using automatically reduced chemical kinetics. *Proc. Combust. Inst.*, 27:1073–1080, 1998.

Abstract

Detailed numerical simulations of burner systems are still very time consuming due to the complexity of detailed combustion models. Several chemical reduction techniques, which lower the computational costs without losing too much accuracy have been introduced in the past few decades. Generally, these reduction methods are based on the assumption that inside a flame, chemical time scales are much smaller than transport time scales. However, an analysis of time scales in a flame shows that transport and chemical time scales appear to be of the same order in a large part of the reaction layer, especially in a premixed flame structure. Therefore, reduction methods that are purely based on chemistry may lead to inaccuracies. In this thesis, existing reduction methods are tested and developed further, with a main focus on the coupling between chemical and transport processes.

Several reduction techniques are highlighted briefly. Two reduction techniques are treated in more detail, i.e. the *Intrinsic Low-Dimensional Manifold* (ILDM) method and the *Flamelet-Generated Manifold* (FGM) method. Both methods are so-called manifold methods, where a low-dimensional manifold which contains information of the chemical composition of the mixture is created in a pre-processing step. During a flame simulation, conservation equations are solved for the controlling variables, which parameterise the manifold, in stead of solving the full set of equations. The ILDM method, which has a strong mathematical support, may lead to inaccurate results, because transport processes are disregarded during the construction of the manifold. On the other hand, the FGM method, which is based on the solution of one-dimensional premixed flames, has proven to be accurate and efficient, because both chemical and transport processes are taken into account. However, the mathematical background is less strong than for the ILDM method.

Many practical combustion applications are partially-premixed. Deviations from one-dimensional premixed behaviour due to inhomogeneous mixing of fuel and air may cause inaccuracies during the application of the FGM in simulations of partially-premixed systems. Therefore, the FGM method is tested in a one-dimensional counterflow configuration, to be able to find a direct relation between the accuracy of the FGM method and the gradient in the mixture fraction (which is a measure for the ratio between fuel and oxidiser). A two-dimensional FGM is constructed from a series of premixed flame solutions, which have different equivalence ratios at the inlet. Good agreement has been obtained between detailed results and FGM results

for the profiles of major species and temperature, even if time scales corresponding to the mixing of fuel and air are of the same order as time scales in the FGM database. The largest problems were obtained in the reproduction of rich premixed flame fronts.

Finally, a new reduction method has been introduced and derived in this thesis, which is referred to as the *Phase Space Intrinsic Low-Dimensional Manifold* (PS-ILDM) method. To obtain a reduction method, which is mathematically sound and includes diffusion processes, the ILDM concept is applied to the equations that are used to construct an FGM. The PS-ILDM method is applied to a simple analytical example. The results show that the PS-ILDM method is more accurate than the ILDM method, because diffusion processes are included in the manifold. However, first applications to more realistic reaction mechanisms indicate that basically only preferential diffusion effects are included in the manifold. Furthermore, a PS-ILDM is less accurate than the FGM method, which includes all the chemical time scales involved.

To conclude, even though not all features of partially-premixed systems have been analysed, the FGM method appears to be a successful tool to model partially-premixed flames accurately and efficiently. Furthermore, first steps have been made in the development of a chemical reduction method, which is mathematically sound and which includes information of diffusion processes. However, further research is required to investigate the possibility of using the PS-ILDM method as a practical reduction method, which is more accurate and efficient than other reduction methods.

Samenvatting

Het gebruik van complexe en gedetailleerde modellen in numerieke simulaties van verbrandingssystemen vergt lange rekentijden. De afgelopen decennia zijn een aantal zogenaamde chemische reductiemethoden geïntroduceerd met als doel de rekentijden te verkorten, zonder daarbij veel aan nauwkeurigheid in te hoeven boeten. Over het algemeen zijn deze reductiemethoden gebaseerd op de veronderstelling dat in een vlam de chemietijdschalen veel kleiner zijn dan transporttijdschalen. Een analyse van deze vlamtijdschalen laat echter zien dat in een groot deel van de reactielaag de chemie- en transporttijdschalen van dezelfde orde van grootte zijn. Het gebruik van reductiemethoden die puur gebaseerd zijn op een analyse van de chemie kan daarom leiden tot onnauwkeurigheden tijdens een vlamberekening. Dit proefschrift richt zich op de verdere ontwikkeling van bestaande reductiemethoden, waarbij met name aandacht wordt besteed aan de koppeling tussen chemie- en transportprocessen.

Het algemene principe van een aantal reductiemethoden wordt kort beschreven. De zogenaamde *Intrinsic Low-Dimensional Manifold* (ILDM) methode en de *Flamelet-Generated Manifold* (FGM) methode worden uitvoeriger behandeld. In beide methoden wordt een database gecreëerd, waarin informatie over chemische samenstelling van het mengsel is opgeslagen. Vervolgens kan deze database worden gebruikt in een vlamsimulatie. Tijdens de simulatie hoeven in plaats van het volledige stelsel vergelijkingen alleen vergelijkingen te worden opgelost voor de zogenaamde controlevariabelen, die het manifold parameteriseren. De ILDM methode heeft een sterk mathematische achtergrond, maar kan leiden tot onnauwkeurigheden omdat tranportprocessen niet worden meegenomen tijdens het creëren van de database. Aan de andere kant is de FGM methode, die gebaseerd is op de oplossing van één-dimensionale voorgemengde vlammen, nauwkeurig, omdat zowel chemie- als transportprocessen worden meegenomen. De mathematische onderbouwing is daarentegen minder sterk als die van de ILDM methode.

In de praktijk zijn veel verbrandingssystem niet puur voorgemengd, maar deels voorgemengd. Het gebruik van de FGM methode voor het simuleren van deels voorgemengde systemen kan leiden tot onnauwkeurigheden door het niet homogeen gemengd zijn van van de brandstof en de oxidator. Om een relatie te vinden tussen de nauwkeurigheid van de FGM methode en de gradiënt in de mengfractie (wat een maat is voor de verhouding tussen brandstof en oxidator), wordt de

methode getest in een zgn. deels voorgemengde counterflow opstelling. Hiervoor is een twee-dimensionaal manifold gecreëerd van een reeks één-dimensionale voorgemengde vlammen, variërend van arm tot rijk. De resultaten met de FGM methode komen goed overeen met de gedetailleerde berekeningen wat betreft de profielen van de voornaamste stofjes en de temperatuur, zelfs wanneer de tijdschalen van het FGM van dezelfde orde van grootte zijn als de tijdschalen die horen bij de menging van brandstof en oxidator. Het nauwkeurig simuleren van de rijk voorgemengde vlamstructuur blijkt voor de meeste problemen te zorgen.

Daarnaast wordt in dit proefschrift een nieuwe reductiemethode geïntroduceerd en afgeleid: de *Phase-Space Intrinsic Low-Dimensional Manifold* (PS-ILDM) methode. In deze methode wordt het ILDM algoritme gecombineerd met de vergelijkingen van de FGM methode, om een reductiemethode te ontwikkelen die een mathematisch sterke basis heeft en bovendien nauwkeurig is omdat transportprocessen worden meegenomen in het manifold. Een simpel analytisch voorbeeld laat zien dat de PS-ILDM methode nauwkeuriger is dan de ILDM methode. Echter, eerste toepassingen van de methode op meer realistische reactiemechanismen wijzen erop dat hoofdzakelijk preferentiële diffusieprocessen worden meegenomen. Tevens is de PS-ILDM methode minder nauwkeurig dan de FGM methode, omdat daarin alle chemietijdschalen worden meegenomen.

Tot slot kan worden geconcludeerd dat de FGM methode een geschikt gereedschap is om deels voorgemengde systemen nauwkeurig en efficiënt te modelleren. Verder zijn de eerste stappen gezet in de ontwikkeling van een reductiemethode, waarin transportprocessen worden meegenomen en die tevens een sterke mathematische basis heeft. Verder onderzoek is echter nog wel noodzakelijk, om aan te tonen dat de PS-ILDM methode bruikbaar is als een praktische reductiemethode, die efficiënter en nauwkeuriger is dan reeds bestaande reductiemethoden.

Acknowledgements

The research that has lead to this thesis has been performed at the Combustion Technology Group at the faculty of Mechanical Engineering of the Eindhoven University of Technology. Rolls-Royce plc. is gratefully acknowlegded for the financial support of the research. During the past five years, I've been supported by many of my colleagues, friends and family. Here, I would like express my gratitude to some of them in particular. First of all, I wish to thank my supervisor professor Philip de Goey. His unflagging enthusiasm, the numerous and challenging discussions, and his faith were a great support. Secondly, professor Anton van Steenhoven, who was closely involved with the project from the beginning. Furthermore, professor Dirk Roekaerts and professor Henk Nijmeijer for carefully reading a draft version of this thesis and suggesting a number of useful improvements.

I thank Ruud Eggels and Jeroen van Oijen, who were also largely contributed to the progress of the project. Firstly, Ruud Eggels and his family are gratefully acknowledged for hosting and guiding me during several traineeships at Rolls-Royce in the United Kingdom and Germany. Secondly, I am gratefully indebted to Jeroen van Oijen for the many fruitful discussions we've had over the years.

Of course, my colleagues of the Combustion Technology Group, who always managed to create a nice and pleasant working atmosphere. More specifically my current room mates, Vincent and Alexey and especially my former room mate Gemmeke, with whom I shared the office during the largest part of the PhD. study.

Dealing with a renal disease has put quite a demand on the improvisation skills of many. Herewith, I want to thank everyone who was willing to be considerate in some way, so I was able to participate in all kinds of social events inside and outside the university, varying from practicing sports, making music, going out, making trips, etc. In particular, my former fellow students of Mechanical Engineering, the members of XQSME, which truly is the hottest party band around, the members of the Pencak Silat association PAMUR Kombinasi, especially my teacher Guru Besar Ph.J.C. Tönjes, who taught to me stay optimistic and to persevere. And of course, I thank all my close friends, my brother Yuri, and my parents for their support, love and friendship.

Curriculum Vitae

May 29th, 1976	:	Born in Assen, the Netherlands.
Aug. 1988 - June 1994	:	Secondary education (V.W.O.), De Groene Driehoek, Hoogeveen.
Sept. 1994 - June 2000	:	Mechanical Engineering, Eindhoven University of Technology, M.Sc. degree.
Aug. 2000 - June 2005	:	Ph.D. student, Combustion Technology Group, Faculty of Mechanical Engineering, Eindhoven University of Technology.
July 2005 - present	:	Post-doctoral researcher, Combustion Technology Group, Faculty of Mechanical Engineering, Eindhoven University of Technology.